2022

Optical Imaging Of Tissue Physiology With Exogenous Contrast Agents

Sang Hoon Chong
University of Pennsylvania

Optical Imaging Of Tissue Physiology With Exogenous Contrast Agents

Abstract

This thesis describes experiments and analyses which push the frontier per what one can learn from optically emitting exogenous contrast agents in living tissue. The first set of experiments concurrently measured cerebral blood flow and bothintravascular- and extravascular-tissue oxygen concentration in a rat brain during functional activation; the new instrumentation needed to collect this information used contrast agent phosphorescence lifetime to determine oxygen concentration and speckle contrast imaging to probe blood flow. The concurrent measurement of multiple physiological parameters with high temporal resolution (~7 Hz) provided a unique opportunity to observe the interconnected dynamics of oxygen exchange, blood flow, and cerebral oxygen metabolism. The experiments showed that initial metabolic changes trigger a blood flow response; comprehensive theoretical modeling of the data exposed potential weaknesses of the well-known and often-used two-compartment oxygen diffusion model, and the experiments as a whole introduced a new tool for characterization of oxygen metabolism and neurovascular coupling in the brain.

The second set of experiments developed instrumentation and a simple theoretical methodology for imaging fluorescent targets in turbid media such as tissue. This approach used the ideas of spatial frequency domain fluorescence diffuse optical tomography (SFD-FDOT). The new reconstruction algorithm modified the more complex SFD-FDOT reconstruction method to rapidly acquire the depth of fluorescent target(s) and then estimate the transverse margins of the fluorescent target(s). Tissue phantom experiments demonstrated the instrumentation and algorithm, and assessed limitations. The new methodology could be useful for image guidance during tumor resection surgery, and could also provide rapid and useful constraining information for more comprehensive fluorescent tomography.

Degree Type

Dissertation

Degree Name

Doctor of Philosophy (PhD)

Graduate Group

Physics & Astronomy

First Advisor

Arjun G. Yodh

Keywords

Cerebral Metabolic Rate of Oxygen, Diffuse Optical Tomography, Fluorescence Image-Guided Surgery, Laser Speckle Contrast Imaging, Phosphorescence Lifetime Oximetry, Structured Illumination

Subject Categories

Biomedical | Biophysics

OPTICAL IMAGING OF TISSUE PHYSIOLOGY WITH EXOGENOUS CONTRAST AGENTS

Sang Hoon Chong

A DISSERTATION

in

Physics and Astronomy

Presented to the Faculties of the University of Pennsylvania

in

Partial Fulfillment of the Requirements for the

Degree of Doctor of Philosophy

2022

Supervisor of Dissertation

Arjun G. Yodh, James M. Skinner Professor of Science

Graduate Group Chairperson

Ravi K. Sheth, Professor of Physics and Astronomy

Dissertation Committee

Ravi K. Sheth, Professor of Physics and Astronomy
Joel H. Greenberg, Professor of Neurology
Eleni Katifori, Associate Professor of Physics and Astronomy
Wesley B. Baker, Assistant Professor of Neurology

OPTICAL IMAGING OF TISSUE PHYSIOLOGY WITH EXOGENOUS CONTRAST AGENTS

Dedicated to my wife, Su Kyung,

and my beloved kids, Ayn and Arjun.

ACKNOWLEDGMENT

My life has been a stream of unpredictable journeys driven by my reckless dreams. It also produced many difficult challenges. The last one, a degree of Ph.D., is finally conquered and turned out to be the most demanding goal so far. It might have not come to a good end without continuous support and encouragement from many people to whom I am so grateful.

My supervisor, Prof. Arjun Yodh, has guided me since my second year. He has been so patient and supportive throughout the whole longevity of my research training with him. He understood my weakness and gave me lots of critical and constructive advice and comments through which I have been trained to form better habits for experimental research. This process was not easy for both of us especially after my second kid was born and my practical studying hours started shrinking significantly. Owing to his continuous support, I was able to get through this difficult process while I could still take care of my two kids, for which I am indefinitely thankful. Thank you very much, Arjun! It is a great honor to be one of your students, and I hope I can repay the debt by growing as a better researcher.

I cannot express my gratitude enough to my research advisers. Prof. Sergei Vinogradov showed me the true meaning of being an expert on something. His work and thoughts on neural biology and chemistry were impeccable and kept our work in line with fundamental biochemistry. Besides, his lab crews, Mirna El Khatib and Srinivasa Allu, were always helpful and it was so pleasant to work with them. Prof. Vadim Markel is an incredibly smart mathematician and physicist. I learned a ton of practical mathematics related to imaging from him. Without his input and directions, it would have been onerous to bear fruit from one of my major projects. Prof. Joel Greenberg has mentored me since I started animal studies. I owe him a great debt

of knowledge in surgical preparation and neurological background. He also provided me with guidance on research often. I wish I could become such a kind research advisor someday. In terms of such guidance, I cannot be forgetful about Ashwin Parthasarathy and Wesley Baker. Ashwin advised and trained me with numerous optical setups and experimental skills that have proven useful in many other following experiments. Wesley has been an extremely reliable lifesaver at all times for any kinds of questions that I have. He always spared his time to give me better ideas in theory and experiments that helped me move forward. Han Ban and David Busch were great mentors in my early stage in the lab.

My friends and colleagues in the lab have encouraged and advised me with their own expertise and friendship. Most importantly, I am so honored to have shared their fellowships in this long tunnel that could have been too lonely without accompanying them. Lin and Yi Hong, I remember our uncountable conversations in the office and lab. The "Stupid Club" was the best private group of encouragement and fun that I have ever had at Penn. Ken's companionship and expertise in a variety of mechanics and instrumentation have been one of the most precious resources keeping the momentum of my research. Emilie Benson, Jeff Cochran, Rodrigo Forti, Tiffany Ko, Alistair Lewis, and Brian White, all of you were my role models. I wish I could have spent more time with you all in the lab, but I still perhaps have a chance to do so with some of you. Lastly, Wei-Shao Wei started the journey in the physics department at the same time. His unshakable passion for experimental physics and warm-hearted mind humbled and encouraged me so much. I will never forget the friendship with him and his wife, Yi-Yun Ho.

There are unsung heroes in all this. My family formed a strong backbone for the entire duration of the Ph.D. program. My wife, Su Kyung Kim, and our two kids, Ayn and Arjun (Yes, I named my boy after my supervisor!), have given me so much

love and patience. My sister, Woo Jung Chong, has taken care of my parents for a long time relieving some burden off my chest. My parents, Chae-Poong Chong and Sun Ouk Song, have supported their slowly maturing prodigal son for their entire life. I can only imagine how laborious and sometimes painful it could have been! My parents-in-law, Kwang-Up So and Se Eun Kim, never stopped encouraging and supporting my family even if they are far away from us.

Thank you all for granting me this incredible memory and achievement!

ABSTRACT

OPTICAL IMAGING OF TISSUE PHYSIOLOGY WITH
EXOGENOUS CONTRAST AGENTS

Sang Hoon Chong

Arjun G. Yodh

This thesis describes experiments and analyses which push the frontier per what one can learn from optically emitting exogenous contrast agents in living tissue. The first set of experiments concurrently measured cerebral blood flow and both intravascular- and extravascular-tissue oxygen concentration in a rat brain during functional activation; the new instrumentation needed to collect this information used contrast agent phosphorescence lifetime to determine oxygen concentration and speckle contrast imaging to probe blood flow. The concurrent measurement of multiple physiological parameters with high temporal resolution ($\sim$7 Hz) provided a unique opportunity to observe the interconnected dynamics of oxygen exchange, blood flow, and cerebral oxygen metabolism. The experiments showed that initial metabolic changes trigger a blood flow response; comprehensive theoretical modeling of the data exposed potential weaknesses of the well-known and often-used two-compartment oxygen diffusion model, and the experiments as a whole introduced a new tool for characterization of oxygen metabolism and neurovascular coupling in the brain.

The second set of experiments developed instrumentation and a simple theoretical methodology for imaging fluorescent targets in turbid media such as tissue. This approach used the ideas of spatial frequency domain fluorescence diffuse optical tomography (SFD-FDOT). The new reconstruction algorithm modified the more complex SFD-FDOT reconstruction method to rapidly acquire the depth of fluorescent target(s) and then estimate the transverse margins of the fluorescent target(s). Tissue

phantom experiments demonstrated the instrumentation and algorithm, and assessed limitations. The new methodology could be useful for image guidance during tumor resection surgery, and could also provide rapid and useful constraining information for more comprehensive fluorescent tomography.

TABLE OF CONTENTS

Acknowledgment iv

Abstract vii

List of Illustrations xii

Chapter 1 : Introduction 1

1.1 Probing Biological Tissue with Optics 1

1.2 Optical Contrast in Tissue 2

1.2.1 Endogenous chromophores 2

1.2.2 Exogenous contrast agents 4

1.3 Central Topics of this Thesis 7

1.4 Thesis Organization 8

Chapter 2 : Hemodynamics and Oxygen Metabolism in Rat Brain 10

2.1 Neurovascular Coupling and Its Significance 10

2.2 Prior Measurements Sensitive to Oxidative Metabolism in Brain . . . 12

2.3 Our Approach 14

2.4 Oxygen Dynamics and $CMRO_2$ 15

2.4.1 Intravascular-extravascular two-compartment oxygen transport model 16

2.4.2 Theoretical modeling of PS_c 18

2.4.3 Limitations of the Model 24

Chapter 3 : Optical and Surgical Methods for Probing Rat Brain Hemodynamics and Oxygen Metabolism 25
3.1 Optical Probing Techniques 25
3.1.1 Two-color phosphorescence lifetime oximetry 25
3.1.2 Laser speckle contrast imaging 30
3.2 Surgical Preparation 38
3.3 Experimental Sequence 39

Chapter 4 : Dynamics of Oxygen Metabolism and Blood Flow in Rat Brain 41
4.1 Two-color, Two-Oxyphor Measurement Method 41
4.2 Longitudinal Measurement Results 43
4.3 Selection of PS_c and Computation of Dynamic $CMRO_2$ 46
4.3.1 Data-constrained selection of PS_c 46
4.3.2 Computation of $CMRO_2$ 49
4.4 Limitations 58
4.4.1 Light penetration 58
4.4.2 Temperature dependence of Oxyphor 59
4.4.3 Invasive injection of Oxyphor 60

Chapter 5 : Spatial Frequency Domain Fluorescence Diffuse Optical Tomography for Image-guided Tumor Resection Surgery (Background and Theory) 61
5.1 Introduction 61
5.2 Theory of Spatial Frequency Domain Diffuse Optical Tomography . . 64
5.2.1 Light diffusion equation in turbid media 64
5.2.2 Source types 66
5.2.3 Green's function solutions in 2D Fourier space 68

5.2.4 Fast analytic inversion algorithms for spatial frequency domain light source . . . 71
5.2.5 Data acquisition and analysis . . . 72
5.2.6 Nonlinear fitting . . . 76

Chapter 6 : Spatial Frequency Domain Fluorescence Diffuse Optical Tomography for Image-guided Tumor Resection Surgery (Experiment, Results and Discussion) . . . 77
6.1 Experimental Results . . . 77
6.1.1 Imaging instrumentation . . . 77
6.1.2 Experimental procedure . . . 79
6.1.3 Single-target experimental results . . . 81
6.1.4 Two-target experimental results . . . 85
6.2 Discussion . . . 89
6.2.1 Depth sensitivity . . . 90
6.2.2 Transverse margins . . . 91
6.2.3 The spatial smoothing (regularization) parameter . . . 92
6.2.4 Stability of the estimates . . . 93
6.2.5 Data acquisition and reconstruction times . . . 94
6.2.6 Limitations . . . 94
6.3 Summary and Outlook . . . 96

Chapter 7 : Summary . . . 97

Appendix . . . 100

LIST OF ILLUSTRATIONS

Figure 1 : Absorption coefficient spectra of the major endogenous chromophores in tissue. Reprinted from Fig. 1 of Ref. 36. 3
Figure 2 : Example spectra of Oxyphor R4 (red) and G4 (green). (a) Absorption spectra. (b) Relative emission spectra. Reprinted from Fig. 2 of Ref. 44. 5
Figure 3 : ICG absorption and emission spectra of 6.5μM in the blood plasma. Reprinted from the package insert of ICG [3]. 6

Figure 4 : Schematic of oxygen delivery from vasculature to tissue. . . . 11
Figure 5 : (a) Schematic of Krogh-Erlang cylinder model. (b) Cross-section view of a single capillary and the surrounding extravascular tissue cylindrical shell corresponding to one of the coaxial cylinders in (a). 18
Figure 6 : Oxygen concentration profile along the radial distance from the wall ($\rho_1 = 3$ μm) to the outer surface of the tissue cylinder ($\rho_2 = 30$ μm) in Krogh cylinder model. 21
Figure 7 : $G(\rho_2/\rho_1)$ as a function of ρ_2/ρ_1. 23

Figure 8 : Simplified Jablonski Diagram. S_o: Ground State, S_1: Singlet State, T_1: Triplet State. 26
Figure 9 : Stern-Volmer Relations. (a) Oxyphor R4. (b) Oxyphor G4. . 27
Figure 10 : (a) Scheme of the experimental setup. (b) Wide-field image of the craniotomy window over the somatosensory area. Scale bar: 1 mm. 28
Figure 11 : Example phosphorescence emission single decay curves for (a) PtR4 and (b) PtG4. 30
Figure 12 : Examples of (a) a raw speckle image, and (b) speckle contrast processed image. Scale bar indicates 1 mm. 37
Figure 13 : Protocol of the surgical procedure and measurement. 39
Figure 14 : Scheme of the experiment protocol 40

Figure 15 : Optical absorption and phosphorescence spectra of Oxyphors PtG4 (Channel 1) and PtR4 (Channel 2). 42
Figure 16 : Raw unprocessed data obtained in an experiment consisting of 13 consecutive forepaw stimulations, accompanied by (a) CBF, (b) p_iO_2, and p_eO_2 measurements in the somatosensory area of the rat brain. 44
Figure 17 : Overlapping traces of p_eO_2. 45

Figure 18 : An example of $CMRO_2$, pO_2 and CBF response to a single functional stimulus. (a) $CMRO_2$ was computed from pO_2 data (b). (b) and (c) are single-shots of pO_2 and CBF responses respectively. 51
Figure 19 : (a) Computed traces of full-dynamic and truncated-dynamic $CMRO_2$ (see the text for definitions) for three different values of parameter PS_c. (b) Normalized traces of CBF, p_eO_2, p_iO_2 and full-dynamic $CMRO_2$ 52
Figure 20 : Normalized traces of $CMRO_2$, p_iO_2, p_eO_2 and CBF. (a,b) compares dynamic $CMRO_2$ with p_iO_2, p_eO_2 and CBF, and (c,d) compares steady-state $CMRO_2$ with p_iO_2, p_eO_2 and CBF. . . 54
Figure 21 : Temperature-dependent PtG4 calibration curve. At a given phosphorescence decay time, τ, a different pO_2 value is assigned according to the temperature. 60

Figure 22 : Schemes of light sources. (a) CW, (b) FD, and (c) TR light source. The figure is reprinted from Ref. 36 67
Figure 23 : Two examples of spatially modulated light patterns. (left) An example of lower spatial frequency ($f = 0.02$ mm^{-1}) light pattern. (right) An example of higher spatial frequency ($f = 0.07$ mm^{-1}) light pattern. 67

Figure 24 : Schematics of the dual-camera imaging system. **SM**: Spatial modulator of the excitation light, **CL**: Collection lens, **RL**: Relay lens, **BS**: 10:90 Beam-splitter, **BF**: Bright-field camera, **EM**: Emission filter, **FL**: Fluorescence camera. 78
Figure 25 : Schemes employed for tissue phantom experiments. (a) The single-target experiments. (b) The two-target (on the same depth) experiment. (c) The two-target (on different depths) experiment. 80
Figure 26 : Example of the measurements in case of single target located at the depth of 2 mm ($f = 0.04$ mm^{-1}). Scale bar indicates 10 mm. 80
Figure 27 : Single target experiment depth estimaion results . The target depth is 2 mm (a), 4 mm (b), 6 mm (c), 8 mm (d), and 10 mm (e). 82
Figure 28 : Single target experiment transverse margin estimaion results . The target depth is 2 mm (a), 4 mm (b), 6 mm (c), 8 mm (d), and 10 mm (e). Yellow scale bar indicates 10 mm. 83

Figure 29 : Transverse image of the fluorescent inclusion at 4mm depth with different values of σ. (a) A weak regularization ($\sigma = 3.77$ mm^{-1}). (b) The optimal regularization ($\sigma = 0.46$ mm^{-1}). (c) A strong regularization ($\sigma = 0.11$ mm^{-1}). 84
Figure 30 : Reconstruction results of single-target experiments. (a) Depth-estimation results. The black dotted line has a unity slope. (b) The ratio between reconstructed image width and the true target width as a function of depth. 85
Figure 31 : Reconstructed transverse margin of two-target experiment. Two targets were placed on the same depth, and it varied as well as transverse separation. 86
Figure 32 : Reconstruction results of two targets in the same vertical plane. (a) Depth-estimation results. (b) Relative width estimation results. 86
Figure 33 : Raw data showing substantially different emission signals from Targets 1 (deep target) and 2 (superficial target). Scale bar corresponds to 10 mm. 87
Figure 34 : 3D rendering of the two-target vertical separation results. . . 88
Figure 35 : Results of the two-target experiments with vertical separations. (a) Results for the reconstructed depth of Targets 1 and 2. The dashed line has the unity slope. (b) Results of the relative width of Targets 1 and 2. 89
Figure 36 : Mean absolute errors for all depth estimation results. 92
Figure 37 : Optimized regularization parameter σ for single-depth reconstruction as a function of the target depth. 93

Figure 38 : Absorption (a) and phosphorescence (b) spectra of Oxyphor PtR4 in 50 mM phosphate buffer solution (pH 7.1, $\lambda_{ex} = 512$ nm). 105
Figure 39 : Phosphorescence quenching plot of Oxyphor PtR4. 107
Figure 40 : Optical absorption and emission spectra of the probes and associated laser lines and optical filters in Channels 1 and 2 of the phosphorometer. The spectral ranges seen by the detectors (APDs) are shown by shaded areas. **lp** is the abbreviation for *long-pass filter*, and **sp** is for *short-pass filter*. 108

Chapter 1

Introduction

1.1 Probing Biological Tissue with Optics

Broadly, optical techniques of many kinds have been successfully employed to investigate normal and abnormal tissues [93]. Depending on desired biological goals and interrogation length scales, experimenters will choose a wavelength range, a measurement geometry (*e.g.*, reflection/transmission, microscopic/macroscopic, etc.), and a suitable technology (*e.g.*, absorption/fluorescence frequency-domain or time-domain spectroscopy, fluorescence/phosphorescence lifetime measurement, correlation spectroscopy, *etc.*).

In this thesis, all of our experiments aim to probe "near-surface" tissues in the reflection geometry. Thus, the light sources and detectors reside on the same (observing) side of the tissue sample. For this work, we predominantly (but not exclusively) employ near-infrared (NIR) light. Roughly speaking, NIR light ranges from 600 nm to 1000 nm. Compared to visible light, photons in NIR have excellent penetration depth in tissue, ranging from millimeter to centimeter scales [36]. Thus, its use enables non-invasive and minimally invasive studies of relatively deep tissues that are typically inaccessible to traditional optical microscopies [31] and methods that rely on single scattering (or no scattering). NIR spectroscopy (NIRS) provides access to the absorption of major endogenous tissue chromophores (*e.g.*, oxy- and deoxy-hemoglobin) [111]; NIR light (pulsed or CW) can be employed to excite exogenous

contrast agents in tissue, which in turn can provide information about tissue oxygen (*via* fluorescence lifetime measurements) [89] or information about tumor margins (*via* fluorophore concentration) [144]; narrowband NIR light sources enable accurate measurements of the speckle fluctuations of reflected light, which in turn provide information about blood flow [38].

In this thesis, I will discuss optical instrumentation, algorithms, and experimental schemes we have developed to probe fluorescent/phosphorescent exogenous contrast agents in two contexts. In one study, we measure agent phosphorescence lifetime to characterize tissue oxygen gradients in the vasculature of rat-brain cortex during resting-state and functional activation. These experiments push the frontier of what is known about neurovascular coupling and oxygen metabolism. In the second, qualitatively different study, we develop fluorescence-imaging instrumentation and algorithms to locate fluorescent targets in situations relevant for image-guided tumor resection surgery. Note, while the central focus of both studies is on exogenous contrast agents, both studies also require measurement/knowledge of endogenous tissue properties.

1.2 Optical Contrast in Tissue

1.2.1 Endogenous chromophores

The tissue contains many molecules, but only a few of these chromophores absorb substantial amounts of light (chromophores) in the range of UV, VIS, and NIR parts of the optical spectrum. This large absorption is a consequence of their comparatively large concentration and oscillator strength. These chromophores are oxy- and deoxy-hemoglobin (HbO_2 and HbR respectively), water, and lipid. Importantly, as noted

above, these chromophores collectively absorb the least amount of light in the NIR part of the optical spectrum, and therefore this regime of minimum absorption is traditionally referred to as the physiological window (Fig.1)). In this window, light penetration depth in most tissues ranges from millimeters to centimeters, depending on blood concentration.

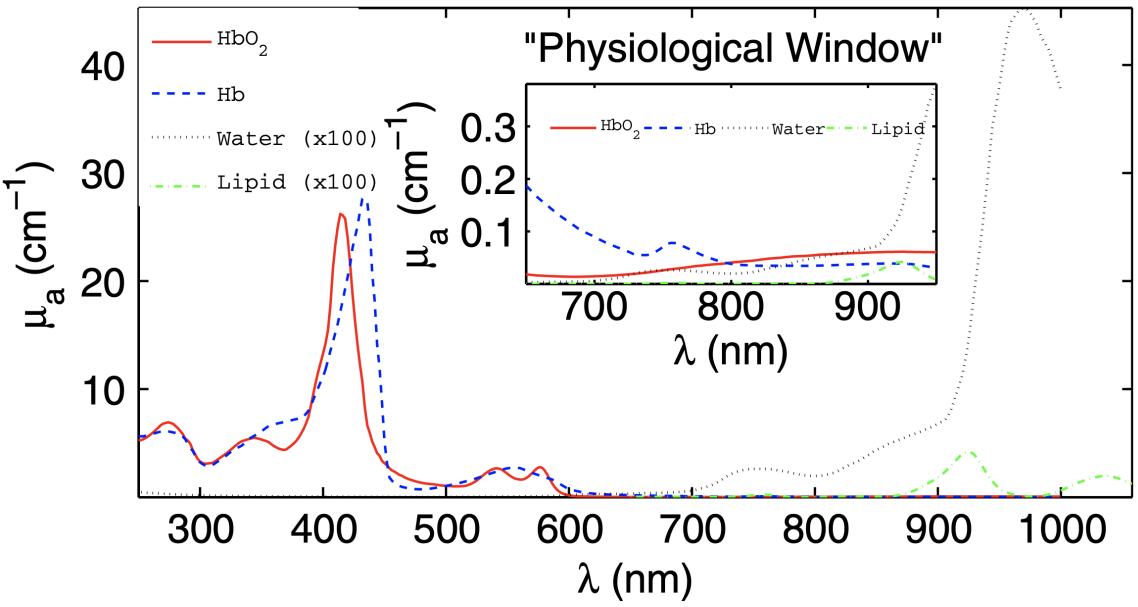

Figure 1: Absorption coefficient spectra of the major endogenous chromophores in tissue. Reprinted from Fig. 1 of Ref. 36.

When NIR light propagates in tissue, it interacts with these chromophores, and it also interacts with organelles, nuclei, cells, and their associated membranes/interfaces. Photons are lost *via* chromophore absorption, and photons are scattered by the organelles, *etc.* In most tissues, the absorption mean free path (*i.e.*, the reciprocal of the absorption coefficient μ_a) is long compared to the so-called reduced scattering mean free path (*i.e.*, the reciprocal of the reduced scattering coefficient μ_s'), In this regime, the diffusion equation (with loss) is a very good approximation for photon transport.

Diffuse optics refers broadly to techniques that utilize the diffusion equation as an underlying mathematical framework to analyze the propagation of light in turbid media, *e.g.*, NIR light in most tissues. Our experiments in the reflection geometry, for example, utilize models based on the diffusion equation to predict the propagation of NIR light into and out of tissue. The model permits the determination of the medium's absorption (μ_a) and reduced scattering coefficient (μ_s') [36], and the wavelength dependence of these parameters (especially μ_a) enables experimenters to deduce the concentrations of the aforementioned endogenous chromophores [37].

The NIR absorption technique, *i.e.*, NIR spectroscopy (NIRS), enables many clinical and pre-clinical applications. For example, in breast cancer, tumor tissues exhibit optical properties that differ from those of normal surrounding tissues as a result of their microvasculature and metabolism; typically, for example, tumors show higher concentrations of HbO_2 and HbR compared to normal tissue. These differences provide spectroscopic contrast which is useful for tomographic imaging of breast cancer and for monitoring the response of cancer to therapy [23, 139, 21, 20, 7, 49]. In a different vein, continuous measurement of HbO_2 and HbR can inform experimenters about the hemodynamics and oxygen dynamics in brain tissue [25]. Indeed, NIR spectroscopy and tomography of HbO_2 and HbR have been an important surrogate for direct molecular oxygenation measurements in tissue; moreover, if integrated with optical measurements of cerebral blood flow (CBF), it is possible to estimate cerebral oxygen consumption or the so-called cerebral metabolic rate of oxygen ($CMRO_2$).

1.2.2 Exogenous contrast agents

While endogenous contrast is useful and can be probed non-invasively, there have been significant advances in the field per development of exogenous contrast

agents. Exogenous contrast agents must be introduced into tissue and are thus invasive (potentially, minimally invasive). Their utility arises from their potential to teach us about other properties in tissue, properties that cannot be rigorously determined from endogenous contrast. For example, in our experiments on functional activation in brain, we utilize exogenous porphyrin-based phosphorescence agents (Oxyphors); the lifetime of their photoluminescence is sensitive to the oxygen concentration in tissue. Oxyphors have been applied in a variety of contexts because their sensitivity to molecular oxygen concentration is relevant to many important metabolic questions. Some optical technologies used thus far with Oxyphors are two-photon microscopy [43, 51, 2, 124], fiber-based imaging [101], and camera-based imaging [44, 120]. Deployment of the phosphorescent agent in tissue enables direct spatiotemporal measurement of oxygen concentration, which is more direct than more common analyses of tissue blood oxygen dynamics based on HbO_2 and HbR. Typically, these exogenous contrast agents are designed to be excited by visible (green and red) light, and they emit phosphorescence light in the NIR.

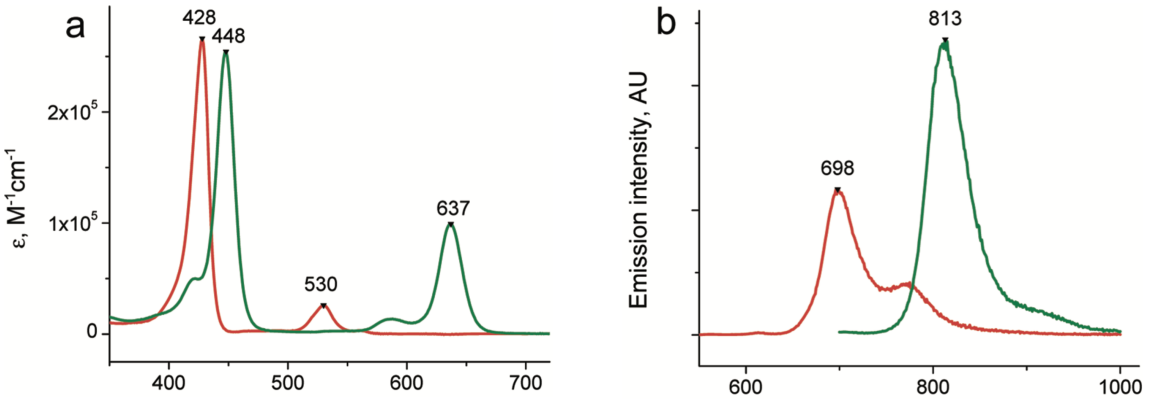

Figure 2: Example spectra of Oxyphor R4 (red) and G4 (green). (a) Absorption spectra. (b) Relative emission spectra. Reprinted from Fig. 2 of Ref. 44.

Another useful exogenous contrast phenomenon is based on fluorescence for tumor detection and characterization. This general problem is a part of the motivation

for our diffuse optical imaging experiments. Specifically, an exogenous contrast agent called indocyanine-green (ICG) has been FDA-approved for clinical use. Among other things, it is the major contrast agent used for clinical angiography [126, 40]. Due to its good fluorescent efficiency and safety, it has also been increasingly deployed as a fluorescent contrast agent for image-guided surgery for tumor resection [113, 6]. In this case, the surgeon injects ICG to a patient 24 hours ahead of the tumor resection surgery; due to various factors, the ICG molecules will preferentially accumulate in and around tumor tissue *via*its leaky vasculature. Using this so-called ICG retention effect [108], the absorption and emission of ICG (and variants) in this context have permitted tumor detection (Fig. 3). In this case, measurement of the enhanced concentration of the agent (in space and in time) permits tumor detection and characterization. Looking forward, all-out efforts to develop cell-specific fluorescent dyes for better contrast are ongoing [72, 29]. Parallel efforts (such as ours) that aim to improve the fidelity of fluorescent contrast imaging are vital too.

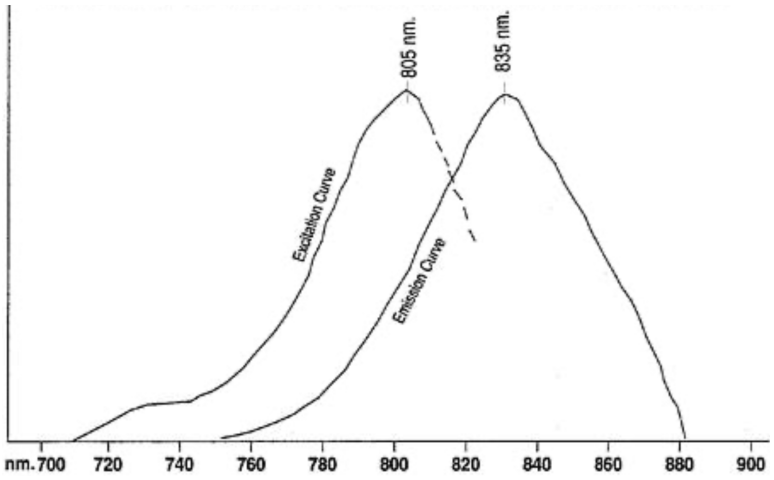

Figure 3: ICG absorption and emission spectra of 6.5μM in the blood plasma. Reprinted from the package insert of ICG [3].

1.3 Central Topics of this Thesis

In the remaining chapters of this thesis, two important applications of exogenous contrast agents are utilized to probe issues at the Biophotonics frontier. Both works enable the acquisition of important information about biological tissue. In the first set of experiments, two phosphorescent contrast agents (Oxyphors) are deployed to interrogate oxygen metabolism in rat brain before, during, and after functional activation. $CMRO_2$ is an important biomarker that we gain access to as a result. In principle, information about $CMRO_2$ can teach us how to assess normal and diseased brain function [54, 129, 130]; furthermore, better information about $CMRO_2$ can help us to answer fundamental questions associated with oxygen dynamics, neurovascular coupling, and metabolic mechanisms in brain. Traditional measurement paradigms for the study of $CMRO_2$ lack the temporal, spatial, and biochemical resolution to fully elucidate dynamic neurological events, *e.g.*, neurovascular coupling. In our investigation, we introduce a new experimental platform to estimate $CMRO_2$ with high temporal and spatial resolutions by simultaneously monitoring intra- and extra-vascular oxygen concentration before, during, and after functional activation. Additionally, we acquired images of cerebral blood flow (CBF) concurrently. Thus, assessment of $CMRO_2$ directly from Oxyphor oxygen measurements provides a novel opportunity to compare the detailed dynamics of oxygen consumption and blood flow with high temporal resolution.

The second set of experiments aims to estimate the depth and transverse margins of fluorescent targets in turbid media. This is an important task that, if carried out rapidly enough, could be utilized by a surgeon for surgical decision-making. Currently, image-guided tumor resection surgery has been increasingly popular due to real-time two-dimensional image-projection guidance, *i.e.*, a surgeon can coarsely

distinguish near-surface tumors from normal tissue by taking two-dimensional images of tissue fluorescence. However, this technique lacks depth information which can be critical for surgeries wherein preserving healthy normal tissue is important. Our work builds on current Spatial Frequency Domain Fluorescence Diffuse Optical Tomography (SFD-FDOT) research. We developed an SFD-based algorithm and instrumentation to assess the depth and transverse margins of fluorescent targets quickly. The instrumentation and algorithm were evaluated experimentally in order to take the first step toward translation to the operating room. The work can also be useful as complimentary priori information in more comprehensive FDOT too.

1.4 Thesis Organization

In the remainder of this thesis, Chapters 2 - 4 are devoted to the first set of experiments that seek to probe $CMRO_2$ in rat brain by direct measurement of oxygen concentration. Chapters 5 & 6 report the algorithm and instrumentation and testing for a new SFD-FDOT technique for fast acquisition of depth/margin.

More specifically, Chapter 2 introduces neurovascular coupling and $CMRO_2$. Further, it explains why the platform we develop could be valuable for future studies of $CMRO_2$ (especially in comparison to existing technology). Lastly, it introduces the theoretical framework we employ to estimate $CMRO_2$ from our measurements. In Chapter 3, the primary measurement techniques are introduced along with information about detailed surgical preparation for the experiment. Chapter 4 demonstrates the full approach, reports important results from the measurements, and discusses its impact on the interpretation of neurovascular coupling and other biological phenomena in the brain.

In Chapter 5, a brief background of the general problem is given, and the theory of diffuse optics and then SFD-FDOT is introduced in detail. The aspects of the

theory of SFD-FDOT needed for our experiments with fluorescent targets is then further developed and explained. Chapter 6 reports the experimental results and system performance through a series of phantom experiments.

Lastly, Chapter 7 summarizes the results and discussion from both experiments, and provides brief suggestions for future work.

Chapter 2

Hemodynamics and Oxygen Metabolism in Rat Brain

This Chapter has been largely adapted from a pending publication: Chong, S. H., Ong, Y. H., El Khatib, M., Allu, S. R., Parthasarathy, A. B., Greenberg, J. H., Yodh, A. G., & Vinogradov, S. A. (2022). *Real-Time Tracking of Brain Oxygen Gradients and Blood Flow during Functional Activation* [Manuscript submitted for publication]. Department of Physics & Astronomy, University of Pennsylvania.

2.1 Neurovascular Coupling and Its Significance

A continuous oxygen supply is critical for maintaining activity in the brain [160, 17, 77]. Briefly, blood carries oxygen and distributes it into brain tissue (predominantly) *via* a network of capillary vessels as shown in Fig. 4 (Note, the image design in the figure is closely related to Fig. 2 of Ref. 70.). Oxygen molecules diffuse from the vessels into neighboring extravascular tissues down a concentration gradient [140] which depends on the rate of oxygen consumption; in the brain, this oxygen consumption rate is called the cerebral metabolic rate of oxygen ($CMRO_2$). The oxygen is metabolized by mitochondria to generate energy *via* its primary pathway, oxidative phosphorylation [17, 22].

Even in their resting state, brain cells are active [95]. Thus, they require a supply of oxygen at all times. However, during functional activation more oxygen is needed, and cerebral blood flow (CBF) must rapidly respond to these changes in neuronal

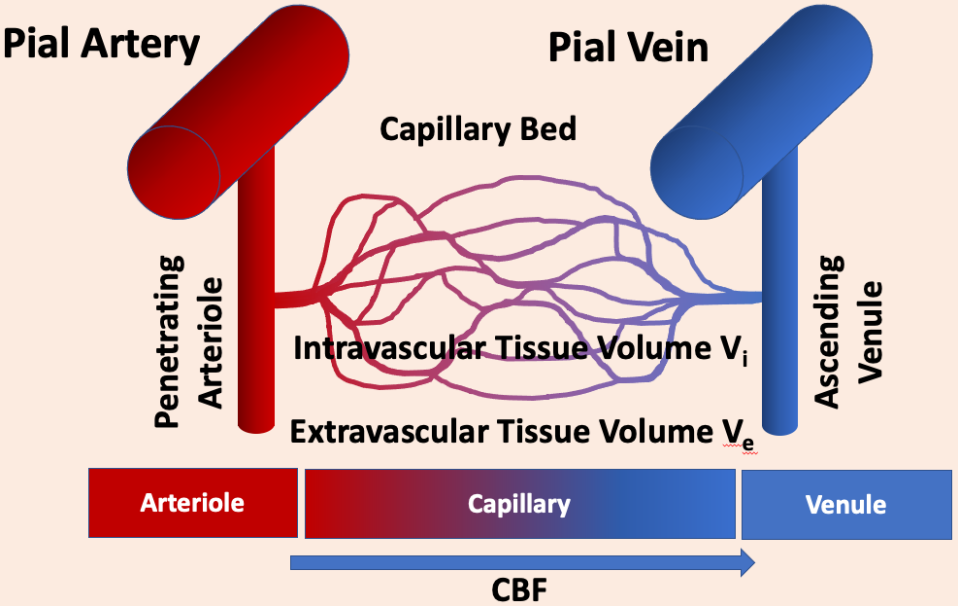

Figure 4: Schematic of oxygen delivery from vasculature to tissue.

activity. More oxygen must be supplied to regions where more activity occurs [71]. The cascade of events connecting variation of neuronal activity to CBF response is known as neurovascular coupling (NVC) [28]. If NVC is compromised, then the brain can suffer local deprivation of oxygen, which can lead to cell death, and potentially permanent neurological disorders [77]. Therefore, comprehensive knowledge about NVC is valuable for understanding the physiology of both healthy and abnormal brains. One way to learn about NVC is to observe and compare hemodynamics and oxygen dynamics in the brain during steady-state (resting-state) and during functional activation. Information about the sequence of events following functional activation, for example, is invaluable for ascertaining the causal connections between various vascular and extravascular physiological parameters [60].

The pure hemodynamic parameters of importance for us (in brain) include CBF, and the concentration of oxy- and deoxy-hemoglobin (HbO_2 and HbR), or, equivalently, the total hemoglobin concentration and blood oxygen saturation (THC and

SO_2). The molecular oxygen parameters of importance within the vascular system are the bound and unbound oxygen concentration in arteries, arterioles, capillaries, venules, and veins. For functional activation in brain, we are specifically interested in the total (bound and unbound) oxygen concentration in the arterioles, capillaries, and venules, which we denote C_a, C_c, and C_v, respectively. Additionally, we are interested in unbound molecular oxygen parameters both outside the vascular system (in extravascular tissue) and within the vascular system (*i.e.*, intravascular); here we denote unbound oxygen concentrations in the capillary intravascular space and in the extravascular space as C_i and C_e, respectively. In our experiments, we measure these latter unbound oxygen parameters, which in turn provide access to $CMRO_2$ as described quantitatively below. Additionally, in our experiments, we measure CBF. The concurrent acquisition of CBF and $CMRO_2$ enables us to systemically compare hemodynamic and oxygen consumption responses.

2.2 Prior Measurements Sensitive to Oxidative Metabolism in Brain

Quantitative assessment of $CMRO_2$ has been of interest to the neuroscience community for many years. $CMRO_2$ can be a useful marker for early detection of tissue pathology such as in stroke [54], traumatic brain injury [129], and glioma [130]. Moreover, dynamic measurements of $CMRO_2$ during neuronal activation provide information about the brain metabolic events that underpin functional responses [13]. Positron Emission Tomography (PET) with ^{15}O-labeled compounds (O_2, H_2O, CO) is arguably the most established method for absolute $CMRO_2$ quantification in steady-state [103, 66]. PET is compatible with human studies, but quantitative measurement of $CMRO_2$ with PET requires independent measurements of CBF and total cerebral

blood volume (CBV), and it relies on multi-parametric models for the calculation of $CMRO_2$ [102, 76]. Furthermore, PET has a low temporal resolution on the order of 2-7 minutes [45] and is, therefore, unable to reveal rapid metabolic dynamics of cerebral tissues during neuronal activation.

For dynamic tracking of brain responses, the most widely used methods are Blood-Oxygen-Level-Dependent functional Magnetic Resonance Imaging (BOLD fMRI) [117, 164] and functional Near-Infrared Spectroscopy (fNIRS) [47, 163, 115]. The central parameter in both techniques is hemoglobin oxygen saturation (S_tO_2), and, like PET, absolute quantification of $CMRO_2$ requires independent measurements of oxygen extraction fraction (OEF), CBF, and CBV, and relies on multi-parametric models [14, 64, 164, 61, 35, 39, 25].

As a result, BOLD fMRI and fNIRS are best suited to probe relative changes in $CMRO_2$, albeit with resultant computed $CMRO_2$ dynamics inherently coupled to the dynamics of CBF. However, since $CMRO_2$ and CBF need not change in the same way when responding to activation, their relative timing carries valuable information about the dynamics of NVC [65, 147], and this relative timing is inaccessible to PET, BOLD fMRI, and fNIRS which rely on CBF for calculation of $CMRO_2$.

Apart from techniques that evaluate cerebral hemodynamics, local $CMRO_2$ can also be inferred from measurements of molecular oxygen gradients around individual vessels, for example by using diffusion-based models such as the two-compartment model suggested by Krogh [75]. The partial pressure of oxygen (pO_2), and pO_2 gradients around vessels were originally measured with oxygen microelectrodes [148]. More recently, two-photon phosphorescence lifetime microscopy (2PLM) has proved useful for spatially-resolved microscopic pO_2 measurements [48]. 2PLM is minimally invasive and is capable of probing pO_2 at multiple locations near vessels in the brain [118, 82]. However, mapping oxygen by 2PLM requires long observation

times, and therefore the technique is best suited for measurements of steady-state gradients [30, 119]. On the other hand, phosphorescence lifetime oximetry has been used to observe stimulus-induced changes of brain pO_2 [4], demonstrating capability for measurements at speeds comparable with transients of neuronal activity. Lastly, microelectrodes and laser Doppler have been used concurrently to track intravascular and extravascular pO_2 in two selected locations, along with local CBF during functional stimulation; together the three signals provided information sensitive to changes in oxygen metabolism, but $CMRO_2$ was not computed [146].

2.3 Our Approach

Here we introduce and demonstrate an all-optical imaging approach for dynamic measurement of $CMRO_2$. The new methodology is based on the quantification of oxygen concentration gradients in the brain using two macromolecular phosphorescent probes, Oxyphors [92, 44], placed separately in the intravascular and extravascular compartments. These probes are carefully designed such that they do not diffuse across the blood-brain barrier, and the chromophores in the probes have distinguishable optical spectra. Thus, the Oxyphors can be interrogated independently and concurrently for direct measurement of oxygen gradients in both compartments. In our work, we sampled oxygen gradients in rat brain cortex at a rate of ~ 7 Hz, but this sampling frequency can potentially be increased > 10-fold. In parallel, we measured the local CBF by laser speckle contrast imaging (LSCI). This combination enabled us to correlate measured changes in $CMRO_2$ with measured changes in CBF and thus ascertain the timing of the physiological events that accompany neuronal activation.

The new approach is minimally invasive, offers superior time-resolution (potentially approaching milliseconds), and creates novel opportunities for dynamic tracking and quantification of brain metabolism. Ultimately, with straightforward improve-

ments in technology, it should be possible to minimize systematic quantification errors associated with oxygen gradients, and thereby generate a robust method for *in vivo* dynamic quantification of absolute $CMRO_2$.

2.4 Oxygen Dynamics and $CMRO_2$

In our approach, $CMRO_2$ is estimated by direct measurement of oxygen concentrations in both intravascular and extravascular space. To understand how this works in practice, in this section, we present a comprehensive theoretical model.

We use the two-compartment theory [142] to model oxygen transport from the vasculature to the extravascular tissue; this theory enables us to estimate $CMRO_2$ in conjunction with the Krogh-Erlang cylinder model [75]. The variables and parameters we use are defined, along with their units, in Table 1.

Table 1: Descriptions of parameters and variables.

Symbol	Unit	Description
V_i	mL/100g Tissue	Capillary (intravascular) volume per unit mass of brain tissue.
V_e	mL/100g Tissue	Extravascular volume per unit mass of brain tissue.
V_t	mL/100g Tissue	Full tissue volume($V_i + V_e$) per unit mass of brain tissue.
CBF	mL/s/100g Tissue	Cerebral blood flow per unit mass of brain tissue.
C_a	mM	Arteriole O_2 concentration (includes both bound and unbound to Hb).
C_c	mM	Capillary O_2 concentration (includes both bound and unbound to Hb).
C_v	mM	Venule O_2 concentration (includes both bound and unbound to Hb).
C_i	μM	Capillary O_2 concentration (includes unbound O_2 only).
C_e	μM	O_2 concentration in the extravascular interstitial space of tissue.
P	cm/s	Permeability of O_2 molecule across capillary wall.
S_c	cm^2/100g Tissue	Surface area of capillary per unit mass of brain tissue.
$CMRO_2$	μmoles/s/100g Tissue	Cerebral metabolic rate of oxygen.

2.4.1 Intravascular-extravascular two-compartment oxygen transport model

The brain capillary network architecture is complex, and modeling capillary oxygen (O_2) dynamics is challenging. Therefore, we simplify the complex capillary structure to a simple cylindrical tube as has been done for many years (*e.g.*, the Krogh-Erlang Model). Our situation and model are schematically illustrated in Fig.4. In this model, O_2 is delivered by blood flowing through the penetrating arteriole, and from there it is distributed into the complex capillary network. The blood passing through the capillaries contains O_2 dissolved in the blood plasma; this dissolved O_2 is in equilibrium with O_2 bound to hemoglobin, which is described by the Hill equation [155]. Some of this O_2 diffuses into the extravascular tissue to support tissue metabolism. O_2 transport into and out of the capillary network is modeled by Eq. (2.1).

$$V_i \frac{\mathrm{d}C_c(t)}{\mathrm{d}t} = \mathrm{CBF}(t) \cdot [C_a(t) - C_v(t)] - \mathrm{PS}_c \cdot [C_i(t) - C_e(t)]. \tag{2.1}$$

The temporal rate-of-change of O_2 molecules, including both bound and unbound to hemoglobin, in the capillary compartment volume is shown on the left-hand side (LHS) of this equation; here C_c is the O_2 molecule concentration (bound and unbound). V_i represents the total capillary compartment volume, *i.e.*, the total intravascular volume. The temporal rate-of-change of total O_2 in the capillary volume depends on the factors on the right-hand side (RHS) of the equation above. The first term on the RHS of Eq. (2.1) defines the net-flow of O_2 molecules into the capillary compartment; here $\mathrm{CBF}(t)$ is the absolute blood flow at time t. C_a and C_v are arteriole and venule O_2 molecule concentrations, respectively. C_a and C_v include O_2 molecules bound to hemoglobin and O_2 molecules dissolved in the blood plasma; they

are in units of mM. The second term on the RHS represents the extraction rate of O_2 molecules from the capillary compartment into the extravascular tissue; here PS_c is a product of the O_2 permeability, P, and the capillary surface area, S_c. C_i and C_e represent the average O_2 molecule concentration in intravascular and extravascular tissue compartments, respectively; note, C_i and C_e depend only on dissolved O_2 molecules (*i.e.*, only on unbound O_2). Notice that this extraction rate of O_2 from the capillary is roughly proportional to the concentration gradient of average unbound O_2 concentration between the intravascular and extravascular compartments. The permeability contains the diffusion coefficient for O_2 and some effective lengths (slightly longer than the capillary radius. see Sec. 2.4.2).

A similar equation can be written for the extravascular unbound O_2 molecule concentration.

$$V_e \frac{\mathrm{d}C_e(t)}{\mathrm{d}t} = PS_c \cdot [C_i(t) - C_e(t)] - CMRO_2(t). \tag{2.2}$$

The LHS term is the time rate of change of O_2 molecules in the extravascular compartment. It depends on the derivative of C_e and the extravascular compartment volume, V_e, which is $V_e = V_t - V_i$, where the total tissue volume is V_t. In the extravascular compartment equation, Eq. (2.2), the net-flow of O_2 molecules includes the diffusive extraction of O_2 from the intravascular compartment (the first term on the RHS), and the O_2 consumed by mitochondria in tissue (the second term on the RHS) whose rate is $CMRO_2$ by definition. Notice that this consumption rate is independent of the amount of O_2 in the compartment.

In our measurement, both intravascular and extravascular oxygen concentrations were measured with high temporal resolution. We assume that the measurements give C_i and C_e respectively. With this information, Equation (2.2) allows us to estimate absolute $CMRO_2$ provided that V_e and PS_c are known. In practice, V_e is well

constrained [32, 91, 121], and consequently its fractional error affects $CMRO_2$ only marginally. However, PS_c is not very well constrained. There are a few publications in the literature wherein PS_c is either directly estimated *via* measurement or theoretically computed; prior estimates of PS_c range from 35 to 230 mL/s/100g Tissue [123].

2.4.2 Theoretical modeling of PS_c

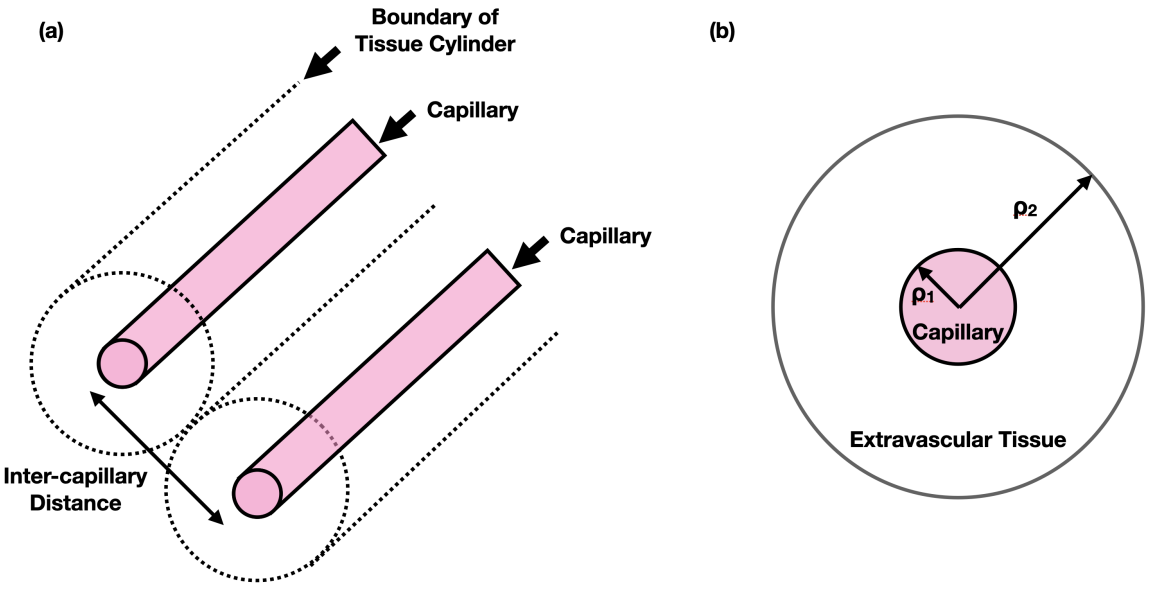

Figure 5: (a) Schematic of Krogh-Erlang cylinder model. (b) Cross-section view of a single capillary and the surrounding extravascular tissue cylindrical shell corresponding to one of the coaxial cylinders in (a).

Herein, we estimate PS_c based on an approach that uses Krogh's cylinder to model the whole tissue region (both intra- and extra-vascular tissue) as described in Fig. 5. In this modeling, each cylindrical capillary is surrounded by a coaxial extravascular cylindrical shell of tissue, and the closest neighboring capillary is placed one intercapillary distance away from one another. The capillary radius is denoted ρ_1, and the tissue outer edge radius is denoted ρ_2. Oxygen escaping from the capillary at ρ_1 will diffuse out to the edge of the extravascular tissue at ρ_2. The distance from

the capillary wall to the tissue boundary is typically set to be about one-half of the average inter-capillary distance. For a fractional volume of capillary, V_i/V_t, ρ_1 and ρ_2 are related *via* the relation below.

$$\frac{V_i}{V_t} = \left(\frac{\rho_1}{\rho_2}\right)^2. \tag{2.3}$$

Then, the length of the cylinder can be computed using ρ_2.

$$L = \frac{V_t}{\pi(\rho_2)^2}. \tag{2.4}$$

Below is the table of morphological parameters of microvasculature and tissue with a few given volume fractions of capillary.

Table 2: Radii of capillary (ρ_1), Radii of tissue cylinder (ρ_2) and corresponding length of capillary (L) are tabulated under the constraint of V_i/V_t.

ρ_1 (μm)		2.0	2.5	3.0	3.5
$V_i/V_t = 1\%$	ρ_2 (μm)	20	25	30	35
	L (km)	75.8	48.5	33.7	24.7
$V_i/V_t = 2\%$	ρ_2 (μm)	14	18	21	25
	L (km)	152	97.0	67.4	49.5
$V_i/V_t = 3\%$	ρ_2 (μm)	12	14	17	20
	L (km)	227	146	101	74.2

The other relevant physiological parameter in the model is the oxygen diffusion coefficient, D. Reported D varies from 1.4 to 1.9×10^{-5} cm^2/sec at 37^{o}C [19, 63, 52, 135]. Note, the animals used in the cited references vary from small rodent species to human brain tissue.

Having the geometrical and physiological parameters of microvasculature constrained, in steady-state, we can readily determine the concentration profile in the extravascular tissue using the diffusion equation in cylindrical coordinates. Assuming the uniform diffusion coefficient in the extravascular tissue volume, solving the

time-dependent diffusion equation below allows us to estimate oxygen concentration distribution in the extravascular tissue.

$$\frac{\partial C}{\partial t} = D\nabla^2 C - M, \tag{2.5}$$

where M corresponds to $CMRO_2$ density in the extravascular tissue; that is, $M = CMRO_2/V_e$, M is spatially uniform in the extravascular tissue volume.

To solve this problem, we must apply boundary conditions. The diffusive O_2 molecule flux at the tissue outer cylinder boundary is assumed zero in the cylindrically symmetric geometry, that is, $\frac{\mathrm{d}C}{\mathrm{d}\rho}\big|_{\rho=\rho_2} = 0$. The other boundary condition is that the concentration on the capillary wall edge is assumed to be C_i, *i.e.*, the oxygen concentration in the intravascular compartment is homogeneous. The steady-state solution to this problem was worked out by Erlang and Krogh [75] and given in by Popel [114] in more detail.

$$C(\rho) = C(\rho_1) + \frac{M}{4D}(\rho^2 - \rho_1^2) - \frac{M\rho_2^2}{2D}\ln\left(\frac{\rho}{\rho_1}\right). \tag{2.6}$$

The extravascular compartment average oxygen concentration, C_e, is found by evaluating the integral below.

$$C_e = \frac{1}{V_e}\int_{V_e} C\mathrm{d}V = -\frac{M}{2D}\left(\frac{\rho_2^4 \ln(\rho_2/\rho_1)}{\rho_2^2 - \rho_1^2}\right) + \frac{M}{8D}(3\rho_2^2 - \rho_1^2) + C(\rho_1). \tag{2.7}$$

Equation (2.6) predicts the extravascular O_2 concentration distribution in the radial direction, and Eq. (2.7) provides its average. Figure 6 shows an exemplary oxygen concentration profile in the extravascular cylinder in terms of corresponding partial oxygen pressure, mmHg, as well as the volume-averaged pO_2. In this example, $CMRO_2$ and D are set to be 3.4 μmoles/s/100g Tissue and 1.7×10^{-5} cm^2/s

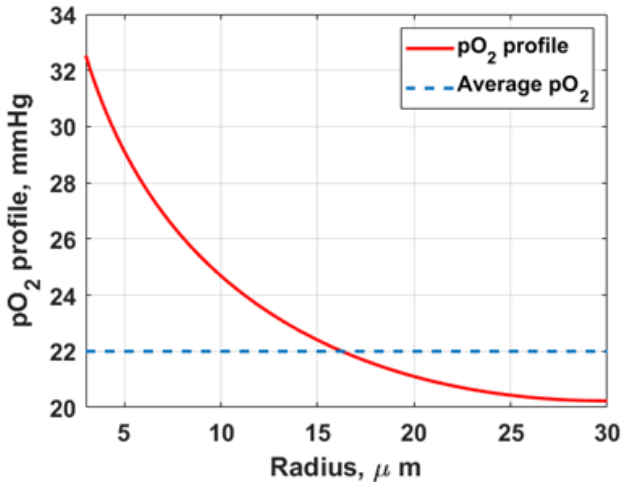

Figure 6: Oxygen concentration profile along the radial distance from the wall ($\rho_1 = 3$ μm) to the outer surface of the tissue cylinder ($\rho_2 = 30$ μm) in Krogh cylinder model.

respectively, and the average pO_2 is 22 mmHg.

Let us now summarize all of the implications of Eq. (2.7), which assumes that Krogh's cylinder model to describe the vascular system. C_e is a function of the morphological factors of microvasculature such as ρ_1 and ρ_2, as well as the physiological factor M/D. Thus, for a given capillary volume fraction and capillary radius, the average O_2 concentration is a function of M and D. Moreover, the measured C_i and C_e are precisely related to $CMRO_2$; Equation (2.7) implies that for specific C_i, C_e, morphological factors, and diffusion coefficient, there exists a unique value of M, *i.e.*, $CMRO_2$.

By trivially rewriting Eq. (2.7), we obtain an expression for M (note, $M = CMRO_2/V_e$). Below, we fill in intermediate steps to derive this expression.

$$\begin{aligned} C(\rho_1) - C_e &= \frac{M}{2D}\left(\frac{\rho_2^4 \ln(\rho_2/\rho_1)}{\rho_2^2 - \rho_1^2}\right) - \frac{M}{8D}(3\rho_2^2 - \rho_1^2) \\ &= \frac{M}{2D}\left[\frac{\rho_2^4 \ln(\rho_2/\rho_1)}{\rho_2^2 - \rho_1^2} - \frac{3\rho_2^2 - \rho_1^2}{4}\right]; \end{aligned} \tag{2.8}$$

$$M = \frac{2D}{\frac{\rho_2^4 \ln(\rho_2/\rho_1)}{\rho_2^2-\rho_1^2} - \frac{3\rho_2^2-\rho_1^2}{4}}(C(\rho_1) - C_e). \tag{2.9}$$

Substituting C_i for $C(\rho_1)$, we obtain an expression which relates molecular O_2 in the capillary and in the extravascular tissue to oxygen metabolism.

$$M = \frac{2D}{\frac{\rho_2^4 \ln(\rho_2/\rho_1)}{\rho_2^2-\rho_1^2} - \frac{3\rho_2^2-\rho_1^2}{4}}(C_i - C_e). \tag{2.10}$$

This expression above, should remind the reader of the steady-state equation for $CMRO_2$, which we derived from the coupled differential equations for the two compartments. This equation can be manipulated to define PS_c. (Note, in deriving all of the results in this section we have implicitly made the steady-state approximation.)

Since V_e is $\pi(\rho_2^2 - \rho_1^2)L$, we have

$$CMRO_2 = M \times V_e = \frac{2\pi D(\rho_2^2 - \rho_1^2)L}{\frac{\rho_2^4 \ln(\rho_2/\rho_1)}{\rho_2^2-\rho_1^2} - \frac{3\rho_2^2-\rho_1^2}{4}}(C_i - C_e) = \frac{2\pi LD}{\frac{\rho_2^4 \ln(\rho_2/\rho_1)}{(\rho_2^2-\rho_1^2)^2} - \frac{3\rho_2^2-\rho_1^2}{4(\rho_2^2-\rho_1^2)}}(C_i - C_e). \tag{2.11}$$

Thus, the model determines PS_c precisely.

$$PS_c = \frac{2\pi LD}{G\left(\frac{\rho_2}{\rho_1}\right)}, \tag{2.12}$$

$G\left(\frac{\rho_2}{\rho_1}\right)$ is a function of a ratio between capillary radius, ρ_1, and tissue radius, ρ_2. Explicitly,

$$G\left(\frac{\rho_2}{\rho_1}\right) = \frac{\left(\frac{\rho_2}{\rho_1}\right)^4 \ln\left(\frac{\rho_2}{\rho_1}\right)}{\left[\left(\frac{\rho_2}{\rho_1}\right)^2 - 1\right]^2} - \frac{3\left(\frac{\rho_2}{\rho_1}\right)^2 - 1}{4\left[\left(\frac{\rho_2}{\rho_1}\right)^2 - 1\right]}. \tag{2.13}$$

Eq. (2.13) depends only on the ratio of intercapillary distance to capillary diameter.

With caveats related to the approximations/simplifications outlined above, PS_c represents the oxygen mass transfer coefficient connecting CMRO_2 to the oxygen gradient across intra- and extravascular tissue compartments. Moreover, within this model, P and S_c can be separately defined. For example, if we take S_c to be the capillary surface area, *i.e.*, $\mathrm{S}_c = 2\pi\rho_1\mathrm{L}$, then we generate an oxygen permeability associated with tissues surrounding the capillary wall, *i.e.*, $\mathrm{P} = D/\left[\rho_1 G\left(\frac{\rho_2}{\rho_1}\right)\right]$. The function, $G\left(\frac{\rho_2}{\rho_1}\right)$, is not significantly larger than unity for typical microvascular parameters, *e.g.*, it ranges from ~ 1.1 to ~ 1.6 for typical capillary diameter and separation when V_i/V_t is between 1 and 3% (see Fig. 7)

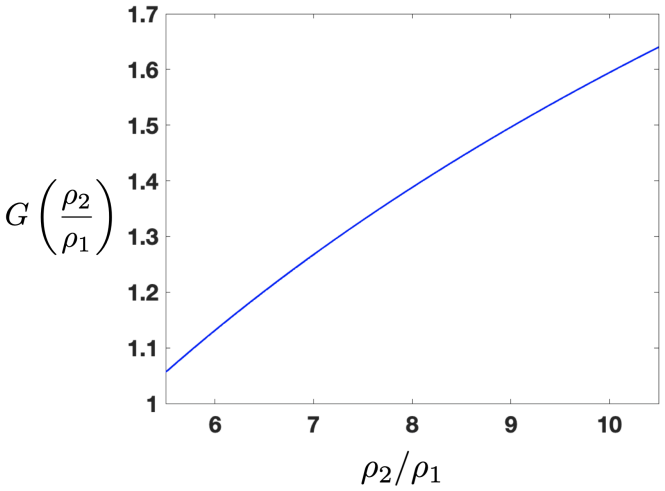

Figure 7: $G(\rho_2/\rho_1)$ as a function of ρ_2/ρ_1.

The Krogh-based model also provides an explicit relationship for the extravascular compartment relaxation time, $T_o = V_e/\mathrm{PS}_c$, in terms of ρ_1, ρ_2 and D. This timescale arises naturally in the solution of the first order differential equation, Eq. (2.2), and can be important for the description of metabolism dynamics at early times. Interestingly, the ratio of T_o to the mean-time, Δt, for oxygen to diffuse the distance ρ_2, is well defined in the model; the ratio $T_o/\Delta t$ is ranges from approximately 2.1 to 3.2 for typical system parameters, and depends only weakly on ρ_2/ρ_1 in the physiologically

relevant experimental regime (*i.e.*, V_i/V_t between 1 and 3 %). Thus, the time for the extravascular compartment to reach a new steady-state oxygen distribution following an impulse is 2× to 3× longer than the mean time it takes for oxygen to diffuse to the extravascular tissue boundary, ρ_2.

In the next Chapter, we will select PS_c based on the results of this theoretical model (using reasonable morphological and physiological parameters), on estimates of $CMRO_2$ from literature, and on our experimental values of C_i and C_e.

2.4.3 Limitations of the Model

As with many biophysical models which give exact results, the present one has potentially important limitations. For example, besides the specific numerical approximations noted above, the model ignores the heterogeneous nature of the capillary network within extravascular tissue. In practice, the capillary size, and especially the intercapillary separation, is not uniform. A slightly more complex theory should average over the distribution of regions with different morphologies. In this case, even if we continue to adopt the core cylinder model, a slightly more complex theory would quantitatively predict a distribution of PS_c and T_o. Accounting for these distributions could change the temporal metabolism dynamics, *i.e.*, compared to replacing distributions by their average values. Another limitation derives from the fact that the extravascular tissue has both neurons and other cells, and they likely have different temporal metabolic responses to stimulation. Still another limitation is the description of the capillary wall as a uniform extension of the inner capillary; for example, the oxygen diffusion coefficient in the capillary wall could be different from the surrounding tissues. All of these factors need to be considered in data interpretation. Notably, our new methodology will make confrontation of these issues possible.

Chapter 3

Optical and Surgical Methods for Probing Rat Brain Hemodynamics and Oxygen Metabolism

This Chapter has been largely adapted from a pending publication: Chong, S. H., Ong, Y. H., El Khatib, M., Allu, S. R., Parthasarathy, A. B., Greenberg, J. H., Yodh, A. G., & Vinogradov, S. A. (2022). *Real-Time Tracking of Brain Oxygen Gradients and Blood Flow during Functional Activation* [Manuscript submitted for publication]. Department of Physics & Astronomy, University of Pennsylvania.

3.1 Optical Probing Techniques

Three physiological parameters were optically tracked in our experiments. The molecular oxygen concentration in the intravascular and extravascular compartments, C_i and C_e, respectively, were acquired using the phosphorescence lifetime oximetry technique. Additionally, the relative variation of cerebral blood flow (CBF) was measured using the laser speckle contrast imaging (LSCI) technique. Their principles and associated instrumentation are introduced below.

3.1.1 Two-color phosphorescence lifetime oximetry

When a molecule is excited, it returns to the ground state *via* multiple pathways. Some pathways are non-radiative, and other pathways are radiative. If the radiation is

emitted from a triplet state, then it is called *phosphorescence* (*fluorescence* radiation is emitted from a singlet state, see Fig.8) [143]. Herein we focus on phosphorescence phenomena.

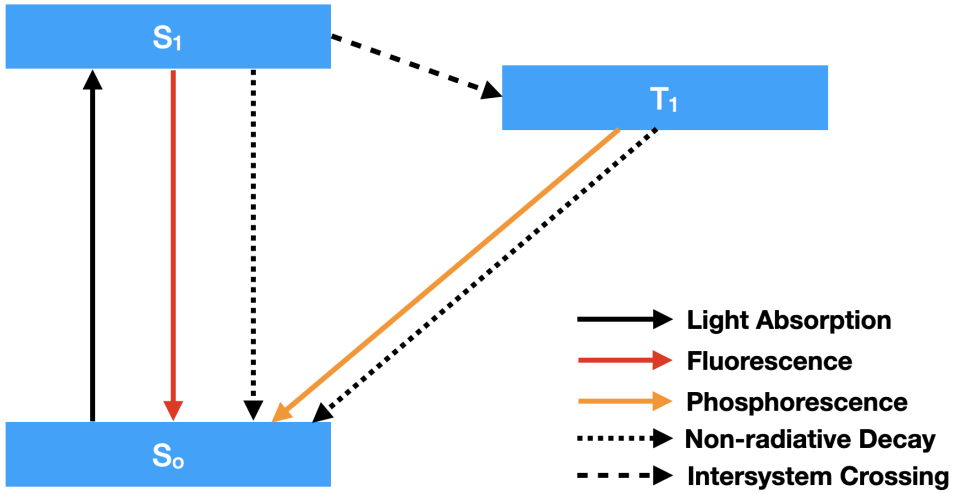

Figure 8: Simplified Jablonski Diagram. S_o: Ground State, S_1: Singlet State, T_1: Triplet State.

When a phosphor molecule in its triplet excited state experiences a collision with an oxygen molecule, the collision provides a non-radiative decay path for energy to depart from the phosphor [156]. Therefore, the more oxygen-rich environment will lead to the rapid decay of phosphorescence emission, while the less oxygen-rich environment results in a comparatively longer phosphorescence lifetime. This relationship is described by the well-known Stern-Volmer relation [131].

$$\frac{1}{\tau} = \frac{1}{\tau_o} + k_q[O_2], \tag{3.1}$$

where τ, τ_o, k_q and $[O_2]$ represent the phosphorescence lifetime, the lifetime in the absence of oxygen, the quenching constant, and oxygen concentration respectively.

Our phosphorescence method utilizes this principle; it employs measurements of phosphorescence lifetime to deduce molecular oxygen concentration (pO_2) in the lo-

cal microenvironment. Besides the phosphor molecule (Oxyphor), our experiments require an excitation laser pulse, as well as a means to detect and temporally resolve the phosphorescence photons emitted after the arrival of the excitation pulse. This time-resolved emission signal is fit to an exponential function to determine the lifetime, which in turn provides information about molecular oxygen concentration *via* a calibration curve.

The phosphorescent probes used in this study were the Oxyphors PtG4 and PtR4. PtG4 has been used previously [80, 132, 18, 15]. PtR4 was synthesized in Sergei Vinogradov's laboratory specifically for this work (see Appendix A.2-4). PtR4 is similar to the probe PdR4 [44], except that the chromophore in PtR4 is a Pt(II) porphyrin, in place of the Pd(II) porphyrin in PdR4. The difference between Pt and Pd porphyrin-based probes has been discussed [80]. The probes were calibrated using a setup previously described [44]. The Stern-Volmer relations for both Oxyphors R4 and G4 are illustrated in Fig. 9 (Note, the figure is reprinted from Fig. 5 of Supporting Information in Ref. 44.)

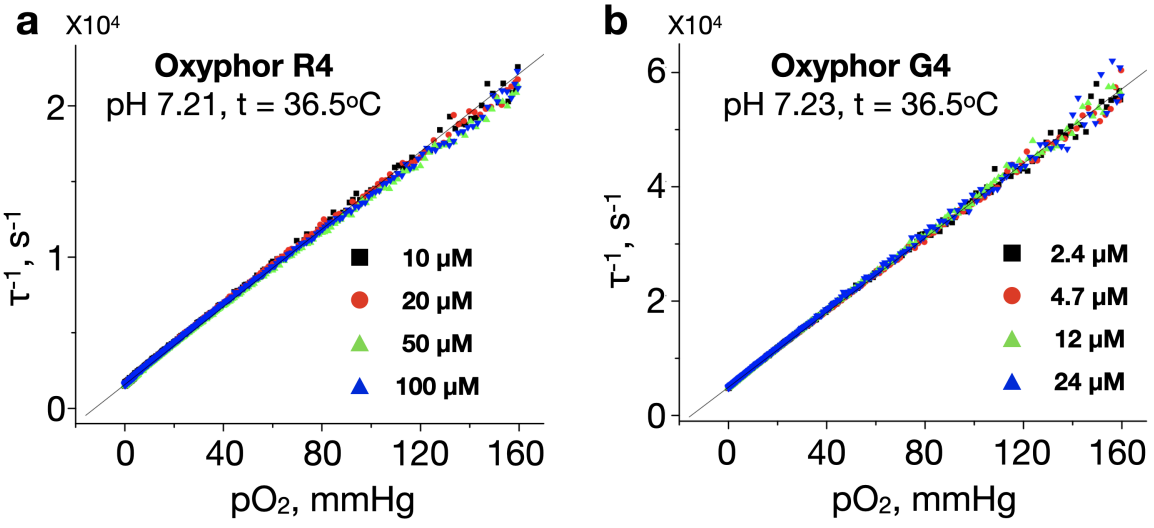

Figure 9: Stern-Volmer Relations. (a) Oxyphor R4. (b) Oxyphor G4.

The instrument for two-color phosphorometry was constructed in-house (Fig. 1a).

Briefly, the excitation sources are pulsed diode lasers (Power Technology) operating at λ_{max} = 635 nm(15 mW) and λ_{max} = 517 nm(10 mW), for excitation of PtG4 and PtR4, respectively. Both diode lasers have a rise-time and fall-time of $\sim$ 20 ns, much shorter than the pulse duration. Avalanche photodiodes (APDs) are employed for light detection (C12703-01, Hamamatsu; rise-time / fall-time $\sim$ 3.4 μs). We will use the term channel to refer to the combination of a diode laser, optical fiber for transmitting phosphorescence light to the detector (see below), a set of optical filters, and the APD. The instrument had two channels (Ch1, Ch2). The control of data acquisition was performed by a digital board (NI USB-6351, National Instruments; 1 MHz), which communicated with the host computer *via* USB interface. The data-acquisition and -analysis software was written in C/C++ (Qt, Nokia).

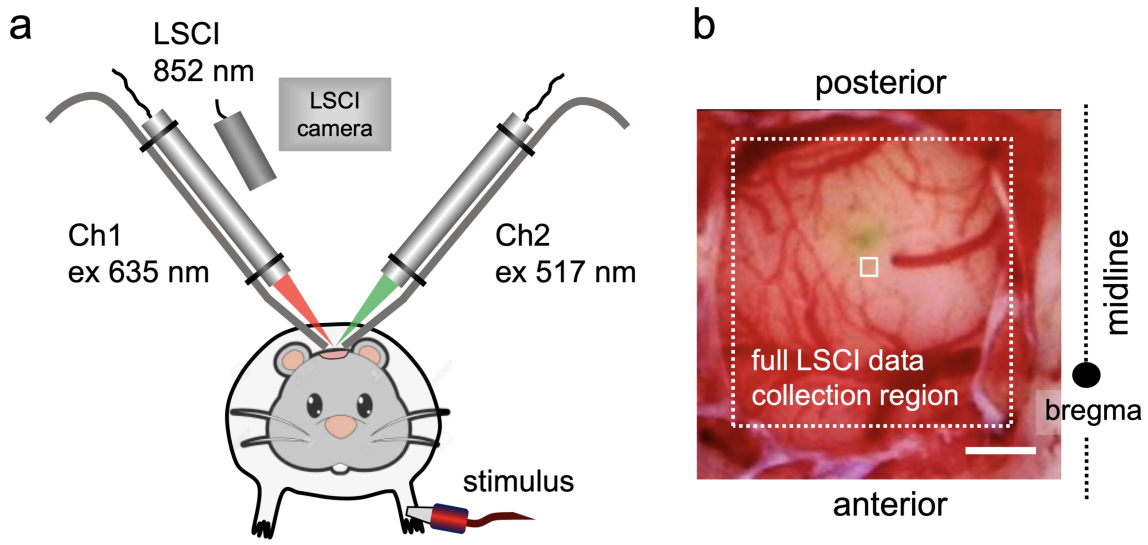

Figure 10: (a) Scheme of the experimental setup. (b) Wide-field image of the craniotomy window over the somatosensory area. Scale bar: 1 mm.

The light beams from both lasers (Ch1 and Ch2) were focused by lenses (f = 60 mm, $\varnothing$= 12 mm) to the same spot (size of $\sim$ 0.2 mm) on the brain surface; the spot (marked in the white square in Fig. 10b) resided within the region of the cortex responsible for forepaw responses, and it was located $\sim$ 300 μm away from the probe

injection site (seen as a greenish area). Phosphorescence signals were collected by single-core plastic fibers ($\varnothing$= 4 mm, Fiberoptic Technology), whose tips were held $\sim$ 2 mm from the excitation spot (Fig.10a). The phosphorescence in each channel was passed through a series of optical filters and focused by a spherical lens ($\varnothing$= 10 mm) onto the APD entrance aperture. The configuration of the optical filters in the channels is presented in Appendix A.5.

To measure pO_2 in the intravascular and extravascular compartments, one phosphorescent probe was injected into the vasculature, and the other was injected directly into the interstitial space of the brain tissue. A single data acquisition cycle (duration $T = \delta t + \Delta t$) consisted of an excitation pulse (δt = 20 μs) , during which the laser was on, followed by the phosphorescence collection period ($\Delta t = 280\mu$s), during which the APD current was digitized and recorded (Note, δt can be adjusted, typically between 10 and 30 μs, depending on the phosphorescence light level, but T is always set to 300 μs). To increase the signal-to-noise ratio (SNR), multiple cycles (N) were executed in sequence, after which the resulting data array was transferred to the computer. The collected phosphorescence decays were averaged and analyzed by single-exponential fitting. The single decay curves for PtR4 and PtG4 are shown in Fig. 11. The resulting phosphorescence decay time (τ) was converted to pO_2 using a Stern-Volmer-like equation. Note, because of the instrument response function of the APD, the fitting conservatively only includes phosphorescence intensity data collected 20 μs termination of excitation light pulse (see Fig. 11). Once a measurement in one channel was completed, it was followed immediately by a measurement in the other channel. The oxygen gradient ($\Delta[O_2]$), defined here as the difference between volume-averaged $\alpha_i\times$ p_iO_2 and $\alpha_e\times$ p_eO_2 ($\Delta[O_2]= \alpha_i\times$ p_iO_2 - $\alpha_e\times$ p_eO_2), where α_i and α_e are oxygen solubility in blood plasma and in cerebrospinal fluid respectively, was computed from the values in the two channels.

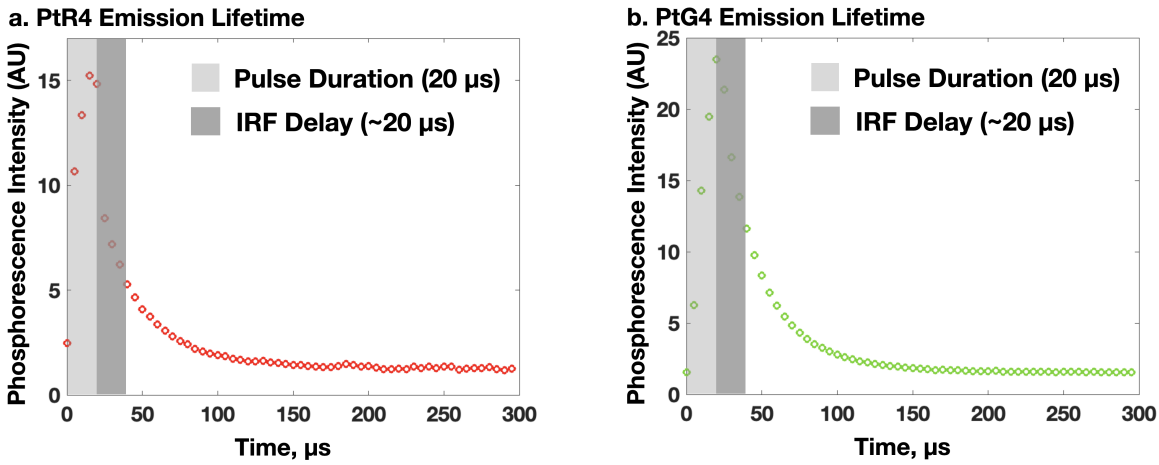

Figure 11: Example phosphorescence emission single decay curves for (a) PtR4 and (b) PtG4.

For typical acquisition settings (*e.g.*, T=300 μs, N=30), the data collection time for each channel was $\sim$ 10 ms, and the data transfer/analysis required another $\sim$ 10 ms. However, due to hardware limitations, the maximum repetition rate for our two-channel acquisition was 7 Hz ($\sim$ 70 ms per channel). This significant "dead time" was caused by the internal operation of the digital board, which had to undergo a reset for each measurement cycle. In the future, with more efficient hardware and optimized collection geometry, the measurement rate can be readily increased to $>$ 50 Hz.

3.1.2 Laser speckle contrast imaging

Temporal speckle analysis. In this section we briefly describe the theory of dynamic light scattering as it pertains to our work. (Much of this section is written informally and is not meant to be comprehensive; the interested reader is invited to read more about these ideas in the cited references.) In our experiments, we shine coherent light onto a tissue sample. The tissue contains many tiny structures that scatter light, (*e.g.*, nuclei, red blood cells, mitochondria). Generally, some of

these structures are moving significantly and some are not. The diffuse reflection is thus composed of a superposition of the scattered fields from all of these microscopic structures in the tissue. If a single speckle (diffraction limited spot) is collected in reflection, then its time-dependent intensity is related to the local electric field at the same location in the usual way:

$$I(t) = E(t)E^*(t). \tag{3.2}$$

Here t is time. The total electric field, $E(t)$, can be considered to be composed of a superposition of "micro" electric fields due, in the simplest case, to the tiny scattering structures in the illuminated tissue. (Note, for simplicity we have assumed it to be a scalar field.) Generally, the light can be scattered by *dynamic* (moving) scatterers or by *static* (not moving) scatterers. Each "micro" electric field has a phase, and the phases of the"micro" electric fields are randomly distributed and can vary with time if the scattering structures move. (See Ref. 56 for an in-depth discussion of these concepts.)

We are interested in the scattering structures that move significantly (the red blood cells). The red blood cells scatter the input light to produce "micro" electric fields with phases that vary in time; since the relative phases vary randomly in time, the sum of the "micro" electric field fluctuate too. Thus, the total detected field, $E(t)$, temporally fluctuates. Of course, the corresponding total intensity will temporally fluctuate as well. One way of characterizing these fluctuations is to measure the (normalized) temporal intensity autocorrelation function of the intensity, $g_2(t)$.

$$g_2(t') = \frac{\langle I(t+t')I(t)\rangle_t}{\langle I(t)\rangle_t^2}. \tag{3.3}$$

Here, t' is a delay time, and angled-brackets, $\langle\rangle_t$, refers to an average over time t.

In practice , it is relatively easy to measure $g_2(t)$ by photon counting techniques. However, information about scatterer motion in the sample, such as the motions of red blood cells, is typically derived from their influence on the (normalized) electric field temporal autocorrelation function, $g_1(t') = \frac{|\langle E(t)E^*(t+t')\rangle_t|}{\langle E(t)E^*(t)\rangle_t}$. Importantly, for Gaussian random fields (our case), the well-known Siegert relation [87] relates $g_2(t')$ to $g_1(t')$. The Siegert relation is given below.

$$g_2(t') = 1 + \beta|g_1(t')|^2. \tag{3.4}$$

Typically, the β coefficient above is a geometrical factor that depends on the number of speckle modes reaching the detector. If only one mode is detected, then β is one; for two modes β is one-half; etc.

The form of the electric field autocorrelation function, $g_1(t')$, depends on experimental measurement geometry and on the nature of the scatterer motion. For example, in our experiment the measurement is in the backscattering (reflection) geometry, and the light is not significantly scattered, *i.e.*, the experiment is in the single scattering regime. Moreover, the cell motion is diffusive, *i.e.*, the particle (cell) mean-square displacement is Brownian-like, except that the diffusion coefficient differs from the traditional value computed first by Einstein, and depends instead on the shear forces (maximum velocity) in the vessels. In this case, the electric field temporal autocorrelation function has a particularly simple form: $g_1(t') = \exp(-t'/t_c)$; t_c is the decorrelation time of the autocorrelation function which depends on the effective diffusion coefficient of the moving particle (cell). Note, if the light were multiply scattered, but the nature of the particle/cell motion was the same, then the functional form of $g_1(t')$ would be different, but we could still extract similar information from the decay of the correlation function, since we can predict the explicit form of the

correlation function in the multiple scattering limit. A summary of various forms for $g_1(t')$ is provided in [8].

Before discussing our LSCI experiments in more detail, we point out a few more features of the single speckle temporal intensity autocorrelation function. First, notice that in the limit of long time delay wherein t' goes to infinity, we expect $g_2(t')$ to approach 1. On the other hand, for $t' = 0$, $g_2(t')$ is larger than unity.

$$g_2(0) = \frac{\langle I(t)^2 \rangle_t}{\langle I(t) \rangle_t^2} = 1 + \frac{\langle I(t)^2 \rangle_t - \langle I(t) \rangle_t^2}{\langle I(t) \rangle_t^2} = 1 + (\kappa_t)^2; \tag{3.5}$$

and

$$\kappa_t = \frac{\sigma_t}{\langle I(t) \rangle_t}. \tag{3.6}$$

Here κ_t is called *temporal* speckle contrast, and $\sigma_t = \sqrt{\langle I(t)^2 \rangle_t - \langle I(t) \rangle_t^2}$.

Spatial speckle analysis. We next focus on LSCI, which is the correlation method used in our experiment. In LSCI, either CMOS or CCD camera is used to acquire an image of the sample that is comprised of many speckles. An average pixel count, S_i is recorded by the i^{th} pixel of the camera *via* integration of the intensity, I_i, over an exposure time, T, *i.e.*,

$$S_{i,T} = \frac{1}{T} \int_0^T I_i(t) \mathrm{d}t. \tag{3.7}$$

For LSCI, we are also interested in the fluctuations associated with the speckles. As the first step, we compute the mean and variance of $S_{i,T}$, *i.e.*, $\mathrm{E}[S_{i,T}]$ and $\mathrm{Var}[S_{i,T}]$, respectively.

$$\mathrm{E}[S_{i,T}] = \left\langle \frac{1}{T} \int_0^T I_i(t) \mathrm{d}t \right\rangle_s = \frac{1}{T} \int_0^T \langle I_i(t) \rangle_s \, \mathrm{d}t = \langle I \rangle_s ; \tag{3.8}$$

$$\mathrm{Var}[S_{i,T}] = \mathrm{E}[(S_{i,T})^2] - \mathrm{E}[S_{i,T}]^2 = \frac{1}{T^2}\int_0^T \int_0^T \langle I_i(t_1) I_i(t_2)\rangle_s \, \mathrm{d}t_1 \mathrm{d}t_2 - \langle I\rangle_s^2 \,. \quad (3.9)$$

Here $\langle\rangle_s$ refers to a spatial averaging operator, and $\langle I_i(t_1) I_i(t_2)\rangle_s$ might be recognized as an ensemble averaged version of the intensity autocorrelation function. Using the Siegert relation once more, we have $\langle I_i(t_1) I_i(t_2)\rangle_s = \langle I\rangle_s^2 [1 + \beta |g_1(t_1 - t_2)|^2]$. Combining these ideas it is straightforward to show that

$$\begin{aligned} \mathrm{Var}[S_{i,T}] &= \frac{\beta \langle I\rangle_s^2}{T^2}\int_0^T \int_0^T |g_1(t_1 - t_2)|^2 \mathrm{d}t_1 \mathrm{d}t_2 \\ &= \frac{2\beta \langle I\rangle_s^2}{T^2}\int_0^T (T - t')|g_1(t')|^2 \mathrm{d}t'. \end{aligned} \quad (3.10)$$

The intensity-normalized variance is then,

$$\frac{\mathrm{Var}[S_{i,T}]}{\langle I\rangle_s^2} = 2\beta \int_0^T \left(1 - \frac{t'}{T}\right) |g_1(t')|^2 \frac{\mathrm{d}t'}{T}, \quad (3.11)$$

which we define as the square of the *spatial* speckle contrast, κ_s. In LSCI, speckles are imaged onto the CCD *via* collection optics. Depending on the imaging, a speckle may be spread over many pixels, or a speckle might be spread over less than one pixel, or somewhere in between. For a given imaging geometry, the minimum size of a speckle is approximately the diffraction-limited spot size, $\rho_{speckle} = 2.44\lambda(1 + M)f/\#$, where λ, M and $f/\#$ are the wavelength of the coherent light source, magnification and f-number of the collection optics [10]. Therefore, the number of speckles (N) in a pixel can be computed, *i.e.*, $N =$ (Area of a pixel) / $\pi \left(\frac{\rho_{speckle}}{2}\right)^2$.

For reflection from a homogeneous collection of microscopic scatterers undergoing diffusive motion, in the single-scattering limit (which is a good approximation for our

geometry and for brain tissues), $g_1(t')$ is well approximated as exponential, *i.e.*,

$$g_1(t') = e^{-\frac{t'}{t_c}}, \tag{3.12}$$

where, in diffusive dynamics, t_c is

$$t_c = \frac{1}{q^2 D_{eff}}. \tag{3.13}$$

q is the magnitude of the scattering vector, and D_{eff} is an effective diffusion coefficient of the blood cells that is in proportion to the speed of the blood flow in the imaged tissue.

Now using Eqs. (3.11) and (3.12), the spatial speckle contrast, κ_s can be acquired.

$$\kappa_s(T) = \sqrt{\beta \frac{e^{-2\frac{t_c}{T}} - 1 + 2\left(\frac{t_c}{T}\right)}{2\left(\frac{t_c}{T}\right)^2}}, \tag{3.14}$$

As a consequence, for a specific camera exposure time, T, κ_s can be related to the characteristic decorrelation time, t_c. In the limit of large exposure time, κ_s is particularly simple. The reciprocal of t_c is in proportion to the speed of the blood cells in the tissue vasculature. In practice, it is difficult to acquire an absolute speed, and therefore relative changes are sought and are sufficient in most cases. The LSCI method has been extensively validated [9, 34, 35, 69, 109, 110, 116], and the linearity of blood flow response is well established in this geometry.

In LSCI acquisition of κ_s requires pixel sampling. In essence, we must compute the standard deviation and the mean of some small ensemble of pixel readouts, *i.e.*, σ_s, and the mean readouts $\langle I \rangle_s$, respectively. One could compute these parameters using as few as one pixel (which would require many measurements in time); in the opposite limit, one could compute these parameters using many pixels at single point

in time. In LSCI we are interested in obtaining images of fluctuations at high frame rates (e.g., video rates). Thus, in practice a compromise between accuracy and spatial resolution in the image must be made. While sampling many pixels over a broad area will stabilize the statistical accuracy of κ_s, the spatial resolution of the image is lost. By contrast, sampling from smaller areas will weaken the statistical accuracy of κ_s but will improve the spatial resolution. The working consensus of LSCI community is to use 7×7 array of pixels as a sliding window (which defines a spatial resolution for the spatial contrast image) for computation of κ_s; the 49 pixels are used to derive a mean and standard deviation of the detected pixel intensity at each location. The choice achieves both statistical significance and spatial resolution of the processed image in many practical situations [10].

In our experiment, as noted previously, a coherent laser beam illuminates the surface of the brain, and the scattered speckle from the brain is imaged onto the CMOS camera (Fig. 12a, camera pixel size is 2040×2040.) in which a majority of blood vessels are not visible except for the large veins. The detected speckle will fluctuate due to motion in the brain, *e.g.*, due to blood flow. Thus, in the spatial regions with significant blood flow, speckles will fluctuate more than in spatial regions with less blood flow. LSCI measures the speckle contrast associated with these different regions. For our analysis, the camera exposure time was set to 5 ms, and a 7×7 moving window was used to compute κ_s at different spatial positions over the whole raw image. For example, in Fig. 12b, the flow information derives from the speckle contrast (the speckle variance) in each region, *i.e.*, low and high speckle contrasts correspond to fast and slow blood flow respectively; the red arrow indicates a pial artery where the flow is fast, and the blue arrow indicates a region where there is no major vessel. Note, in our experiments, the speckle contrast did not have to be computed for the whole field of view; we only needed to investigate a smaller region

of interest wherein functional activation occurred (marked in the white square region of 200 μm$\times$200 μm in Fig. 10b).

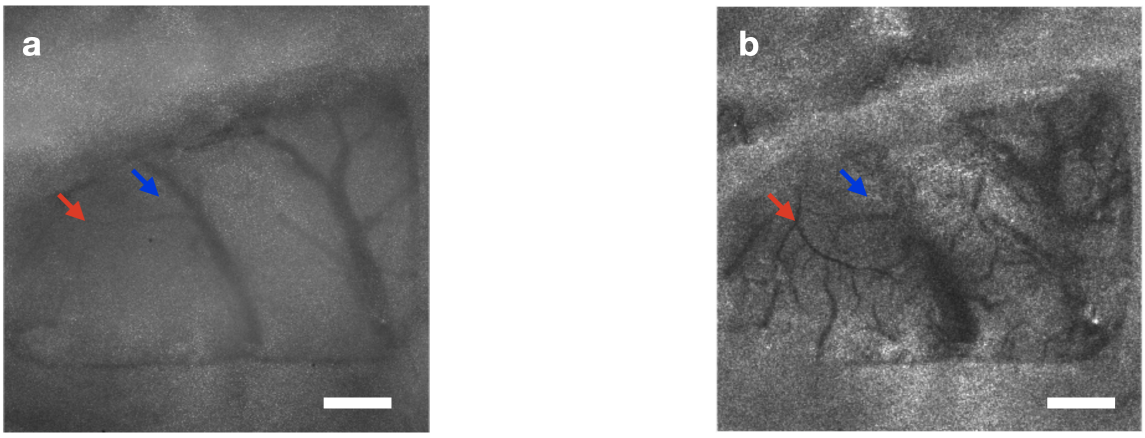

Figure 12: Examples of (a) a raw speckle image, and (b) speckle contrast processed image. Scale bar indicates 1 mm.

Once κ is computed, it is then related to the decorrelation time, t_c whose reciprocal is essentially proportional to local blood flow in tissue region. In the experiments, a diode laser (852nm, 600mW, LD852-SE600, Thorlabs) was positioned at a distance of $\sim$ 20 cm from the brain surface, and its beam was directed at a $\sim$ 45^o angle relative to the surface normal. The brain was imaged using a CMOS camera (acA2040-180km, Basler AG, Germany) equipped with infinity-corrected optics. Images were acquired at the rate of 20 Hz using custom-written software (LabView, National Instruments). The LSCI field-of-view (FOV) was quite large: 6.2 mm $\times$ 6.2 mm; the FOV encompassed the functional activation region and the focal spot used for the phosphorescence oximetry. LSCI data were analyzed to quantify relative changes of CBF in the brain cortex [39].

3.2 Surgical Preparation

Twelve adult male Sprague-Dawley rats ($250 - 400$ g) were used in this study. A rat was anesthetized *via* inhalation of a nitrogen:oxygen (70:30) mixture containing isoflurane ($\sim 4\%$ for induction, and $\sim 1.5\%$ for maintenance). A catheter was placed into the left femoral artery for continuous monitoring of the arterial blood pressure. The same catheter was used for injection of the phosphorescent probe for intravascular pO_2 measurements, as well as for injections of saline to maintain hydration. The animal's head was fixed in a stereotaxic frame, and the intracranial pressure of the rat brain was normalized through *cisterna magna*. Afterward, a cranial window was made in the skull (6 mm×4 mm) over the forepaw somatosensory area (Fig. 10b) using a saline-cooled dental drill. The dura mater was removed, after which the exposed brain surface was continuously irrigated with artificial cerebrospinal fluid heated to $\sim 37^oC$ (see Appendix A.1 for ingredients). After the craniotomy was completed, α-chloralose was administered intraperitoneally (60 mg/kg), and the isoflurane dose was gradually decreased and then discontinued over a period of 30 min. Anesthesia was maintained by supplemental doses of α-chloralose (30 mg/kg, ~ 1 dose/hr). Two electrodes for electrical stimulation were inserted sub-dermally into the left forepaw contralateral to the craniotomy site (Fig. 10a). The body temperature was monitored with a rectal probe and was maintained at 37.4 ± 0.2^oC using a heating pad controlled by a homeothermic monitoring system (Harvard Apparatus, MA). A detailed timeline is summarized in Fig. 13. The animals were under the care of the University of Pennsylvania Laboratory Animal Resources. All studies were approved by the University of Pennsylvania Institutional Animal Care and Use Committee.

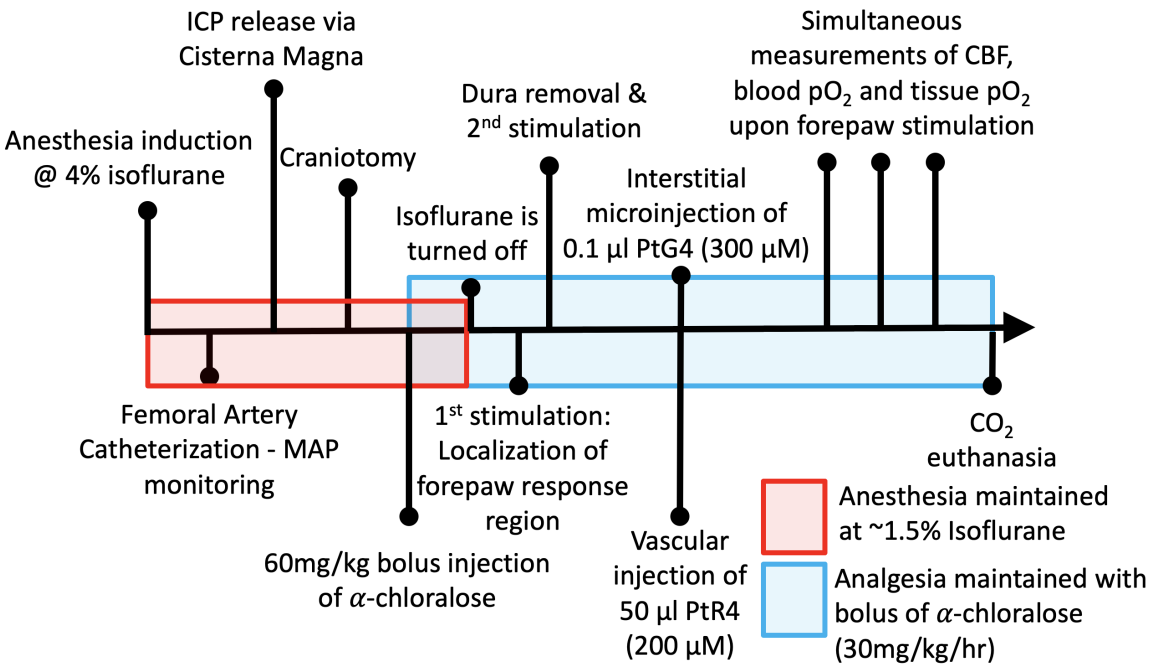

Figure 13: Protocol of the surgical procedure and measurement.

3.3 Experimental Sequence

First, the animal's forepaw was stimulated using an electric current from a stimulus isolator (1.5 mA, 1 ms-long pulses at 3 Hz, stimulation time 4 s), and LSCI data was collected and analyzed [39] to locate the somatosensory cortex region within the exposed craniotomy window before and after removal of the dura mater. Oxyphors PtR4 and PtG4 were administered as solutions in physiological saline. PtR4 was administered intravascularly *via* femoral catheter (50 μL, 200 μM), and PtG4 (0.1 μL, 300 μM) was administered by direct injection into the brain tissue using a microinjection dispenser (Picospritzer III, Parker Hannifin Precision Fluidics Division, NH) and a micropipette (tip diameter $\sim$ 15 μm). The micropipette was inserted to a depth of $200 - 300$ μm, and the Oxyphor solution was injected at a rate of ~ 0.1 μL/min. Subsequently, electrical stimulation/blood flow measurement by LSCI was repeated

to confirm that functional responses persisted. The assemblies for phosphorescence measurements were positioned above the cranial window (Fig. 10b) and phosphorescence signals were measured. If necessary, the amount of intravascular probe was increased by injecting additional solution through the catheter.

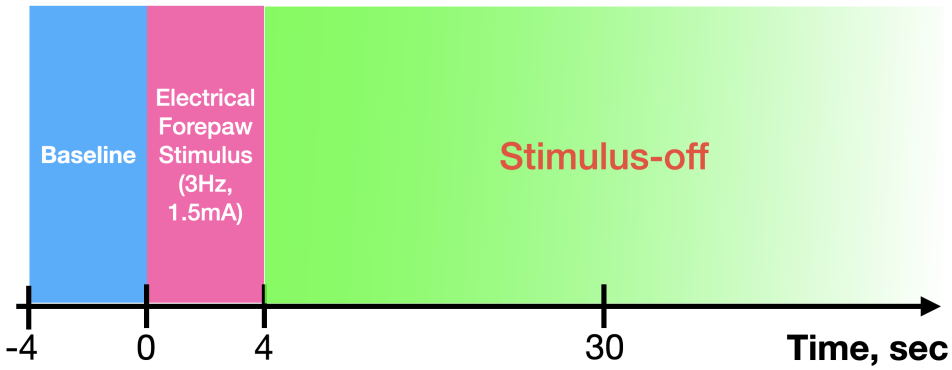

Figure 14: Scheme of the experiment protocol

Each stimulation cycle was 1 minute. The stimulation cycle consisted of 4 second baseline monitoring, followed by the application of 4 second stimulus (1.5 mA, 1 ms-long pulses at 3 Hz), and then a 52-second recovery. Up to 15 sequential stimulation cycles were applied, during which lifetime and LSCI data were recorded (Fig. 14 is a block diagram of the procedure).

Chapter 4

Dynamics of Oxygen Metabolism and Blood Flow in Rat Brain

This Chapter has been largely adapted from a pending publication: Chong, S. H., Ong, Y. H., El Khatib, M., Allu, S. R., Parthasarathy, A. B., Greenberg, J. H., Yodh, A. G., & Vinogradov, S. A. (2022). *Real-Time Tracking of Brain Oxygen Gradients and Blood Flow during Functional Activation* [Manuscript submitted for publication]. Department of Physics & Astronomy, University of Pennsylvania.

4.1 Two-color, Two-Oxyphor Measurement Method

In our work, we demonstrated a novel application of the phosphorescence quenching method [145] which facilitates concurrent measurement of oxygen concentrations in both intravascular and extravascular compartments of rat brain. This approach enables us to determine vascular oxygen gradients. Critically, we identified two dendritic polyethyleneglycol (PEG)-coated phosphorescent probes, Oxyphors [80, 44] which do not cross through the blood-brain barrier [118, 82, 44, 43, 132], and which have minimally overlapping absorption and emission spectra (see Fig. 15. The laser lines (635 nm and 517 nm) of the respective channels and the LSCI laser line (852 nm) are shown by vertical bars. The absorption spectra are scaled by the respective extinction coefficients at absorption peaks (ε_{620}(PtG4)$\simeq 1.0 \times 10^5$ $M^{-1}cm^{-1}$, ε_{510}(PtR4)$\simeq 2.0 \times 10^4$

$M^{-1}cm^{-1}$). The emission spectra are scaled such that their areas are proportional to the probes' phosphorescence quantum yields ($\eta_{PtG4} = 0.067, \eta_{PtR4} = 0.052$). The emission wavelength ranges isolated by the optical filters and seen by the detectors in Ch1 (PtG4) and Ch2 (PtR4) are shown by the shaded areas.) In our experiments, we demonstrated that the phosphorescence lifetime signals from the two probes can be retrieved with minimal cross-talk, and since one probe circulated in the blood and the other resided in the extravascular space, we showed that intravascular and extravascular pO_2 can be measured concurrently.

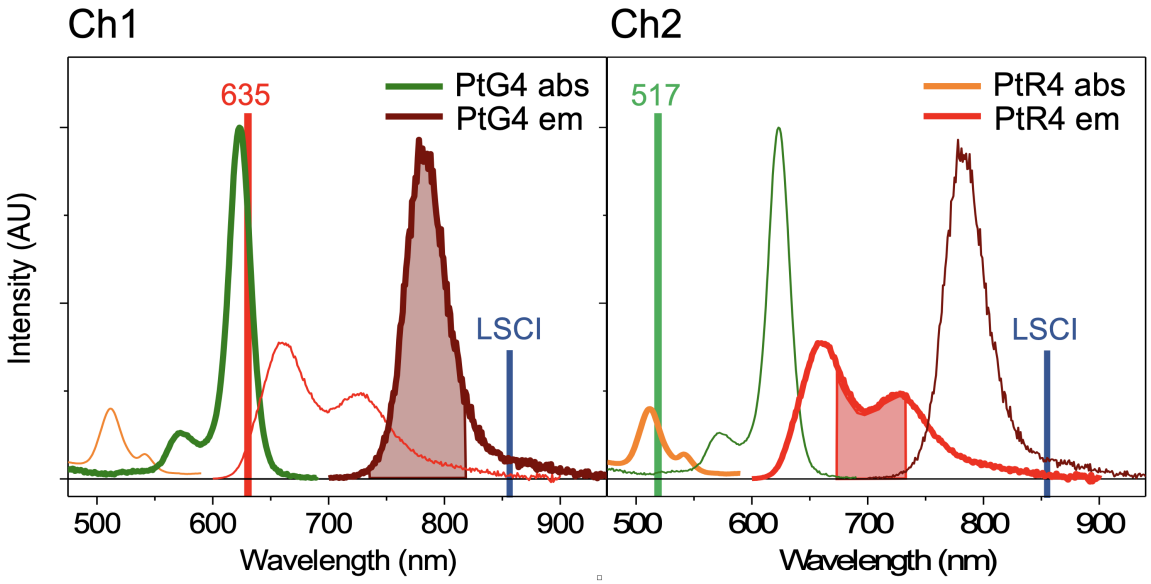

Figure 15: Optical absorption and phosphorescence spectra of Oxyphors PtG4 (Channel 1) and PtR4 (Channel 2).

A major experimental challenge for this work was to minimize optical cross-talk between two Oxyphors while preserving enough Oxyphor signal to derive the vascular oxygen gradient. Although excitation of PtR4 and PtG4 Oxyphor mixtures at 635nm produced only PtG4 phosphorescence (Fig. 15), the laser excitation at 517nm, aimed at the Q-band of PtR4, induced a weak but non-negligible emission from PtG4. Thus, multiple optical filters were needed to remove unwanted signals from each channel (see

Appendix A.5); use of these filters sacrificed $\sim$ 40% of the PtR4 phosphorescence spectrum. This effect, in conjunction with the lower molar extinction coefficient and phosphorescence quantum yield of PtR4 (Fig. 15), caused the PtR4 signal to be 10 to 15 times weaker than that of PtG4 *in vitro* , even when equal amounts of the probe were dissolved in water. *In vivo*, this difference was further exacerbated by attenuation at 517 nm due to endogenous tissue absorption.

Thus it was necessary to increase the PtR4 concentration in brain by a factor of 10$\times$ more than PtG4. Even still, the PtR4 phosphorescence signal was $\sim$ 10 to 20 times weaker than PtG4. Consequently, noise in Ch2 (Fig. 15) was significantly higher than in Ch1, irrespective of whether PtR4 was injected into the blood or interstitial space. Generally, the p_eO_2 extravascular signal had $\sim 3\times$ better signal-to-noise compared to the p_iO_2 intravascular signal, due to the optical advantages of PtG4 described above. Despite this challenge, oxygen (pO_2) readings were obtained at a rate of 7 Hz for the two channels and were sufficient to resolve transients in respiratory and vascular activity upon neuronal activation. In the experiments producing the best signal-to-noise, PtR4 was delivered intravascularly. This approach permitted us to increase PtR4 concentration *via* additional injections during the experiments through the catheter, if necessary.

4.2 Longitudinal Measurement Results

An example of raw unprocessed traces of p_eO_2 (Ch1/PtG4), p_iO_2 (Ch2/PtR4), and CBF during a series of stimulations is shown in Fig. 16a. Notably, we obtained useful single-shot data-waveforms for each electrical stimulation. All three parameters exhibited a sharp rise after stimulation, followed by a more gradual decrease to baseline levels at longer times. Between each pair of stimulations, we paused recording of pO_2; this minimized brain exposure to excitation light and possible associated

phototoxicity (Fig. 16b).

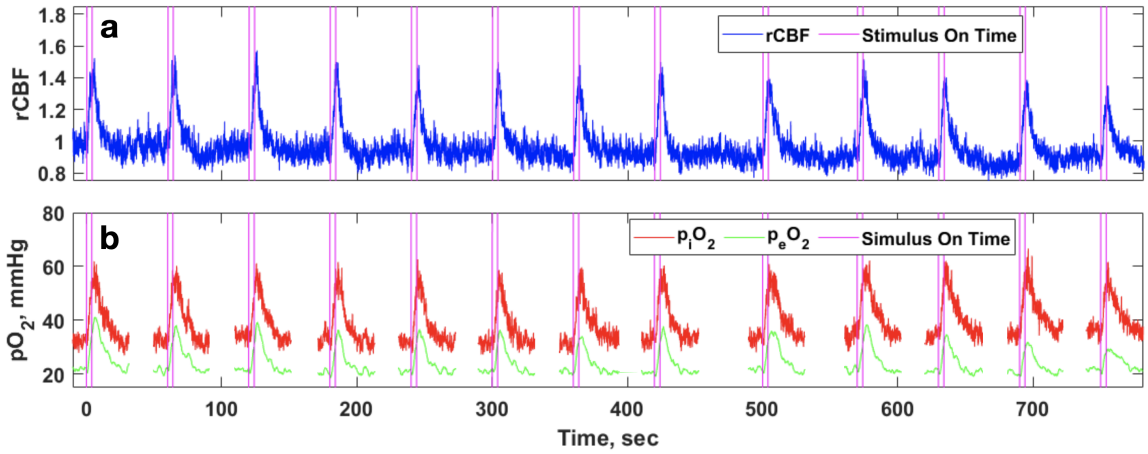

Figure 16: Raw unprocessed data obtained in an experiment consisting of 13 consecutive forepaw stimulations, accompanied by (a) CBF, (b) p_iO_2, and p_eO_2 measurements in the somatosensory area of the rat brain.

In Fig. 17, we exhibit superposed traces of p_eO_2 synchronized at the start of the electrical stimulation ($t = 0$). Each color represents a different stimulus trial, and the stimulation period is shown by a pink rectangle (this convention is consistent throughout Chapter 4.) Notice that immediately upon the start of stimulation, p_eO_2 exhibits a characteristic "initial dip" caused by the rapid increase in the local oxygen consumption by activated neurons. Remarkably, the dips could be seen in practically all individual stimulation events. On average, the dip magnitude was approximately $9\pm2\%$ of the average peak p_eO_2; the minima occurred approximately 0.8 ± 0.1 sec after the onset of stimulation. Dip minima occurrence times in previous microscopy studies are in a similar range [82, 30], but these assignments typically required averaging of hundreds of simulation trials. In the present case, the signals were strong in part because they originated from a large excitation volume that likely encompassed the entire activation region. However, this volume probably included cells whose oxygen consumption is less than that of neurons upon activation. The measured dip amplitude should therefore be expected to fluctuate, especially since illumination

areas could include greater/smaller volume fractions of neurons.

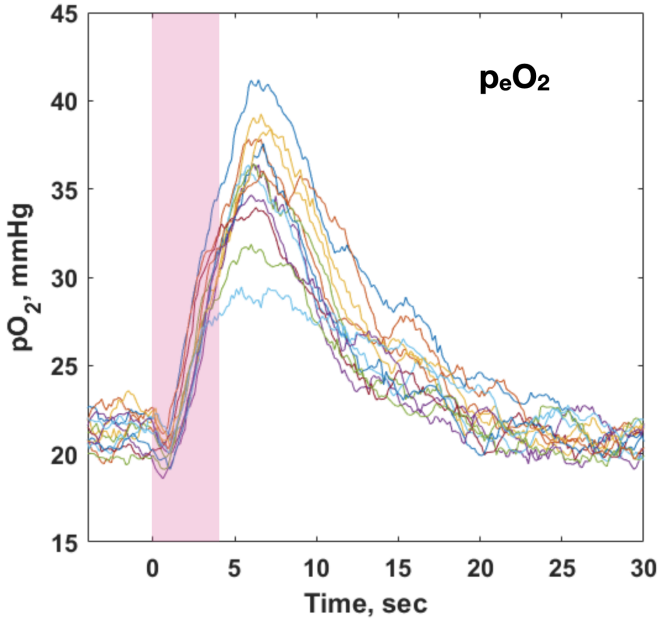

Figure 17: Overlapping traces of p_eO_2.

Per quantification of oxygen gradients, the average baseline intravascular oxygen partial pressure (p_iO_2) was 33.5 ± 0.5 mmHg (mean, standard deviation of the mean). This number is on the lower side of the range of intravascular pO_2 values reported previously [118, 82, 30, 43, 94], possibly due to the use of α-chloralose as an anesthetic. Anesthesia is known to have pronounced effects on tissue pO_2 [94, 159]. The average baseline extravascular oxygen partial pressure (p_eO_2) clustered around 21.3 ± 0.2 mmHg. Therefore, the resulting intra-/extra-vascular pO_2 drop was 12.2 ± 0.4 mmHg.

In previous studies of rat brain, utilizing 2PLM and isoflurane as anesthetic, pO_2 drops of $\sim$ 15 mmHg were seen over 25 μm distances from large single arterioles, corresponding to the gradients of ~ 0.6 mmHg/μm [119]. Measurements around capillaries of a rat brain using microelectrodes (with pentobarbital anesthesia) produced somewhat lower gradients, ~ 0.45 mmHg [148]. In the present case, p_iO_2 is derived mainly from capillaries, since the total volume of blood in capillaries is larger, and

since excitation of the phosphorescent probe in thin capillaries is much more efficient than in large vessels. Our measured p_eO_2 represents a volume average over the entire extravascular space within the excitation volume. If we assume that the average intercapillary distance is 60 μm [85, 12], then our results give a gradient of $\sim$ 0.8 mmHg/μm. Note, the measurements of p_iO_2 and/or p_eO_2 are also subject to systematic errors (see Section 4.4), which will need to be further analyzed/corrected for as the method develops.

4.3 Selection of PS_c and Computation of Dynamic $CMRO_2$

4.3.1 Data-constrained selection of PS_c

For our calculations we choose $PS_c = 210$ [mL/sec/100g tissue]. In this subsection, we describe in detail the rationale we used to arrive at the choice, which was based on morphological and physiological considerations in the published literature. The reader who is not interested in these details is invited to skip to the next subsection. The reader who is interested in this selection should read on, in part because the full analysis exposes internal consistencies in the theory and the importance of particular assumptions.

The cylindrical model for capillary and surrounding tissue enables determination of PS_c based on the full range of reported $\rho_1, \rho_2, V_i/V_t$, and D and Eq. (2.12). The resulting "allowed" variation of PS_c spans widely from 137 to 2470 mL/sec/100g tissue. Tables 3-5 show the values of PS_c (in bold) as a function of $\rho_1, \rho_2, V_i/V_t$, and D; note ρ_2 is fixed by choice of ρ_1 and V_i/V_t. This potential variation of PS_c thus deduced is larger than the range of values reported in the literature, and does not

entirely overlap with the range of values reported in the literature.

Table 3: PS_c (Bold), $CMRO_2$ vs D, ρ_1, ρ_2 for intravascular volume fraction, V_i/V_t of 0.01(1%). PS_c values [mL/sec/100g Tissue] computed from (2.12) as a function of D [10^{-5}cm^2/sec], ρ_1 and ρ_2 [μm]. Baseline $CMRO_2$ values [μmoles/sec/100g Tissue] are computed according to (2.11) using the PS_c based on different values of D [10^{-5}cm^2/sec] and ρ_1 [μm]. The green-shaded cells correspond to baseline $CMRO_2$ values that are consistent with a range of prior measurements.

D \ ρ_1 / ρ_2	2.0 / 20	2.5 / 25	3.0 / 30
1.4	**418**, 7.1	**268**, 4.5	**186**, 3.2
1.5	**448**, 7.6	**287**, 4.9	**199**, 3.4
1.6	**478**, 8.1	**306**, 5.2	**212**, 3.6
1.7	**508**, 9.1	**325**, 5.5	**226**, 3.8
1.8	**538**, 9.6	**344**, 5.8	**239**, 4.1
1.9	**568**, 9.6	**363**, 6.2	**252**, 4.3

Table 4: PS_c (Bold), $CMRO_2$ vs D, ρ_1, ρ_2 for intravascular volume fraction of 0.02(2%). PS_c values [mL/sec/100g Tissue] computed from (2.12) as a function of D [10^{-5}cm^2/sec], ρ_1 and ρ_2 [μm]. Baseline $CMRO_2$ values [μmoles/sec/100g Tissue] are computed according to (2.11) using the PS_c based on different values of D [10^{-5}cm^2/sec] and ρ_1 [μm]. The green-shaded cells correspond to baseline $CMRO_2$ values that are consistent with a range of prior measurements.

D \ ρ_1 / ρ_2	2.0 / 14	2.5 / 18	3.0 / 25	3.5 / 28
1.4	**1040**, 17.9	**669**, 11.5	**464**, 8.0	**341**, 5.8
1.5	**1120**, 19.2	**716**, 12.3	**497**, 8.5	**365**, 6.3
1.6	**1190**, 20.5	**764**, 13.1	**531**, 9.1	**390**, 6.7
1.7	**1270**, 21.7	**812**, 13.9	**564**, 9.7	**414**, 7.1
1.8	**1340**, 23.0	**860**, 14.7	**597**, 10.2	**439**, 7.5
1.9	**1420**, 24.3	**907**, 15.5	**630**, 10.8	**463**, 7.9

Table 5: PS_c (Bold), $CMRO_2$ vs D, ρ_1, ρ_2 for intravascular volume fraction of 0.03(3%). PS_c values [mL/sec/100g Tissue] computed from (2.12) as a function of D [10^{-5}cm^2/sec], ρ_1 and ρ_2 [μm]. Baseline $CMRO_2$ values [μmoles/sec/100g Tissue] are computed according to (2.11) using the PS_c based on different values of D [10^{-5}cm^2/sec] and ρ_1 [μm]. The green-shaded cells correspond to baseline $CMRO_2$ values that are consistent with a range of prior measurements.

D \ ρ_1 / ρ_2	2.0 / 12	2.5 / 14	3.0 / 17	3.5 / 20
1.4	**1820**, 31.5	**1170**, 20.2	**810**, 14.0	**595**, 10.3
1.5	**1950**, 33.8	**1250**, 21.6	**867**, 15.0	**637**, 11.0
1.6	**2080**, 36.0	**1330**, 23.1	**925**, 16.0	**680**, 11.8
1.7	**2210**, 38.3	**1420**, 24.5	**983**, 17.0	**722**, 12.5
1.8	**2340**, 40.6	**1500**, 26.0	**1040**, 18.0	**765**, 13.2
1.9	**2470**, 42.8	**1580**, 27.4	**1110**, 19.0	**807**, 14.0

To further constrain PS_c, we next utilize prior measurements of baseline (normal) $CMRO_2$, and our absolute measurements of intravascular and extravascular compartment pO_2. Specifically, our measurements of baseline intravascular and extravascular compartment partial pressures found mean values of $p_iO_2 = 33.5$ mmHg and $p_eO_2 = 21.3$ mmHg (Fig. 16). Using these partial pressures, we can readily compute baseline volume-averaged C_i and C_e. Finally, using the reported range of baseline $CMRO_2$ and Eq. (2.11), *i.e.*, using the result $CMRO_2 = PS_c\ (C_i - C_e)$, we identify a much smaller subset of PS_c which satisfy Eq. (2.11) subject to published constraints on tissue morphology and oxygen diffusion.

These results are summarized in Tables 3 - 5, which show the predicted $CMRO_2$ as a function of $\rho_1, \rho_2, V_i/V_t$, and D for the cases where $3 < CMRO_2 < 7.4$ [41, 134, 150, 73]. The **green shaded rectangles** in the tables correspond to the allowed range of values of $CMRO_2$. Note, PS_c is given in bold text, next to $CMRO_2$ in these green shaded rectangles.

Taken together, our modeling and analysis suggest that PS_c has a value constrained approximately to the range from 180 to 430 [mL/sec/100g tissue]. The

choice of PS_c amongst this range of possibilities has consequences for the magnitude and dynamical response of $CMRO_2$. For our calculations we choose PS_c = 210 [mL/sec/100g tissue]. In making this selection, we used morphological and physiological parameters towards the middle of the reported ranges; for example, $D \simeq 1.6 \times 10^{-5}$ cm^2/s and $\rho_1 = 3.0$ μm and $\rho_2 = 30$ μm. Note also, this selection of 210 mL/sec/100g tissue is similar to the value of PS_c found in the only study of rat brain [67] that had a pO_2 ($\sim$ 25 mmHg) comparable to our experiments ($\sim$ 21 mmHg). Lastly, note that this choice is also within the range used in all prior studies; the prior studies suggest that PS_c has a value between 35 and 230 mL/sec/100g tissue [55, 59, 68, 112, 136, 142, 123, 67]. We caution the reader, however, because a small change of ρ_1 and ρ_2 to 2.5 μm and 25 μm, respectively, gives $PS_c \sim 300$ [mL/sec/100g tissue]. Ultimately, to ameliorate this problem, the community will need to carry out more experiments and analyses to further constrain PS_c.

4.3.2 Computation of $CMRO_2$

With the value of PS_c (210 [mL/sec/100g tissue]) now determined, estimation of $CMRO_2$ is mathematically straightforward using Eq. (2.2). An example of resultant $CMRO_2$ is given in Fig. 18a. Recall that in contrast to prior work [61, 35, 39, 4, 86], our experiments demonstrate dynamic tracking of $CMRO_2$ before, during, and after stimulation based on measurements of oxygen gradients; this approach enables us to dynamically measure $CMRO_2$ without reliance on CBF. Importantly, we also independently obtained concurrent traces of CBF response. Thus, our measurements provide a unique opportunity to compare the response of all four parameters, CBF, p_iO_2, p_eO_2, and $CMRO_2$. This capability offers physiologically important information not available to other methodologies. Especially, our ability to independently determine

C_i, C_e, and their time derivatives in Eq. (2.2) distinguishes the new methodology from prior analyses of $CMRO_2$ dynamics.

In previous work, because experimental determination of the derivatives, dC_c/dt in Eq. (2.1) and dC_e/dt in Eq. (2.2), was difficult or inaccessible, $CMRO_2$ was computed from only the instantaneous values of CBF and C_a - C_v [164, 61, 35, 39, 25]. Therefore, steady-state conditions were inevitably assumed, which leads to the popular definition: $CMRO_2 = CBF \times (C_a - C_v)$. To distinguish between the older and present methods we introduce the terms *full-dynamic* and *truncated-dynamic* $CMRO_2$. Full-dynamic $CMRO_2$ is computed from the data using the full model, Eq (2.2) that includes the time derivative, dC_e/dt. Truncated-dynamic $CMRO_2$ is computed using Eq. (2.2) but ignoring the time derivative, which is equivalent to $CMRO_2 = CBF \times (C_a - C_v)$. Additionally, inclusion of the time-derivative introduces an exponential extravascular compartment time constant, $T_o = V_e/PS_c$, which can affect relative delays between the temporal responses of p_iO_2, p_eO_2, CBF, and that of $CMRO_2$.

In practice, V_e is well constrained by previous experiments, and its variation only marginally affects $CMRO_2$ response. By contrast, PS_c affects both the magnitude of $CMRO_2$ and its temporal dynamics, and PS_c is not as well constrained by previous experiments (*i.e.*, compared to V_e). We illustrate these effects in Fig. 19a. The responses shown in Fig. 19a are obtained by Gaussian low-pass filtering (Fig. 18, the raw data is marked in gray while de-noised traces are in colors, and each trace is gaussian low-pass filtered (FWHM=300 msec) for analysis of temporal dynamics) and averaging the 13 stimulation-induced p_eO_2 and p_iO_2 profiles (Fig. 16b) and, then, solving Eq. (2.2) (with and without including the time derivative) for $CMRO_2$ with the same inputs but different PS_c. Figure 19a exhibits the variation of full- and truncated-dynamic $CMRO_2$ at three different numerical values of PS_c $(80, 210,$

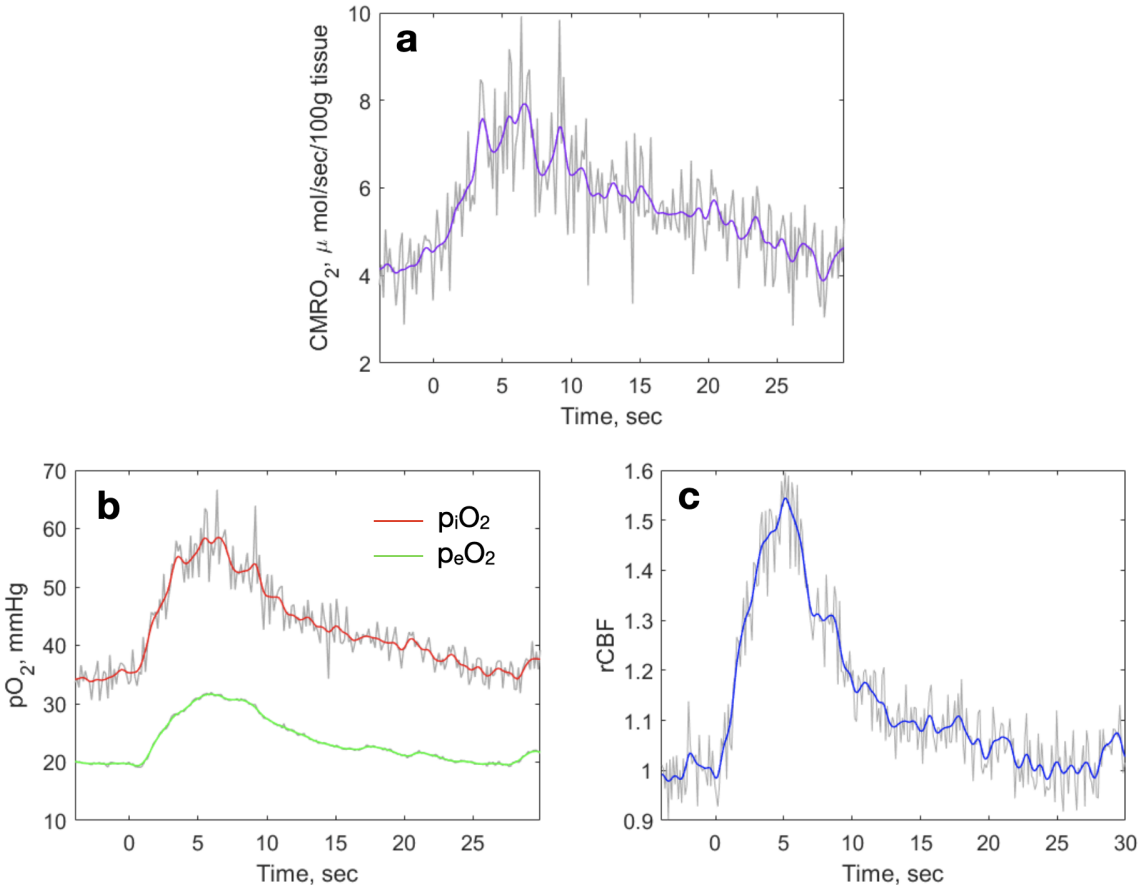

Figure 18: An example of $CMRO_2$, pO_2 and CBF response to a single functional stimulus. (a) $CMRO_2$ was computed from pO_2 data (b). (b) and (c) are single-shots of pO_2 and CBF responses respectively.

and 430 mL/sec/100g tissue). Notice that when PS_c is large, the time constant T_o gets shorter, and the traces of full- and truncated-dynamic $CMRO_2$ strongly overlap; the full-dynamic model recovers the steady-state approximation in the limit of large PS_c. However, for smaller PS_c, the full-dynamic $CMRO_2$ increasingly lags behind the truncated-dynamic trace. This lag-effect is a direct consequence of the inclusion of the time derivative (dC_e/dt). Ultimately, a novel feature of the new methodology is its ability to directly observe and measure these delays, thereby extracting information about the timing of physiologically-relevant events such as neurovascular coupling.

As noted above, choice of PS_c is important. As described above, we used prior

experimental measurement constraints on capillary diameter [122, 152, 91, 154, 57], inter-capillary distance [85, 122, 79], intravascular volume fraction [122, 152, 91, 57, 125], oxygen diffusion coefficient [19, 63, 52, 135], and baseline $CMRO_2$ [41, 134, 150, 73], along with the predictions of the Krogh-Erlang model, Eq. (2.12), to select an optimal PS_c of 210 mL/sec/100g tissue. This value of PS_c gives a baseline absolute $CMRO_2$ of $\sim$ 3.5 μmoles/sec/100g tissue and a peak activation absolute $CMRO_2$ of $\sim$ 6.0 μmoles/sec/100g tissue (Fig. 19a (middle panel)) from the averaged traces obtained in the experiment shown in Fig. 16. We will use this value of PS_c for the remainder of the analysis; it gives a measurable but small dynamic versus steady-state $CMRO_2$ delays.

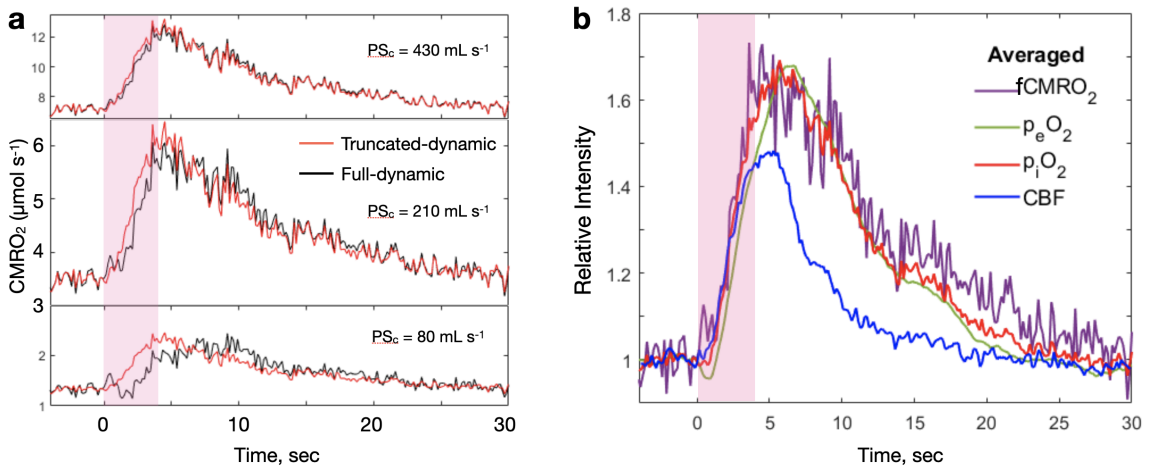

Figure 19: (a) Computed traces of full-dynamic and truncated-dynamic $CMRO_2$ (see the text for definitions) for three different values of parameter PS_c. (b) Normalized traces of CBF, p_eO_2, p_iO_2 and full-dynamic $CMRO_2$

To put the full amplitude and temporal responses of CBF, p_eO_2, p_iO_2 and $CMRO_2$ into physiological/biochemical context, we averaged the traces of CBF, p_eO_2, p_iO_2 and $CMRO_2$ (from the 13 stimulations in Fig. 16 assuming PS_c = 210 mL/sec/100g tissue). In Fig. 19b, we exhibit these averaged traces normalized by their respective pre-activation baseline values. Data in this figure illustrates how the peak responses

vary in strength for the different variables and is discussed further below.

In Fig. 20, we exhibit these same traces (Fig. 19b) but normalized by their peak amplitude. (This approach is similar to that chosen in other publications, *e.g.*, Refs. 101 and 164, for timing analyses.) Figs. 20a,c show "whole" response curves; enlargements of the responses at early times are given in Figs. 20b,d. Examination of Figs. 20b,d permits the study of relative delays in full-dynamic versus truncated-dynamic models at early times. Briefly, $CMRO_2$, CBF, and the intra- and extravascular pO_2 increase from their baseline levels when activation initiates a rapid increase in energy consumption by neurons and other cells. Mitochondrial oxidative phosphorylation is expected to respond nearly instantaneously by elevating the rate of the ATP (adenosine triphosphate) synthesis and consequently, $CMRO_2$. This rise in energy consumption is the key trigger that initiates the cascade of events for all measured parameters. Our data and analysis thus take the first steps towards the direct confrontation of the full-dynamic versus truncated-dynamic models and their underlying assumptions.

In Fig. 20, we see that the earliest event following stimulation is an initial rise in $CMRO_2$ due to local depletion of oxygen. This behavior is a manifestation of the "initial dip" in the trace of p_eO_2 and is apparent to varying degrees in both full-dynamic and truncated-dynamic models.

We first consider the early-time results of the full-dynamic model (Fig. 20b). The steep initial rise of $CMRO_2$ is a mathematical consequence of the instantaneous value of C_e and its time-derivative in the p_eO_2 dip. Subsequently, we observe a flattening of the $CMRO_2$ response for a brief period ($0.3-1.3$ sec), followed by a very steep rise. The initial rise of $CMRO_2$, at times of order 0.3 sec (or less), triggers the vascular response of upstream arterioles *via* a pathway known as neurovascular coupling [54, 65]. As a result, local CBF starts to increase and brings newly oxygenated blood

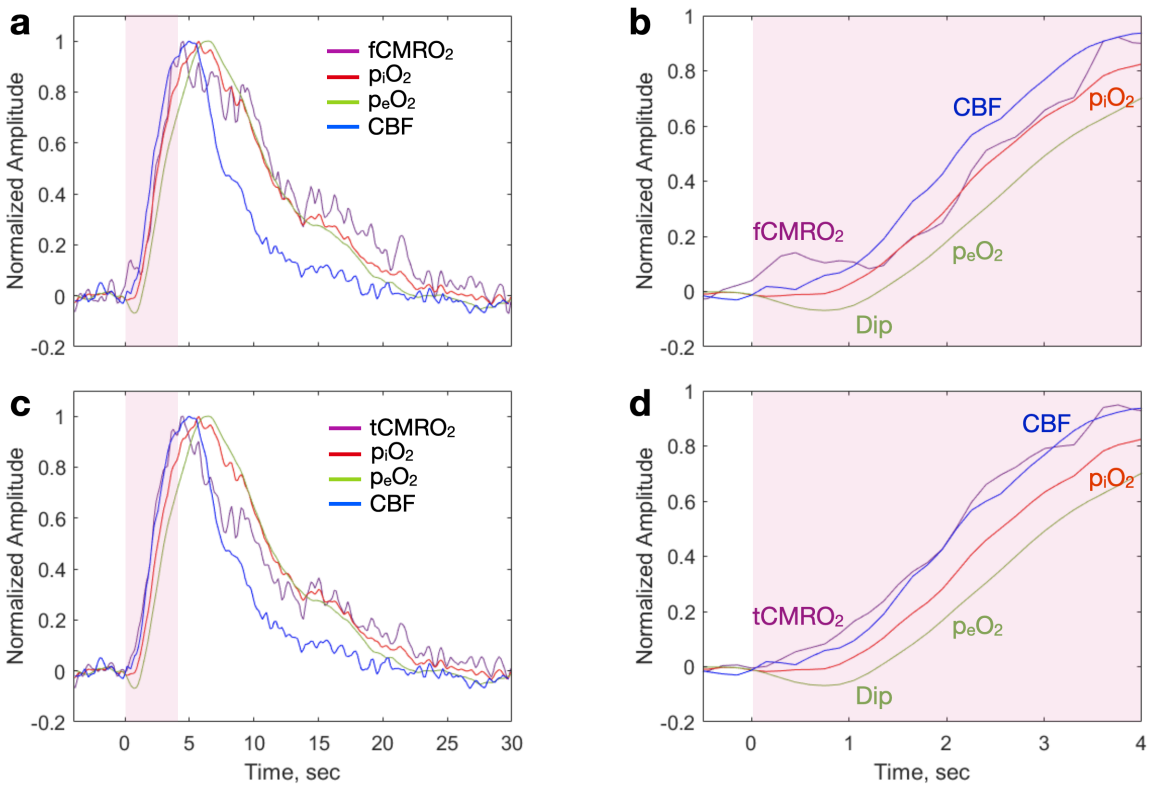

Figure 20: Normalized traces of $CMRO_2$, p_iO_2, p_eO_2 and CBF. (a,b) compares dynamic $CMRO_2$ with p_iO_2, p_eO_2 and CBF, and (c,d) compares steady-state $CMRO_2$ with p_iO_2, p_eO_2 and CBF.

into the activated region. Even with our finite temporal resolution and non-negligible noise, the measurements clearly reveal the triggering event of $CMRO_2$ in advance of the rapid increase of CBF. Once triggered, CBF grows very rapidly. When CBF reaches 20% of its peak value at ~ 1.4 sec, it leads p_iO_2, p_eO_2, and $CMRO_2$, though the rate-of-increase (slopes) of all variables is about the same within measurement error. The temporal trajectory of $CMRO_2$ over this initial time period (~ 1.5 sec) is more complex than the CBF trajectory; this $CMRO_2$ behavior is a mathematical consequence of the changing slope around the p_eO_2 dip and the compartment time constant, T_o. After the initial transients, the $CMRO_2$ and p_iO_2 (due to increased arterial blood) traces roughly overlap; they lead p_eO_2 and lag CBF slightly.

Figures 20c,d show the results of the truncated-dynamic analysis based on the

same input data. Recall that the time derivative is set to zero in Eq. (2.2) for the truncated-dynamic model. In this case, $CMRO_2$ and CBF overlap at early times. The early changes observed are at the limits of our resolution and noise but are consistent with $CMRO_2$ slightly leading CBF and triggering a rapid CBF rise. The temporal trajectory of $CMRO_2$ over the initial time period ($\sim$ 1.5 s) is similar to CBF; $CMRO_2$ and CBF traces overlap within experimental error, and they lead both p_iO_2 and p_eO_2.

We computed the important timescales for both models. A summary of these timescales, *i.e.*, $t_{trigger}(= t_{9\%}), t_{20\%}, t_{50\%}, t_{90\%}, t_{peak}$ and t_{fall} (the 50% decay-time point), is given in Table 6 for each model (full- and truncated-dynamics).

Table 6: Timing of $t_{trigger} = t_{9\%}, t_{20\%}, t_{50\%}, t_{90\%}, t_{peak}$, and t_{fall}, corresponding to the $9\%, 20\%, 50\%, 90\%$ rise during functional activation, and the peak-time and 50% fall-time, respectively. Estimates are given for CBF, pO_2 and $CMRO_2$ (both full- and truncated-dynamic models). The confidence interval for the timing was computed from standard error of the mean of the set of 13 traces (in parenthesis).

Parameters	$t_{9\%}$, sec	$t_{20\%}$, sec	$t_{50\%}$, sec	$t_{90\%}$, sec	t_{peak}, sec	t_{fall}, sec
CBF	1.0(0.2)	1.4(0.1)	2.1(0.1)	3.5(0.3)	5.0(0.4)	7.5(0.2)
p_iO_2	1.3(0.1)	1.7(0.1)	2.6(0.1)	4.4(0.1)	5.7(0.2)	11.1(0.3)
p_eO_2	-	2.1(0.1)	3.1(0.1)	5.2(0.3)	6.5(1.5)	11.1(0.4)
$fCMRO_2$	0.2 (0.2)	1.6(0.2)	2.4(0.2)	3.6(0.6)	4.5(0.2)	11.5(0.5)
$tCMRO_2$	0.8 (0.3)	1.2(0.2)	2.1(0.1)	3.5(0.2)	4.5(0.2)	10.5(0.7)

The differences between full- and truncated-dynamic models at early times are interesting to speculate about and offer new means to explore the underlying physiological assumptions of the models. Briefly, the results based on truncated-dynamic analysis (Fig. 20d) are largely consistent with traditional expectations wherein $CMRO_2$ leads CBF, albeit the metabolic trigger event is only marginally resolvable due to limited signal-to-noise. The results based on full-dynamic analysis (Fig. 20b) show a clear metabolic neurovascular trigger event, but thereafter $CMRO_2$ appears to flatten briefly, and then rises, exhibiting a slight lag with respect to CBF. While recognizing

that the finite time-resolution and measurement noise are significant, one can still argue that the observed temporal behavior for $CMRO_2$ is different from the traditional expectation, and since the full-dynamic model includes time derivatives, one might expect new features to be revealed. How can we reconcile these model-dependent $CMRO_2$ differences? One possibility is that our choice of PS_c is not correct; with a larger PS_c (*e.g.*, 430 mL/sec/100g tissue) the full-dynamic model would give an early time temporal variation similar to the truncated-dynamic model; however, in this case, the $CMRO_2$ magnitudes would also be larger, and essentially all prior estimates of PS_c are $\sim 2\times$ smaller than 430 mL/sec/100g Tissue, if not more [123]. A related possibility is derived from capillary network heterogeneity, which the models ignore. Network heterogeneity could lead to a distribution of PS_c and thus a wider range of compartment time constants, even for the same average capillary size and separation. In a different vein, one might question the assumption of uniform metabolic response in the extravascular compartment; for example, neurons consume energy, but other cells consume energy too, and their temporal dynamics need not be the same. Such an effect could give rise to a more complex temporal variation of the $CMRO_2$ response at early (and late) times. At this stage, we do not advocate particular sets of assumptions. Rather, we emphasize that evidence from our qualitatively new methodology takes the first steps toward a more critical examination of models/model-inputs.

The temporal behaviors exhibited on longer timescales do not strongly distinguish the full-dynamic versus truncated-dynamic analyses. After reaching their peaks, all four parameters gradually return to their baselines. Interestingly, while the decay time constants of $CMRO_2$, p_iO_2 and p_eO_2 are similar, the decline of CBF is steeper than the decline of everything else (see Table 6). This observation suggests that a signal for cessation of arterial dilation is issued close to when the functional stimulus is terminated and the rate of increase of $CMRO_2$ levels off or begins to fall. It appears

the system gives feedback to attenuate arterial blood supply when oxygen in the pool is sufficient to maintain $CMRO_2$ at an elevated level. In this regard, we note that $CMRO_2$ is expected to be independent of pO_2 over the entire physiological range down to very low oxygen pressures (< 1 mmHg) [17, 157, 158]. The measurements in this peak and fall-time regime continue to suggest that the vascular responses are triggered to change by variation of the energy state reflected by $CMRO_2$ [160].

Finally, we return to Fig. 19b to consider the magnitude of the various functional activation responses. We see that $CMRO_2$ at its maximum is $\sim 1.7\times$ its baseline, while the respective increase in CBF is $\sim 1.5\times$. In other experiments ($n = 3$, averaged over $4 - 5$ stimulations) the respective increases in CBF and $CMRO_2$ were reversed, *e.g.*, $\sim 1.4\times$ and $1 \sim 1.2\times$, respectively. The observation of a larger increase in $CMRO_2$ compared to CBF is somewhat unusual since many (but not all) previous studies have found that CBF response exceeds $CMRO_2$ response in magnitude [61, 35, 39, 86, 88]. It is possible that the inversion seen in our experiments was caused by some systematic measurement errors (see Section 4.4). However, we note that this inversion is not impossible, since the amount of oxygen delivered to the activation area, even upon a moderate increase of CBF, can still overwhelm the demand caused by a large increase in $CMRO_2$, due to the very high oxygen-carrying capacity of hemoglobin. Indeed, the traces of pO_2 showed characteristic "overshoots" similar in magnitude to overshoots reported previously [30]; the overshoots have been hypothesized to be a consequence of the anatomical structure of the brain, where arterioles triggered by neurovascular coupling supply oxygen to a much larger volume than the activated region [30, 160].

4.4 Limitations

Several limitations in the current implementation of the method could cause systematic measurement errors. In the future, it should be possible to ameliorate or account for these factors.

4.4.1 Light penetration

The optical frequencies (wavelengths) used for probing p_iO_2 and p_eO_2 in our experiment were different (by design) to eliminate the cross-talk between the two measurement channels. However, the effective depth of sampling by light is wavelength-dependent due to the endogenous absorption and scattering. Strong optical heterogeneity of tissue makes it difficult to evaluate the difference in the sampling depth, but estimates based on typical brain optical properties can deliver a rough prediction of the different penetration depths. Typically, this depth penetration can be estimated using the two-point Green's function that describes light propagation of excitation light to the Oxyphor and then light propagation of the phosphorescence emission to the detection surface. We employed a Monte Carlo simulation algorithm, MCXLAB [46], to simulate the two-point Green's function; this code incorporated typical brain optical properties and enabled us to deduce the comparative depth penetration of the incident excitation light and the comparative losses of escaping phosphorescent photons. Thus we could estimate the spatial origin of the measured signals due to the different Oxyphors. The optical properties for the simulation are summarized in Table 7.

As a result, the effective depth-penetration associated with the optical signals due to PtR4 and PtG4 were approximately 0.7 mm and 1.6 mm, respectively. These

Table 7: Absorption and scattering coefficients (μ_a and μ_s' respectively) for simulation. For the simulation, concentrations of HbO and HbR were set to be 60μM and 40μM respectively.

Parameters	PtR4 (Excitation/Emission)	PtG4 (Excitation/Emission)
Wavelength (nm)	517 / 670	634 / 770
μ_a (cm^{-1})	2.50 / 0.13	0.22 / 0.10
μ_s' (cm^{-1})	20 / 16	15 / 13

different effective sampling volumes of the two phosphors could be a source of systematic error, for example, if the oxygen concentrations or vascular architecture vary significantly over this range.

In the future, it should be possible to select two probes excitable at the same wavelength, but with both having minimally overlapping phosphorescence spectra, both in the near-infrared region. Using appropriate optical filtering, the signals of the probes could then be sampled independently, and the difference between the probed volumes will be minimized. A selection of dendritic oxygen probes with different optical parameters is available for exploration [80, 44, 43] and will be tested in the future. Another useful independent experiment could measure (for example, using electrode techniques) the differences in oxygen with depth over this range.

4.4.2 Temperature dependence of Oxyphor

Since the brain tissue after the craniotomy was exposed to room-temperature air, a temperature gradient from the surface down was established. Both phosphorescence decay times and oxygen quenching parameters of the probes are temperature-dependent [44]. Thus, the combination of the temperature gradient, which was unknown, with the different sampling depths for the two probes (see above) could have its own effect on the measured apparent oxygen gradients. For example, at 36.5^{o}C,

PtG4 emission will have a lifetime of 27 μs at 40 mmHg of oxygen tension, but at 33.0^{o}C a lifetime of 27 μs converts to 43.2 mmHg (see Fig. 21). Again, minimizing the difference between the sampling volumes should decrease the associated systematic error.

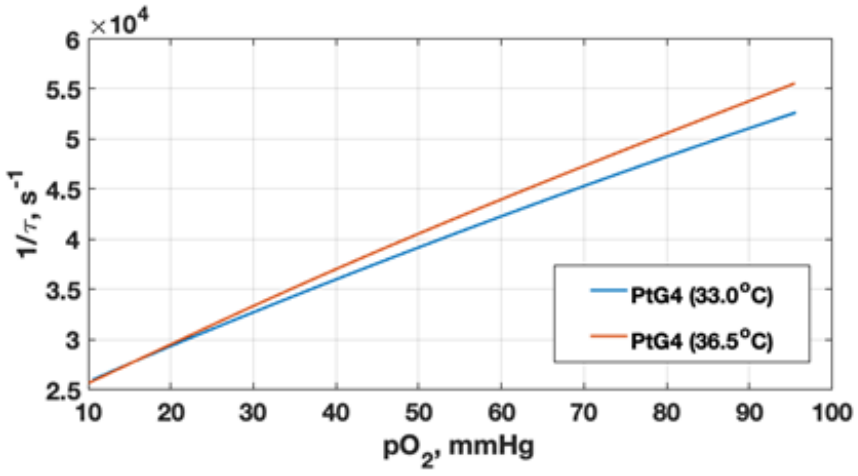

Figure 21: Temperature-dependent PtG4 calibration curve. At a given phosphorescence decay time, τ, a different pO_2 value is assigned according to the temperature.

4.4.3 Invasive injection of Oxyphor

One of the principal strengths of all-optical methodology is its minimal invasiveness. However, in our experiments one of the probes had to be delivered by direct injection into the brain tissue close to the measurement site, potentially damaging the brain. To circumvent this problem in the future it should be possible to introduce the extravascular pO_2 probe by injection into *cisterna magna* [43], far away from the measurement site and thus avoid tissue damage.

Chapter 5

Spatial Frequency Domain Fluorescence Diffuse Optical Tomography for Image-guided Tumor Resection Surgery (Background and Theory)

The background and theory development in this chapter largely adapted from a pending publication: Chong, S. H., Markel, V. A., Parthasarathy, A. B., Ong, Y. H., Abramson, K., Moscatelli, F. A., & Yodh, A. G. (2022). *Algorithms and instrumentation for rapid spatial frequency domain fluorescence diffuse optical imaging* [Manuscript submitted for publication]. Department of Physics & Astronomy, University of Pennsylvania.

5.1 Introduction

Surgical guidance based on fluorescence imaging is rapidly becoming a method of choice for resection of tumors [113, 42, 6], especially in neuro- [16, 83, 84, 105] and thoracic-surgeries [106, 107]. The primary goal of surgical resection is to excise all cancerous tissue since leftover residual tumor cells can lead to local cancer regrowth and poor clinical outcomes [100]. Currently, surgeons rely on visual inspection, palpation, or intraoperative pathology to identify tumor boundaries and residual tumor cells; however, the specificity and spatial resolution of these methods are very limited. Fluorescence imaging addresses some of these limitations by providing spatially

resolved, real-time contrast between tumorous and healthy tissues. The technique relies on exogenous contrast agents that accumulate preferentially in tumors, such as the widely-used and FDA-approved fluorophore Indocyanine Green (ICG) and some newer cell-specific fluorophores [151]. Fluorescence light emitted by these contrast agents helps demarcate boundaries between cancerous and healthy tissue.

Currently, fluorescence image guidance for surgical tumor-resection is accomplished with commercial and research-grade imaging systems [113, 104] that utilize epi-illumination with near-infrared (NIR) light, and that image fluorescence from the surgical scene with wide-field camera-based detectors. In practice, two-dimensional (2D) fluorescence images from the tissue (including the tumor regions) are overlaid on a corresponding 2D bright-field image; this method enables surgeons to ascertain the transverse coordinate of the tumor. Since preserving normal tissue is critical for organs such as brain, accurate detection of tumor margins is important beyond a rough localization. In this regard, current fluorescence imaging still suffers from technical limitations. First, 2D fluorescence imaging is most accurate only for tumors at or near the tissue surface, and it cannot determine tumor depth. Second, diffusion of the fluorescent light from the tumor can make the image margins appear larger than the actual tumor margins [62]; this effect is more pronounced for sub-surface tumors. Improved localization of the tumorous tissues in three dimensions (3D) is therefore desirable for better surgical planning and outcomes.

To improve the localization of tumors during surgery, our work adapts a parallel set of diffuse optical fluorescence imaging advances that predate the current commercial approaches for fluorescence image guidance [23, 27, 53, 33, 1, 128, 74, 78, 50, 24, 133, 26, 137, 127]. While these early advances have rarely been deployed clinically, they hold potential for wide-field, non-contact fluorescence imaging with real-time processing. One of these techniques utilizes two different wavelengths of fluorescent

emission [81] to derive information about tumor depth [161]; however, information about tumor lateral margins is not obtained by this method. The other technique, Spatial Frequency Domain Fluorescence Diffuse Optical Tomography (SFD-FDOT), was used to produce 3D images of small point-like fluorophore targets [74] *in vitro* and in mouse models. SFD-FDOT illuminates tissue with the continuous wave, wide-field intensity patterns which are sinusoidally modulated at different spatial frequencies. With this scheme, the light penetration depth is controlled by the spatial frequency, and the wide-field image data collected at different spatial frequencies facilitates the 3D reconstruction of the fluorophore concentration. In principle, the SFD-FDOT method allows one to acquire 3D information about the tumor depth and lateral margins. However, prior implementations of SFD-FDOT were limited to point-like fluorophore targets (diameter of ~ 2 mm) located less than ~ 3 mm below the surface.

Here we report on an instrument and a new rapid reconstruction algorithm for SFD-FDOT. Our analysis builds on the spatial frequency domain approach and introduces a rapid and computationally inexpensive two-step reconstruction algorithm. In the first step, we use the variation of reflected diffuse fluorescence intensity with respect to the spatial modulation frequency of incident light to estimate tumor depth. Then, using the tumor depth determined in the first step, we determine the lateral margins of the fluorophore concentration in the target plane by rapid analytical data inversion. Herein we report the principles and details of this methodology, and we exhibit the results from a series of SFD-FDOT phantom experiments; the experiments characterize the depth accuracy and lateral spatial resolution of the method. The findings reported below suggest that the methodology could be useful clinically by enabling rapid tumor localization and margin assessment. Additionally, it can be used to provide constraints for more rigorous or comprehensive fluorescence tomography.

5.2 Theory of Spatial Frequency Domain Diffuse Optical Tomography

5.2.1 Light diffusion equation in turbid media

When light propagates through an optically turbid media, such as biological tissue, it interacts with the media *via* absorption and scattering events. When the number of scattering events is large compared to the number of absorption events, then it is well-known that a light diffusion equation, Eq. (5.1), accurately describes the spatiotemporal transport of the fluence rate in tissue [11, 149]. We write this diffusion equation below.

$$\nabla \cdot [D(\mathbf{r},t)\nabla\Phi(\mathbf{r},t)] - \mu_a(\mathbf{r},t)\Phi(\mathbf{r},t) + S(\mathbf{r},t) = \frac{\partial\Phi(\mathbf{r},t)}{v\partial t}, \tag{5.1}$$

$$D(\mathbf{r},t) = \frac{1}{3[\mu_a(\mathbf{r},t) + \mu_s'(\mathbf{r},t)]}, \tag{5.2}$$

where Φ, D, S, v, μ_a and μ_s' represent the light fluence rate, light diffusion coefficient, the input light source distribution, the speed of light, and the wavelength-dependent absorption and reduced scattering coefficients of light in the medium, respectively. $\mathbf{r}$ and t represent the spatial Cartesian coordinate and time. For spatial frequency domain imaging, the source is continuous wave (CW), which makes the time-derivative of the fluence rate vanish and leads to further simplification of the diffusion equation.

$$\nabla \cdot [D(\mathbf{r})\nabla]\Phi(\mathbf{r}) - \mu_a(\mathbf{r})\Phi(\mathbf{r}) + S(\mathbf{r}) = 0. \tag{5.3}$$

Tissue is never perfectly homogeneous. Typically, $D(\mathbf{r})$ and $\mu_a(\mathbf{r})$ deviate perturbatively from their average values $\bar{D}$ and $\bar{\mu}_a$. In this case, the solution of the diffusion

equation, Eq. (5.4) can be found using perturbation theory [97].

$$\Phi(\mathbf{r}) = \int S(\mathbf{r}')G(\mathbf{r},\mathbf{r}')\mathrm{d}^3r' + \int G(\mathbf{r},\mathbf{r}')[\nabla\cdot\delta D(\mathbf{r}')\nabla - \delta\mu_a(\mathbf{r}')]\Phi(\mathbf{r}')\mathrm{d}^3r'; \qquad (5.4)$$

$$\left(\nabla^2 - \frac{\bar{\mu}_a}{\bar{D}}\right) G(\mathbf{r},\mathbf{r}') = -\frac{\delta(\mathbf{r}-\mathbf{r}')}{\bar{D}}, \qquad (5.5)$$

Here $D(\mathrm{r}) = \bar{D} + \delta D(\mathrm{r})$, $\mu_a(\mathrm{r}) = \bar{\mu}_a + \delta\mu_a(\mathrm{r})$, and the Green's function, $G(\mathbf{r},\mathbf{r}')$, satisfies the Helmholtz equation, Eq. (5.5).

The second term on the right-hand side is a convolution of the Green's function with a function that involves the fluence rate and the spatial heterogeneity of the optical properties; this equation is intrinsically nonlinear when spatial heterogeneity exists. To solve it analytically, simplifying assumptions are needed. One of the assumptions is to assume homogeneous background optical properties. The zeroth-order approximation of the solution, in this case, is usually sufficient to describe light propagation in turbid media such as tissue (for NIR light).

For fluorescence imaging, two light sources and propagating diffusive light fields are involved. The first pertains to light that excites the fluorophore. The second pertains to fluorescence light emitted by the fluorophores (after they absorb the excitation light). To distinguish the two, we use a subscript *ex* for any variables/parameters relevant to the excitation light wavelength, and we use a subscript *em* for the emission light wavelength. Therefore, two governing light diffusion equations, Eqs. (5.4) and (5.5) are needed to fully describe the process by which fluorescence light emanates from a turbid media.

$$\nabla\cdot[D_{ex}(\mathbf{r})\nabla\Phi_{ex}(\mathbf{r})] - \mu_{a,ex}(\mathbf{r})\Phi_{ex}(\mathbf{r}) + S(\mathbf{r}) = 0; \qquad (5.6)$$

$$\nabla \cdot [D_{em}(\mathbf{r})\nabla\Phi_{em}(\mathbf{r})] - \mu_{a,em}(\mathbf{r})\Phi_{em}(\mathbf{r}) + \varepsilon\eta C(\mathbf{r})\Phi_{ex}(\mathbf{r}) = 0. \tag{5.7}$$

Here ε, η, and C represent the extinction coefficient, quantum efficiency and concentration of the fluorophore at $\mathbf{r}$. For both Eqs. (5.6) and (5.7), solutions can be written in a similar form in Eq. (5.4). Each solution is nonlinear *per se*, and solving them analytically is extremely difficult (or impossible).

As noted above, a few assumptions can simplify the problem. We assume that (1) then spatial heterogeneity of the background optical properties is negligible, and we assume that (2) the excitation light fluence rate in the medium is not affected by light absorption of the fluorscent contrast agents (the fluorophores). These approximations are not too bad, especially if the contrast agent concentration is low (as it usually is in practice). With these two assumptions, we can use the lowest-order approximations for the propagating excitation and fluorescence light fluence rates, which are:

$$\Phi_{ex}(\mathbf{r}) = \int_V G_{ex}(\mathbf{r}, \mathbf{r}')S(\mathbf{r}')\mathrm{d}^3r'; \tag{5.8}$$

$$\Phi_{em}(\mathbf{r}) = \int_V G_{em}(\mathbf{r}, \mathbf{r}')\varepsilon\eta C(\mathbf{r}')\Phi_{ex}(\mathbf{r}')\mathrm{d}^3r'. \tag{5.9}$$

Here the Greens functions, G_{ex} and G_{em}, satisfy Eq. (5.5) for $\bar{D}$ and $\bar{\mu}_a$ for excitation light and emission light wavelengths respectively. In essence, the perturbation in this problem derives from the heterogeneous contrast agent spatial distribution.

5.2.2 Source types

To evaluate Eqs. (5.8) and (5.9), the source term, $S(\mathbf{r})$ needs modeling. There are four standard types of sources; (1) Continuous-wave (CW, the light intensity does not vary over time), (2) Frequency-domain (FD, the light intensity is modulated in time), (3) Time-resolved (TR, the input light is a pulse whose width is typically

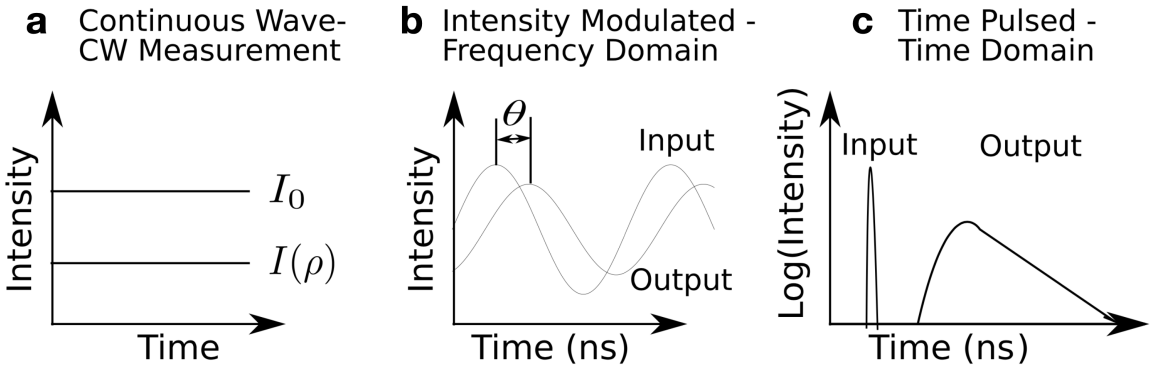

Figure 22: Schemes of light sources. (a) CW, (b) FD, and (c) TR light source. The figure is reprinted from Ref. 36

.

a few picosecond scales. The output light is broadened in time), and (4) Spatial-frequency-domain (SFD). For (1), (2), and (3), the light source is often (but not always) provided as a point source in space, either *via* fiber optics or by a focused laser-scanning system.

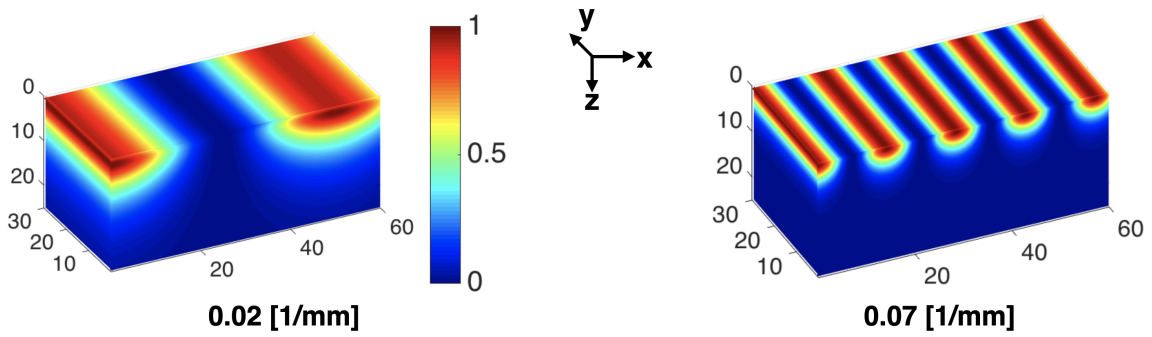

Figure 23: Two examples of spatially modulated light patterns. (left) An example of lower spatial frequency ($f = 0.02$ mm^{-1}) light pattern. (right) An example of higher spatial frequency ($f = 0.07$ mm^{-1}) light pattern.

The last type is particularly relevant for our work. The SFD light source uses wide-field epi-illumination on a sample. The light intensity is spatially modulated (but is CW in time, similar to (1) above); typically it is sinusoidally modulated in space. Each sinusoidal pattern is associated with a spatial frequency. The light penetration depends on the assigned spatial frequency (see Fig. 23); penetration is shallower for

larger spatial frequencies. We model the source as the sinusoidal function varying in space (and localized at the surface z=0).

$$S(\mathbf{r}) = S_o[1 + A\cos(\mathbf{k} \cdot \mathbf{r})]\delta(z). \tag{5.10}$$

Alternatively, removing the constant background, and switching to complex notation, the source can be written:

$$S(\mathbf{r}) = S_o e^{i\mathbf{k}\cdot\mathbf{r}}\delta(z), \tag{5.11}$$

where $\mathbf{k} = (k_x, k_y)$ is the wavevector of the spatial pattern.

5.2.3 Green's function solutions in 2D Fourier space

Our analysis will use functions that vary in the transverse plane, *i.e.*, in the x- and y-directions. As such, we need to define forward and inverse Fourier transforms in the transverse plane. These definitions are given below for functions $f(\mathbf{q})$ and $F(\boldsymbol{\rho})$; we adopt the upper case variable (F) for the real-space functions and the lower case variable (f) for the Fourier-space functions.

$$f(\mathbf{q}) = \int_{S_q} F(\boldsymbol{\rho}) e^{-i\mathbf{q}\cdot\boldsymbol{\rho}} \mathrm{d}^2\rho; \tag{5.12}$$

$$F(\boldsymbol{\rho}) = \left(\frac{1}{2\pi}\right)^2 \int_{S_\rho} f(\mathbf{q}) e^{i\mathbf{q}\cdot\boldsymbol{\rho}} \mathrm{d}^2 q, \tag{5.13}$$

Here $\boldsymbol{\rho}$ is the cartesian coordinate of a transverse plane, *i.e.*, x and y, and $\boldsymbol{q}$ is the corresponding Fourier variable.

Then, the Green's function and Helmholtz equation in Eq. (5.5) can be rewritten according to the definition of the inverse Fourier transform and the *Weyl* expan-

sion [153, 90].

$$\left(\nabla^2 - \frac{\bar{\mu}_a}{\bar{D}}\right) \int_{S_q} g(\mathbf{q}; z, z') e^{i\mathbf{q}\cdot(\boldsymbol{\rho}-\boldsymbol{\rho}')} \mathrm{d}^2 q = -\frac{\delta(z-z')}{\bar{D}} \int_{S_q} e^{i\mathbf{q}\cdot(\boldsymbol{\rho}-\boldsymbol{\rho}')} \mathrm{d}^2 q, \tag{5.14}$$

where the constant terms of $\frac{1}{2\pi}$ were canceled on both sides. Note, it is 2D inverse Fourier transform that pertains to transverse directions so that only the transverse coordinate of the Dirac delta function in the RHS of Eq.(5.5) is written in terms of the inverse Fourier transform. Then, it is straightforward to show that Eq. (5.14) can be simplified to Eq. (5.15).

$$\int_{S_q} \left[\left\{ \frac{\partial^2}{\partial z^2} - (\mu_{eff})^2 - q^2 \right\} g(\mathbf{q}; z, z') + \frac{\delta(z-z')}{\bar{D}} \right] e^{i\mathbf{q}\cdot(\boldsymbol{\rho}-\boldsymbol{\rho}')} \mathrm{d}^2 q = 0, \tag{5.15}$$

where $(\mu_{eff})^2 = 3\mu_a(\mu_a + \mu_s')$. The integrand has to be zero for all $\boldsymbol{\rho}$, which provides us with a differential equation of Green's function for planar impulse at z'.

$$\left[\frac{\partial^2}{\partial z^2} - \left\{ Q(\mathbf{q}) \right\}^2 \right] g(\mathbf{q}; z, z') = -\frac{\delta(z-z')}{\bar{D}}. \tag{5.16}$$

Here, $Q(\mathbf{q}) = \sqrt{3\mu_a(\mu_a + \mu_s') + |\mathbf{q}|^2}$.

Infinite medium. For our work, we seek the Green's function solution to Eq. (5.16), wherein the input(*i.e.*, the source) is confined to a plane (z') and is permitted to have sinusoidal spatial variation with wavevector $\mathbf{q}$ (in the plane transverse to the z-direction). For the infinite medium, the only boundary condition is that $g(\mathbf{q}; z, z') \to 0$ as $|z - z'| \to \infty$. In this case,

$$g(\mathbf{q}; z, z') = \frac{e^{-Q(\mathbf{q})|z-z'|}}{2\bar{D}Q(\mathbf{q})}, \tag{5.17}$$

Here, $Q(\mathbf{q}) = \sqrt{3\mu_a(\mu_a + \mu_s') + |\mathbf{q}|^2}$. Note, the Green's function solution is isotropic

in transverse plane in the real space. The Fourier transformed Green's function is also symmetric in $\mathbf{q}$.

Semi-infinite medium. In realistic semi-infinite medium cases, there is a boundary between the turbid media and air. Diffuse light escapes from the media to the air. This is the light we detect in our experiments. When it escapes, it does not return. Therefore, other than the light source, the only radiance traveling into the turbid medium is derived from the reflected "escaping" radiance predicted due to Fresnel reflections. This effect provides a boundary condition for the semi-infinite medium problem, the so-called partial flux boundary condition [5].

$$(G + \ell\hat{\mathbf{n}} \cdot \nabla G)\,|_S = 0, \tag{5.18}$$

where ℓ is called the extrapolation distance [5] (which is of order but is slightly different from $1/\mu_s'$), and S is the boundary surface. When the flux is normal to the surface, Eq. (5.18) reduces to Eq. (5.19) (again using Fourier transforms).

$$\left(g + \ell\frac{\partial g}{\partial z}\right)\Bigg|_{z=0} = 0. \tag{5.19}$$

The boundary conditions for the semi-infinite medium follow [98]

$$\begin{aligned}
&g(\mathbf{q}; 0, z') - \ell\frac{\partial g}{\partial z}(\mathbf{q}; 0, z') = 0,\\
&g(\mathbf{q}; z' + \epsilon, z') - g(\mathbf{q}; z' - \epsilon, z') = 0,\\
&\frac{\partial g}{\partial z}(\mathbf{q}; z' + \epsilon, z') - \frac{\partial g}{\partial z}(\mathbf{q}; z' - \epsilon, z') = -\frac{1}{\bar{D}},\\
&g(\mathbf{q}; z, z') < \infty,\ as\ z \to \infty.
\end{aligned} \tag{5.20}$$

Solving for the semi-infinite medium Green's function is straightforward. We obtain

the solution, Eq. (5.21). Note, as was the case for the infinite-medium solution, the semi-infinite medium solution is also symmetric in $\mathbf{q}$.

$$g(\mathbf{q}; z, z') = \frac{1}{2\bar{D}Q(\mathbf{q})}\left[e^{-Q(\mathbf{q})|z-z'|} + \frac{1-\ell Q(\mathbf{q})}{1+\ell Q(\mathbf{q})}e^{-Q(\mathbf{q})(z+z')}\right]. \tag{5.21}$$

5.2.4 Fast analytic inversion algorithms for spatial frequency domain light source

In the previous section, an expression for the SFD light source, $S(\mathbf{r})$ was given. Using the expression, Eq. (5.8), the homogeneous excitation fluence rate can be written in a simple analytical form.

$$\begin{aligned}\Phi_{ex}(\boldsymbol{\rho}, z; \mathbf{k}) &= S_o \int G_{ex}(\boldsymbol{\rho}, \boldsymbol{\rho}', z, z') e^{i\mathbf{k}\cdot\boldsymbol{\rho}'} \delta(z) \mathrm{d}^3 r' \\ &= S_o g_{ex}(\mathbf{k}, z, 0) e^{i\mathbf{k}\cdot\boldsymbol{\rho}}.\end{aligned} \tag{5.22}$$

g_{ex} depends on sample geometry (*e.g.*, semi-infinite, etc.).

The emission fluence rate, Φ_{em} is also readily written. Plugging Eq. (5.22) into Eq. (5.9) gives:

$$\Phi_{em}(\mathbf{r}_d; \mathbf{k}) = \varepsilon\eta \int_V G_{em}(\mathbf{r}_d, \mathbf{r}) C(\mathbf{r}) \Phi_{ex}(\mathbf{r}; \mathbf{k}) \mathrm{d}^3 r. \tag{5.23}$$

$\mathbf{r}_d$ is the cartesian coordinate of the sample surface and equivalent to (x_d, y_d, z_d). Note, typically, in our semi-infinite space we set $z_d = 0$.

2D Fourier transform of Eq. (5.23) renders a useful form that converts the 3D integration to a one-dimensional integration, Eq. (5.24), that in some cases can be

easily inverted.

$$\varphi_{em}(\mathbf{q}_d, z_d = 0; \mathbf{k}) = \varepsilon\eta \int g_{em}(\mathbf{q}_d, z_d = 0, z) g_{ex}(\mathbf{k}, z, 0) c(\mathbf{q}_d - \mathbf{k}, z) \mathrm{d}z, \tag{5.24}$$

where φ_{em} and c are 2D Fourier Transform of Φ_{em} and C respectively. $\mathbf{q}_d$ is the Fourier variable corresponding to $\boldsymbol{\rho}_d = (x_d, y_d)$. By substituting $\mathbf{q}$ for $\mathbf{q}_d - \mathbf{k}$, a final convolution integral equation is acquired.

$$\varphi_{em}(\mathbf{q} + \mathbf{k}, z_d = 0; \mathbf{k}) = \varepsilon\eta \int \gamma(\mathbf{q}, z_d = 0, z; \mathbf{k}) c(\mathbf{q}, z) \mathrm{d}z; \tag{5.25}$$

$$\gamma(\mathbf{q}, z_d = 0, z; \mathbf{k}) = \left(\frac{\ell_{ex}\ell_{em}}{\bar{D}_{ex}\bar{D}_{em}} \right) \frac{e^{-[Q_{ex}(\mathbf{k}) + Q_{em}(\mathbf{q}+\mathbf{k})]z}}{[1 + \ell_{ex}Q_{ex}(\mathbf{k})][1 + \ell_{em}Q_{em}(\mathbf{q} + \mathbf{k})]}. \tag{5.26}$$

Later, we will use these results to analyze the distribution of exogenous fluorophore targets in our tissue phantom experiment. For now, we will next describe how the experiments are done.

5.2.5 Data acquisition and analysis

In practice, the sample surface is illuminated by a sinusoidally modulated intensity pattern of the form as described above. In the experiment, we add three different phases to Eq. (5.10) to realize the complex light source, Eq. (5.11).

$$S_i(\boldsymbol{\rho}_d; \boldsymbol{k}) = \frac{S_o}{2}[1 + \cos(\boldsymbol{k} \cdot \boldsymbol{\rho}_d + \theta_i)] \ , \quad i = 1, 2, 3 \ . \tag{5.27}$$

Here $\boldsymbol{\rho}_d = (x_d, y_d)$, where x_d and y_d are Cartesian coordinates in the surface of the sample (assumed to be a plane). The quantities S_o and θ_i represent the incident intensity and the spatial phase shift of the illumination pattern. In the experimental procedure, we use $\theta_1 = 0$, $\theta_2 = 2\pi/3$ and $\theta_3 = 4\pi/3$ (this choice of phases will

be explained below). In principle, it is possible to use general 2D modulation wave vectors $\boldsymbol{k}$. However, in our experiments, we modulated the incident light only along the x-axis, so that $\boldsymbol{k} = (k, 0)$, where the spatial modulation wave number is $k = 2\pi f$, and f is the spatial frequency of the modulating sinusoid. This restriction of the modulation wave vector is sufficient for reconstructions. The use of other modulation directions can enhance the method but requires larger data acquisition times.

In the experiments, we typically employed 31 different spatial frequencies f varying from 0 to 0.15 mm^{-1}. Note that, in practice, small discrepancies arise between the set of intended and actual values of f on the phantom surface due to small deviations in the estimated distance between the sample surface and the collection lens. We determine the actual values of f by analyzing the bright-field image, and we use these measured values of f in the reconstructions.

For each illumination pattern $S_i(\boldsymbol{\rho}_d; \boldsymbol{k})$, a corresponding fluorescent (intensity) emission image $I_i(\boldsymbol{\rho}_d; \boldsymbol{k})$ was recorded. The images I_0, I_1 and I_2 were then combined to obtain the complex fluorescent emission signal, $\Phi_{em}(\boldsymbol{\rho}_d; \boldsymbol{k})$ according to

$$\begin{aligned} \Phi_{em}(\boldsymbol{\rho}_d; \boldsymbol{k}) \quad &= \tfrac{1}{3}\left[2I_0(\boldsymbol{\rho}_d; \boldsymbol{k}) - I_1(\boldsymbol{\rho}_d; \boldsymbol{k}) - I_2(\boldsymbol{\rho}_d; \boldsymbol{k})\right] \\ &\quad + \tfrac{i}{\sqrt{3}}\left[I_2(\boldsymbol{\rho}_d; \boldsymbol{k}) - I_1(\boldsymbol{\rho}_d; \boldsymbol{k})\right] \ . \end{aligned} \tag{5.28}$$

This combination is well known and is needed for our analysis. Essentially, it allows us to remove the constant background in illumination and to access information about amplitude and phase (equivalent to that provided by illuminating the medium with both sine and cosine functions in the spatial modulation pattern). The resultant emission data, Φ_{em}, is Fourier transformed to estimate the depth of the fluorescent inclusion.

Estimation of target depth. The first step in the reconstruction algorithm is

to estimate the target depth. To this end, we utilize a simplification of Eq. (5.25). Specifically, we assume that the fluorophores are localized at a particular depth, which we refer to as z_{target}, so that $c(\boldsymbol{q}, z) = \hat{C}(\boldsymbol{q})\ \delta(z - z_{\text{target}})$. In this case, Eq. (5.25) simplifies to the following form:

$$\varphi(\boldsymbol{q} + \boldsymbol{k}; \boldsymbol{k}) = \varepsilon\eta\gamma(\boldsymbol{q} + \boldsymbol{k}, z_{\text{target}}; \boldsymbol{k})\ c(\boldsymbol{q})\ . \tag{5.29}$$

This equation can be rearranged to relate the z-dependent kernel to the measured fluorescence emission and to the fluorophore concentration distribution. Note that, even if the actual fluorophore distribution is more widely spread in the z-direction, our method will derive a fairly good estimate of the depth. Specifically, with the assumptions outlined above, and with $\boldsymbol{q} = 0$, it is straightforward to show that, for each spatial modulation wave vector $\boldsymbol{k}$, we have

$$y(\boldsymbol{k}) = A\ \exp(-z_{\text{target}}\ x(\boldsymbol{k})) + y_o\ , \tag{5.30a}$$

where

$$x(\boldsymbol{k}) = Q_{\text{ex}}(\boldsymbol{k}) + Q_{\text{em}}(\boldsymbol{k})\ ; \tag{5.30b}$$

$$y(\boldsymbol{k}) = \varphi(\boldsymbol{k}; \boldsymbol{k})[Q_{\text{ex}}(\boldsymbol{k})\ell_{\text{ex}} + 1][Q_{\text{em}}(\boldsymbol{k})\ell_{\text{em}} + 1]\ . \tag{5.30c}$$

The dependent variable, $y(\boldsymbol{k})$, is the normalized emission response at the modulation wave vector $\boldsymbol{k}$. The independent variable, $x(\boldsymbol{k})$, can be measured or estimated; it is, essentially, twice the reciprocal of the penetration depth, which depends on the spatial modulation frequency. The parameter $A = \varepsilon\eta\left(\frac{\ell_{\text{ex}}\ell_{\text{em}}}{D_{\text{ex}}D_{\text{em}}}\right)c(0)$ depends on a number of parameters of the background medium and the fluorophores, some of which may not be directly known or measured, but it is independent of the modulation wave

vector $\boldsymbol{k}$. In a data set obtained by varying $\boldsymbol{k}$, we can view A as a constant and as an adjustable parameter. Further, y_o is an extra adjustable parameter added to account for the noise floor in the data since the fluorescent signal does not go to zero when $|\boldsymbol{k}| \to \infty$ (as predicted theoretically), perhaps as a result of background fluorescence and other noise, as well as imprecision in the theoretical model. As A, we assume that y_o is independent of $\boldsymbol{k}$.

We can now find z_{target} by nonlinear fitting of the theoretical formula, Eq. (5.30a), to the data in which A, z_{target} and y_o are viewed as $\boldsymbol{k}$-independent adjustable parameters. Once the depth of the target is determined, we can compute the lateral margins of the fluorophore concentration in the plane.

Estimation of lateral margins of target. This is the second step in our two-step algorithm. Briefly, rearranging Eq. (5.29) for $c(\boldsymbol{q})$ and taking the inverse 2D Fourier transform, we obtain a simple reconstruction formula for the transverse distribution of the fluorophore target in the plane $z = z_{\text{target}}$. The obtained relation is parameterized by $\boldsymbol{k}$ and, theoretically, any value of $\boldsymbol{k}$ can be used to obtain the transverse distribution of the fluorophore. In the reconstructions, we have used the $\boldsymbol{k} = 0$ for this purpose because the signal-to-noise ratio in the fluorescence images is best for unmodulated incident light. Therefore, we use the reconstruction formula

$$C(\boldsymbol{\rho}, z = z_{\text{target}}) = \frac{1}{\varepsilon\eta} \int \frac{\hat{\Phi}(\boldsymbol{q}; \boldsymbol{k} = 0)}{\gamma(\boldsymbol{q}, z_{\text{target}}; \boldsymbol{k} = 0)} e^{-i\boldsymbol{q}\cdot\boldsymbol{\rho}} f_\sigma(\boldsymbol{q}) \frac{\mathrm{d}^2 q}{(2\pi)^2} \ , \tag{5.31}$$

where

$$f_\sigma(\boldsymbol{q}) = \frac{1}{2\pi\sigma^2} \exp\left(-\frac{q^2}{2\sigma^2}\right) \tag{5.32}$$

is a Gaussian low-pass filtering kernel.

We apply $f_\sigma(\boldsymbol{q})$ to ameliorate the effects of noise and model imprecisions that render the integrand in Eq. (5.31) unreliable at high values of q. Since the denominator

of the integrand decreases exponentially with q (see Eq. (5.26)), the contribution of noise to the image is amplified when large values of q are used in a numerical reconstruction. The Gaussian filter enables us to regularize Eq. (5.31). The regularization parameter σ depends on the level of noise and must be determined for each data set separately. However, the reconstruction is so fast that it is possible to generate many images in real-time while tuning σ.

5.2.6 Nonlinear fitting

Prior to fitting, the data were normalized to the maximum value. That is, both sides of Eq. (5.30a) were divided by $y(\boldsymbol{k} = 0)$. This allowed us to compare errors of the fit for different data sets quantitatively. We then obtained an estimate of the fluorophore target depth, z_{target}, from the best fit of the theoretical formula, Eq. (5.30a), to the data points $(x(\boldsymbol{k}), y(\boldsymbol{k})/y(0))$. We removed the first data point (with the smallest $|\boldsymbol{k}|$) from the fitting procedure (it will be discussed in the next chapter). For the fitting, we used a nonlinear regression model algorithm, `fitnlm` (MATLAB 2022a, The Mathworks Inc., Natick, Massachusetts, USA), and chose the initial values for A, z_{target}, and y_o to be 5.0, 1.0, and 0.1, respectively.

Chapter 6

Spatial Frequency Domain Fluorescence Diffuse Optical Tomography for Image-guided Tumor Resection Surgery (Experiment, Results and Discussion)

This chapter largely adapted from a pending publication: Chong, S. H., Markel, V. A., Parthasarathy, A. B., Ong, Y. H., Abramson, K., Moscatelli, F. A., & Yodh, A. G. (2022). *Algorithms and instrumentation for rapid spatial frequency domain fluorescence diffuse optical imaging* [Manuscript submitted for publication]. Department of Physics & Astronomy, University of Pennsylvania.

6.1 Experimental Results

6.1.1 Imaging instrumentation

For testing and for eventual clinical implementation, we constructed a wide-field imaging system that consisted of a digital micro-mirror device for illuminating the tissue at different spatial frequencies, and a spectrally-separated dual camera detection system that simultaneously records bright-field reflectance images at the excitation wavelength of 808 nm and fluorescence images at the emission wavelength of 850 nm. The setup is illustrated schematically in Fig. 24. The combined illumination and imaging system was mounted on a translation stage (MN10-015-E01-13, Velmex Inc.,

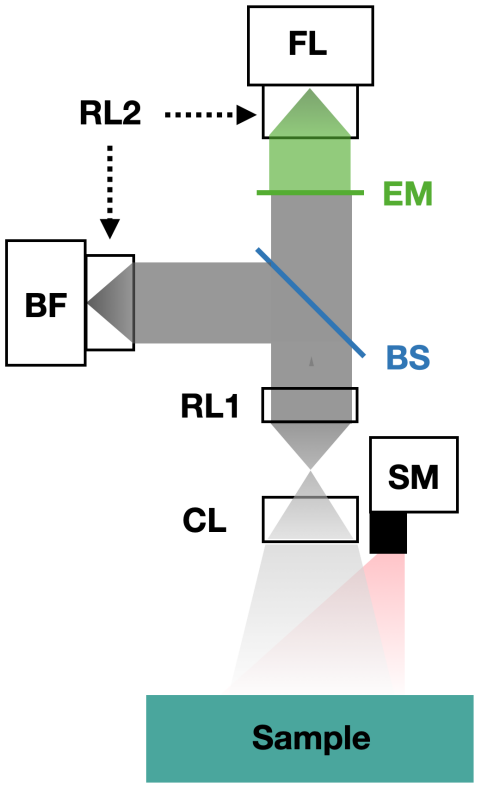

Figure 24: Schematics of the dual-camera imaging system. **SM**: Spatial modulator of the excitation light, **CL**: Collection lens, **RL**: Relay lens, **BS**: 10:90 Beam-splitter, **BF**: Bright-field camera, **EM**: Emission filter, **FL**: Fluorescence camera.

Bloomfield NY, USA) and positioned above the sample with the object distance of 32 cm. Illumination was provided by a digital light projector (FC E4500 MKII, EKB Technologies Ltd. Bat-Yam Israel). Its intensity on the sample surface was approximately 0.3 mW/cm^2 for uniform (spatially unmodulated) illumination, well below the ANSI limit for tissue damage. A digital micro-mirror device was electronically controlled to produce spatially-modulated (at different frequencies) illumination of the sample surface with wide-field light at 808 nm. Reflected light at the excitation and fluorescent wavelengths was directed to two separate camera channels; further spectral filtering was necessary to record the fluorescence image. The fluorescence emission images recorded in the fluorescence camera are used for the reconstruction

of the depth and the transverse margin of the fluorescent targets.

6.1.2 Experimental procedure

Background tissue was mimicked using a mixture of intralipid (Intralipid 20%, Fresenius Kabi, Pune, Maharashtra, India), nigrosin (Acid Black, MP Biomedicals, Santa Ana, CA, USA), and water. The background medium had a wavelength-dependent absorption coefficient, μ_a, and reduced scattering coefficient, μ_s'. Respectively, these coefficients were 0.004 mm^{-1} and 0.8 mm^{-1} at the excitation wavelength of 808 nm, and 0.006 mm^{-1} and 0.76 mm^{-1} at the emission wavelength of 850 nm. The hollow cube (for containing the fluorescent target) was 3D-printed with inner side length of 10 mm and wall thickness of 1 mm (VeroWhitePlus, Stratasys Direct Manufacturing, Valencia, CA, USA), which was suspended in a tissue-simulating liquid phantom using two posts (blue). This cube was employed to simulate the fluorescent target(s); the cube was filled with a mixture of intralipid containing dissolved ICG powder (IC-GREEN, Akorn Inc., Lake Forest IL, USA). The ICG concentration was 6.5 μM.

The fluorescent contrast cubes were suspended in the liquid phantom tank using fishing lines and posts, as shown in Fig. 25. The depths of the targets were controlled by lowering or raising the surface of the background liquid phantom in the single target experiments (see Fig. 25a).

Both bright-field and fluorescence images were recorded with a 12-bit dynamic range for each phase offset (see Fig. 26); the exposure time was increased until the maximum count of a pixel reached approximately 4000 for unmodulated incident light. The adjustable fluorescence camera exposure time ranged from 800 msec for the 2 mm depth of the target to 5 sec for the 10 mm depth; these adjustments were

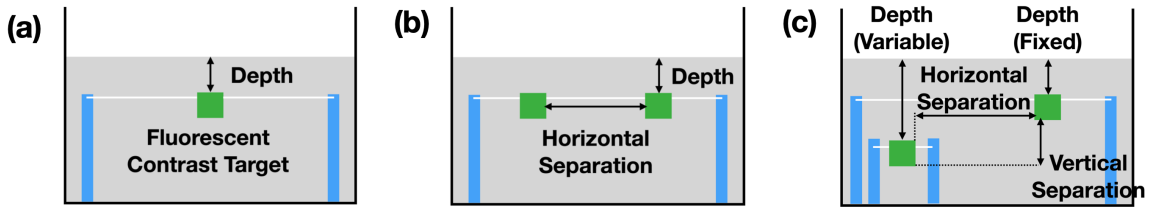

Figure 25: Schemes employed for tissue phantom experiments. (a) The single-target experiments. (b) The two-target (on the same depth) experiment. (c) The two-target (on different depths) experiment.

needed to account for the difference in detected intensity. The exposure time of the bright-field camera was about 15 msec. Accordingly, the full acquisition time for the deepest target was four times longer than that of the shallowest target. Fluorescence emission data for single-target phantoms were acquired for target depths of 2, 4, 6, 8, and 10 mm.

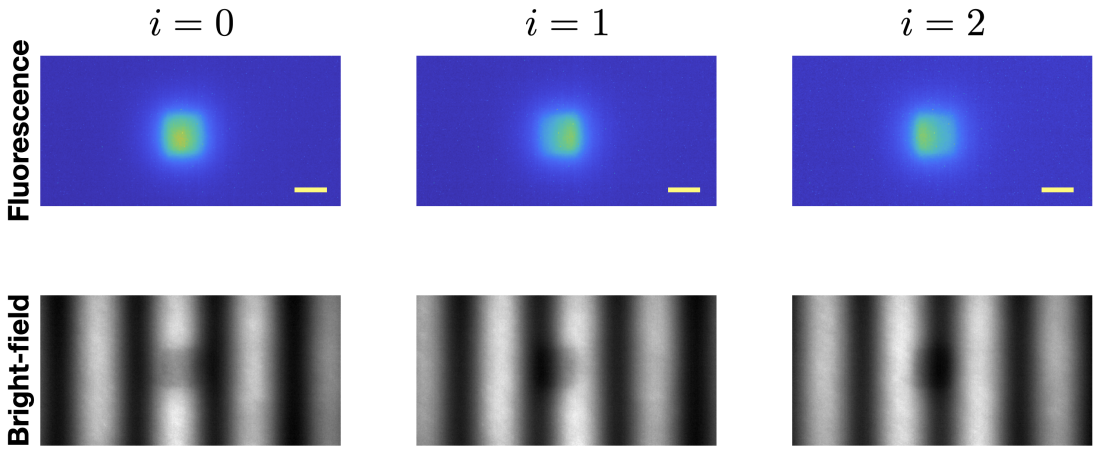

Figure 26: Example of the measurements in case of single target located at the depth of 2 mm ($f = 0.04$ mm^{-1}). Scale bar indicates 10 mm.

For two-target phantoms, two different sets of experiments were performed. In one set, two identical targets were placed at the same depth. This depth of the two targets, and the lateral separation between the targets, were varied as shown in Fig. 25b. In the second set of two-target phantom experiments, the two targets were laterally separated by either 20 or 40 mm. The depth of one target was fixed at 2

mm, while the depths of the other targets varied from 4 to 8 mm (Fig. 25c).

In all experiments, the data acquisition time for the fluorescence associated with the shallowest target (2 mm depth) was $\sim$ 2 min. The acquisition time for fluorescence associated with the deepest target (10 mm depth) was $\sim$ 8 min.

6.1.3 Single-target experimental results

The depth of the fluorescence contrast target varied from 2 to 10 mm, and the corresponding exponential fitting results are displayed in the left column of Fig. 27. The estimated depth is marked on top of the plot along with its standard deviation.

Note, the first data point corresponding to k = 0 was not used for fittings. If used, this data point can skew the decay constant to larger values and increase the fitting errors significantly. Physically, we can justify the removal of this point by recalling that the specific intensity of the light transmitted through the top interface (tissue surface) consists of two components, sometimes referred to as diffuse and ballistic (reduced). The ballistic photons have a relatively large energy flux near the interface but then undergo a much faster exponential decay with depth compared to the diffuse photons [138]. The rate of decay of both components increases as k is increased, which results in a complex competition of the two terms. For relatively shallow targets (*i.e.*, depths of 2 mm to 6 mm), the ballistic term can strongly perturb the k = 0 measurement and, perhaps, influence the next data point as well, but it becomes negligible at larger values of k. As the target moves deeper, the influence of the ballistic term is further diminished for all values of k. At the depths greater than 10 mm, the ballistic term can be generally neglected. In our experiments, however, most of the targets do not satisfy this condition; the data are affected by the ballistic term, but the theory on which the reconstructions are based accounts only for the

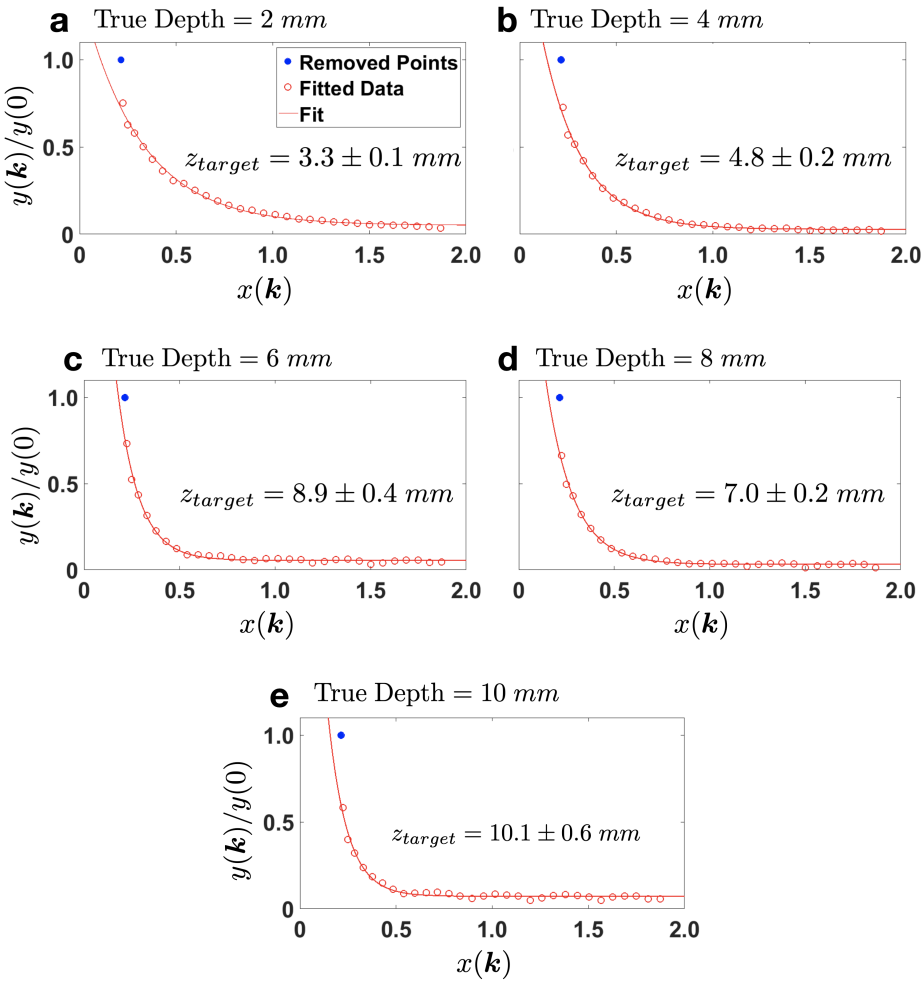

Figure 27: Single target experiment depth estimaion results . The target depth is 2 mm (a), 4 mm (b), 6 mm (c), 8 mm (d), and 10 mm (e).

diffuse photons which obey the single-exponent decay model, Eq. (5.30a). For these reasons, the data point with $k = 0$ was excluded from the fitting procedure in all reconstructions. In the future, a more systematic accounting of the ballistic photons will require the use of a two-exponent decay model [138]; if successful, inclusion of the $k = 0$ (and other data points with relatively small values of k) will be possible and should increase the dynamic range of measurements, which is useful for more accurate depth estimation.

After the target depth and its uncertainty are estimated, we determine the trans-

verse margins of the fluorophore concentration by using Eq. (5.31). The result is shown in Fig. 28. In each panel, the figure on the left shows the reconstructed transverse images, and the yellow scale bar corresponds to 10 mm. The figure on the right shows the transverse margin (blue) in comparison to the true margin (black).

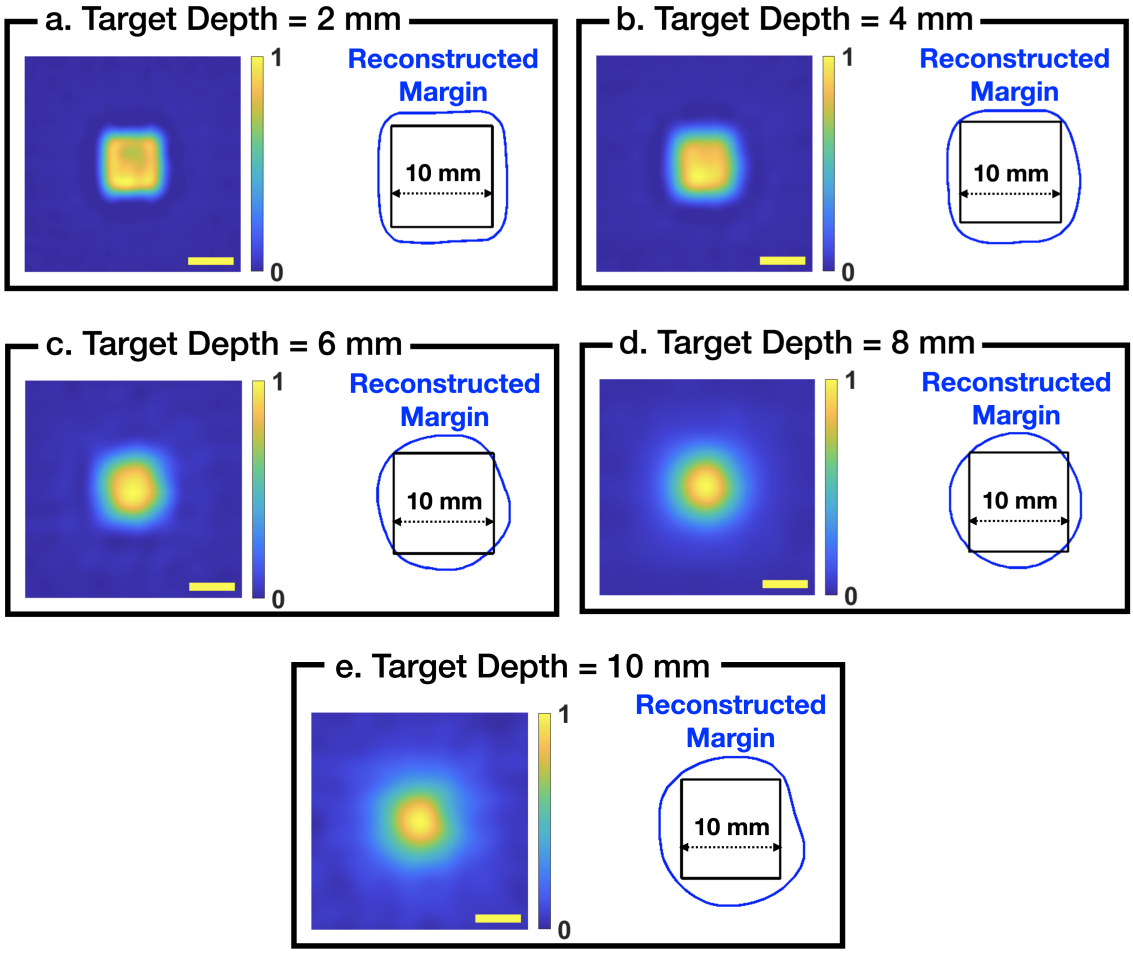

Figure 28: Single target experiment transverse margin estimaion results . The target depth is 2 mm (a), 4 mm (b), 6 mm (c), 8 mm (d), and 10 mm (e). Yellow scale bar indicates 10 mm.

The resulting reconstructions depend on the regularization parameter σ. If σ is too large, the resulting images typically contain significant random noise, which renders the target unrecognizable (see Fig. 29a,). On the other hand, if σ is too small,

the reconstructed image is only a blob (see Fig. 29c). To determine the optimum σ, we apply a weak positivity constraint on $C(\boldsymbol{\rho}, z = z_{\text{target}})$. Since C is intrinsically positive, we require that the mean value of the normalized concentration over all pixels is at least one standard deviation larger than zero; this roughly corresponds to a condition that the fraction of pixels with negative values is less than 16%.

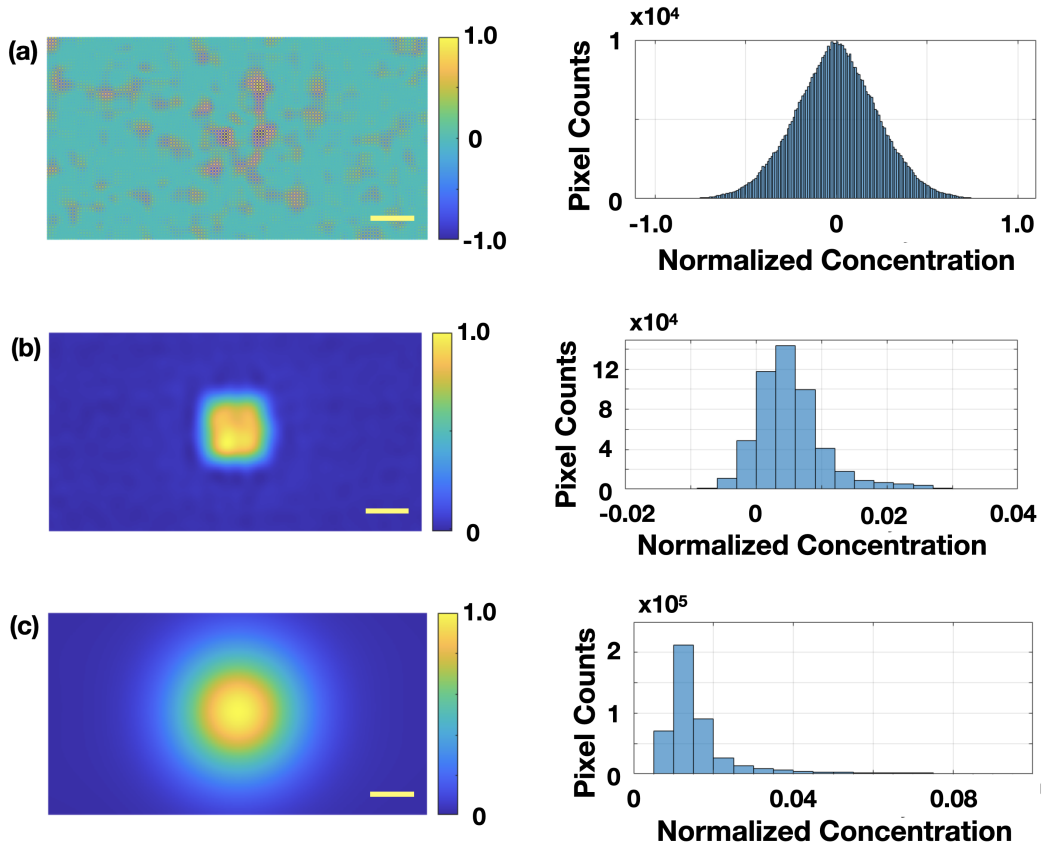

Figure 29: Transverse image of the fluorescent inclusion at 4mm depth with different values of σ. (a) A weak regularization ($\sigma = 3.77$ mm^{-1}). (b) The optimal regularization ($\sigma = 0.46$ mm^{-1}). (c) A strong regularization ($\sigma = 0.11$ mm^{-1}).

The optimal σ we choose is the maximum σ satisfying this constraint. A resultant optimized image is shown in Fig. 29b; the transverse images in the middle column of Fig. 28b are produced using the same positivity constraint.

The lateral margin of the target was set to be the full-width-at-half-maximum

(FWHM) contour line of this distribution (the figures on the right in each panel of Fig. 28). To measure the discrepancy between the reconstructed and true margins, we computed the relative width, which we define as the square root of the ratio of the transverse target area (area confined by the blue line in the figure on the right in each panel of Fig. 28 to the true target area (100 mm^2). For the single-target experiments, the reconstructed depth and the relative width are fairly accurate and are summarized in Fig. 30.

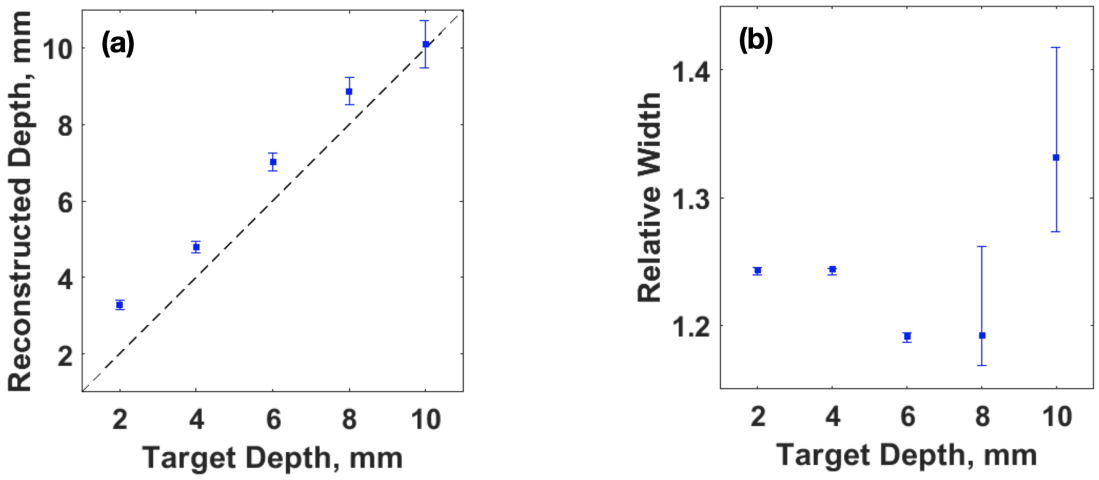

Figure 30: Reconstruction results of single-target experiments. (a) Depth-estimation results. The black dotted line has a unity slope. (b) The ratio between reconstructed image width and the true target width as a function of depth.

6.1.4 Two-target experimental results

Transverse Separation. We first placed two identical targets in the same plane but with varying lateral separation. The estimated depths and transverse margins were then computed. A few examples are shown in Fig. 31 The two targets are clearly distinguished in most cases. As expected, the ability to distinguish between the targets is reduced as the depth is increased. However, for the range of separations used in our experiments, we clearly observe two targets at every depth.

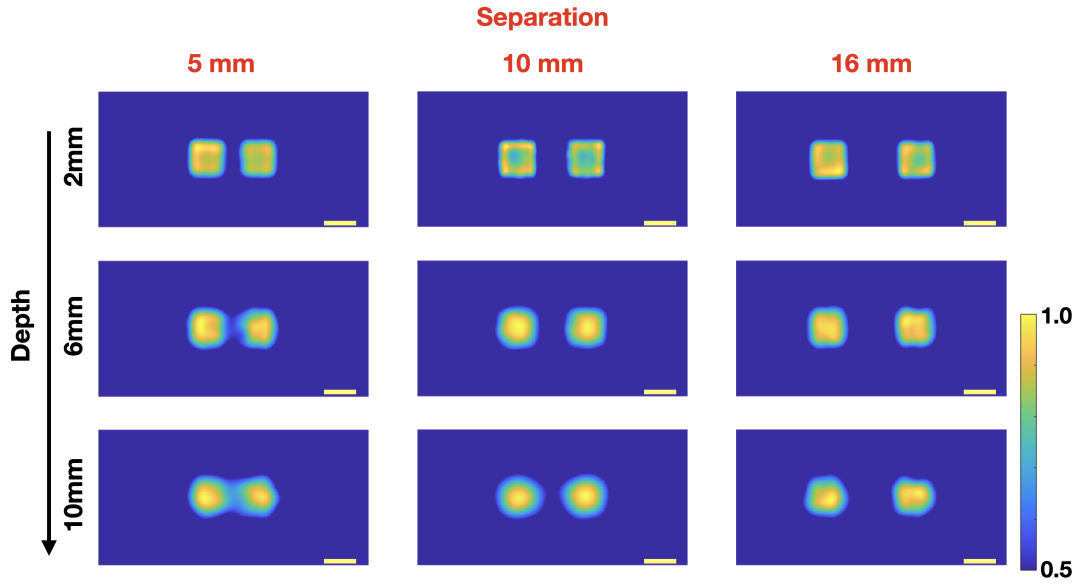

Figure 31: Reconstructed transverse margin of two-target experiment. Two targets were placed on the same depth, and it varied as well as transverse separation.

A summary of depth sensitivity and relative width is given in Figs. 32a and 32b.

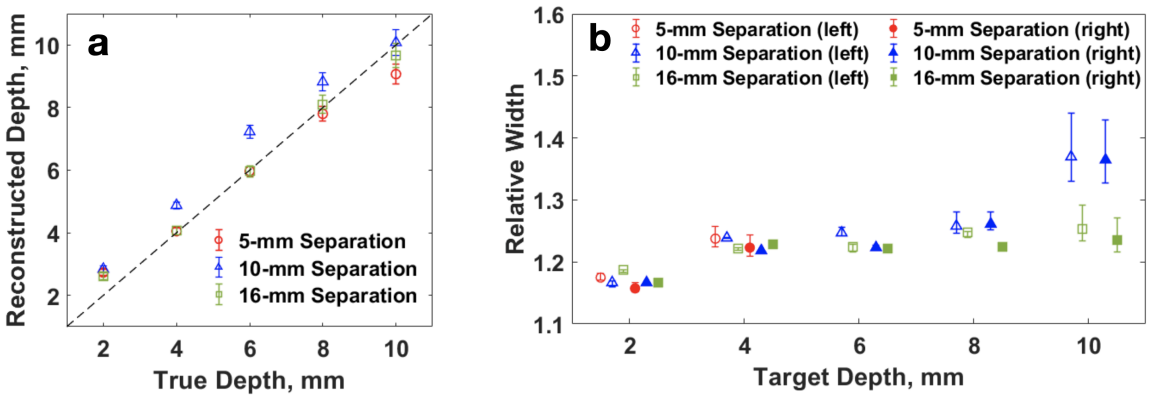

Figure 32: Reconstruction results of two targets in the same vertical plane. (a) Depth-estimation results. (b) Relative width estimation results.

Vertical Separation. The second, more challenging problem, is to reconstruct two targets that are separated both vertically and laterally. To this end, we fixed the lateral separations to be either 20 or 40 mm. The depth of Target 2 was fixed at 2 mm below the surface, and the depth of Target 1 was varied taking the values

4, 6, and 8 mm. Since the targets were well separated transversely, even when they are located at different depths, we could safely segment the data and process each target separately (Fig. 33). We use the minimum in the peak intensity profile along the horizontal (dotted) line A to define the segmentation regions for the image, as shown by the vertical (dashed) lines B in the figure. After the depth of each target was independently estimated, we used these estimates to process the data further for each target. We obtained the transverse fluorophore distributions by utilizing the same algorithm as in the single target reconstructions.

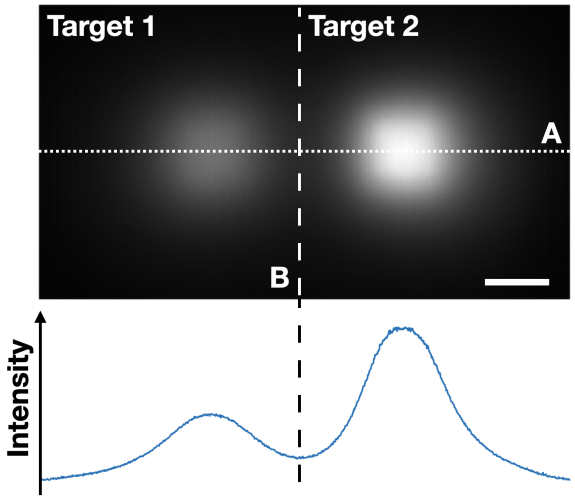

Figure 33: Raw data showing substantially different emission signals from Targets 1 (deep target) and 2 (superficial target). Scale bar corresponds to 10 mm.

Reconstructions with 20 and 40 mm transverse separations are presented in Fig. 34. Columns and rows represent the depth of Target 1 and the transverse separation of the targets, respectively (Target 2 is fixed at the 2 mm depth). Estimated depths are marked below each margin slice. The yellow scale bar represents a 10 mm length in the transverse plane. The vertical scale is exaggerated for better visibility.

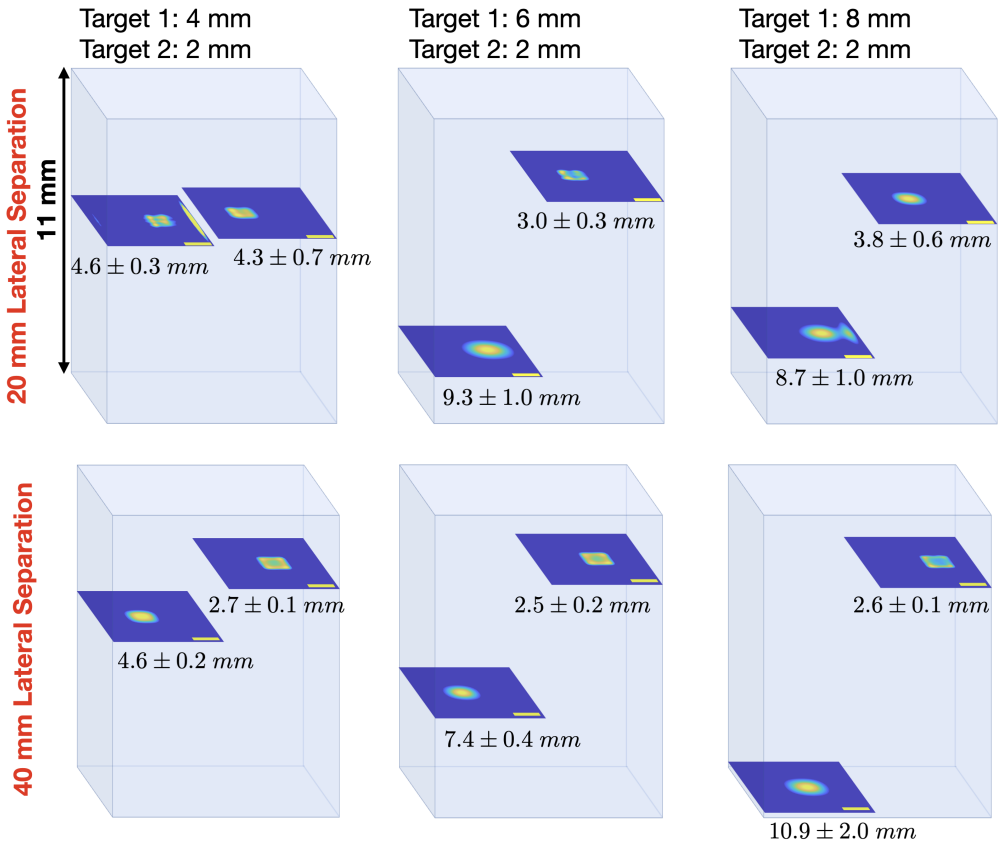

Figure 34: 3D rendering of the two-target vertical separation results.

The depth-sensitivity and depth estimates for these targets (Fig. 35a) are not as good as our results for single targets, nor for two-targets in the same vertical plane (Figs. 30b,32b). This can be understood by noting that both the experimental acquisition time and the resulting computationally processed data are different for different target depths. As described in Chapter 5, the camera exposure times needed to obtain reliable fluorescence images for deeper targets are significantly larger than those for shallow targets. In our instrument and data collection scheme, it was not possible to use large exposure times when a shallow target is present due to the possibility of overexposure. We were therefore forced to use the exposure times appropriate for the shallow target. Thus, when Target 1 is located at the depth of 10 mm, its fluorescent signal was not detectable due to the insufficient exposure time. Cross-talk of the

targets located at different depths can also cause artifacts. As expected, the errors of the transverse margins of the target are larger for smaller horizontal separations (Fig. 35b). When the transverse separation is 20 mm, then the cross-talk from Target 2 in the segmented image of Target 1 becomes significant and produces an artifact near the edge. When this effect is severe, the transverse margins of the deeper target are corrupted (see the last column of the first row of Fig. 34).

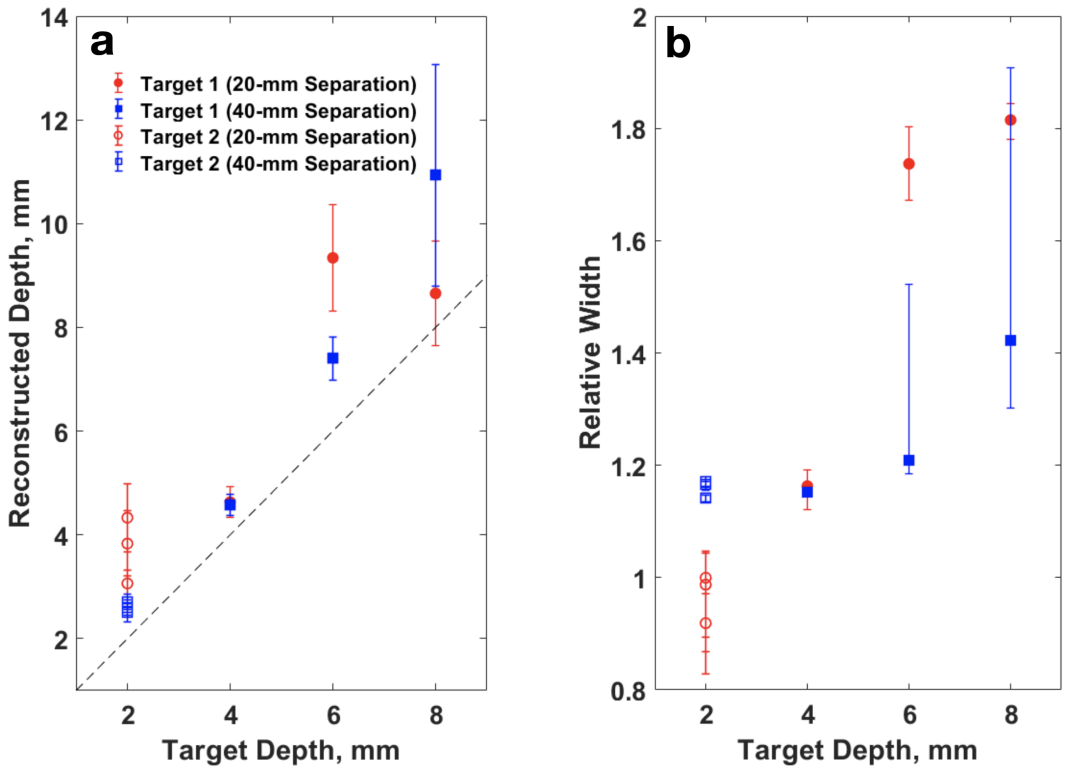

Figure 35: Results of the two-target experiments with vertical separations. (a) Results for the reconstructed depth of Targets 1 and 2. The dashed line has the unity slope. (b) Results of the relative width of Targets 1 and 2.

6.2 Discussion

We have introduced and demonstrated a simple method based on SFD-FDOT to estimate the depth and lateral margins of fluorescent targets in turbid media in the

reflection geometry. The present work moves beyond prior research [74] in several ways. The targets studied are extended rather than point-like and are located as deep as $\sim$ 1 cm below the surface rather than at the shallow depths of $\lesssim$ 3 mm. Also, we considered multiple targets located at the same and different depths rather than a single isolated point-like target. An important but subtle aspect of our work that may not be apparent is that we were able to determine the depth of each target without sensitivity to the regularization parameter (which was the case in the past); this is because we divided the reconstruction into two steps. The first step involves a simple fitting of the data to a single exponent, and the second step involves a straightforward 2D Fourier transform. Essentially, for the second step, we have utilized prior knowledge that the fluorescence signal is mostly emitted from one particular depth, *i.e.*, at the top surface of the target. Approaches that do not rely on these simplifying assumptions generally require the inversion of a severely ill-posed operator. In the latter case, sensitivity to the regularization parameter can become strong.

6.2.1 Depth sensitivity

The simple algorithm proposed in this paper was successful in estimating the depth of fluorescent inclusions to within approximately 1 mm of the true depth in both single-target and two-target experiments in which the targets were at the same depth but laterally separated. Interestingly, the estimation error was minimum at the largest depth (Fig. 36); this observation can be attributed to the effects of ballistic photons which were briefly discussed in Sec. 6.1.3 and which were not accounted for in the reconstructions. We mitigated the effects of ballistic photons by removing the data point with $\boldsymbol{k} = 0$ in the fitting procedure. As noted, these points are affected by the ballistic photons more strongly, especially, in the case of shallow targets. However,

the ballistic contribution still affects the data, most seriously for the target depth of 2 mm. Naturally, as the target moves away from the surface, contributions of the fast-decaying ballistic photons decrease, leading to better depth estimation. In the case of two targets at different depths, the effect of ballistic photons is stronger since at least one target is always close to the surface. This, and the experimental limitations related to the available exposure times, produced a larger error in terms of depth estimation in this set of experiments, typically, of the order of 20% to 40% of the true depth.

Clearly, technical improvements that can ameliorate some of the observed limitations are possible in future work. By increasing the number of low spatial frequencies used in the fitting, we can, potentially, use a more precise two-exponent model [138] for nonlinear fitting of depth. The theoretical model in this case will account for both ballistic and diffuse photons. This will increase the dynamic range of useful data and reduce the systematic errors of the theoretical model. In addition to reducing depth estimation errors of shallow targets, such improvements could enable imaging of targets located deeper than 10 mm below the surface.

6.2.2 Transverse margins

Another important advance reported in this paper is the ability to constrain the transverse margins of the fluorescent inclusions (tumors). For the most part, the transverse margins of the single targets, or two targets in the same plane, overestimated the true margins by 30% or less. For the two-target experiments with targets at different depths, these margin errors were larger; the larger error in depth-estimation propagates to the error in the transverse margin.

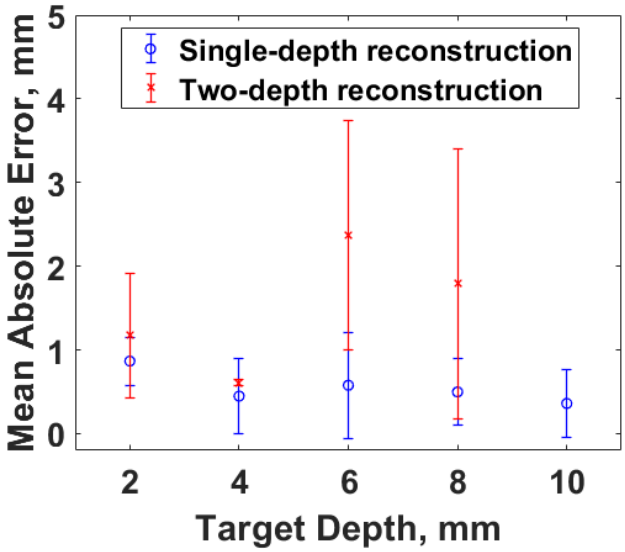

Figure 36: Mean absolute errors for all depth estimation results.

6.2.3 The spatial smoothing (regularization) parameter

Figure 37 shows the average value of the optimized regularization parameter σ as a function of the target depth for single-depth reconstructions. It can be seen that the regularization parameter tends to decrease as the target depth increases. This is because the signal-to-noise ratio for the detected fluorescent intensity decreases as the pathlength of light increases and the spatial waves at high spatial frequencies in the detected intensity distribution become dominated by noise. Empirically, we note that the value of k for which $y(\boldsymbol{k})$ settles into the noise plateau is roughly proportional to the optimal σ (roughly, $k \sim \sigma$). Therefore, the value of k can be considered as a guideline for choosing the optimal σ.

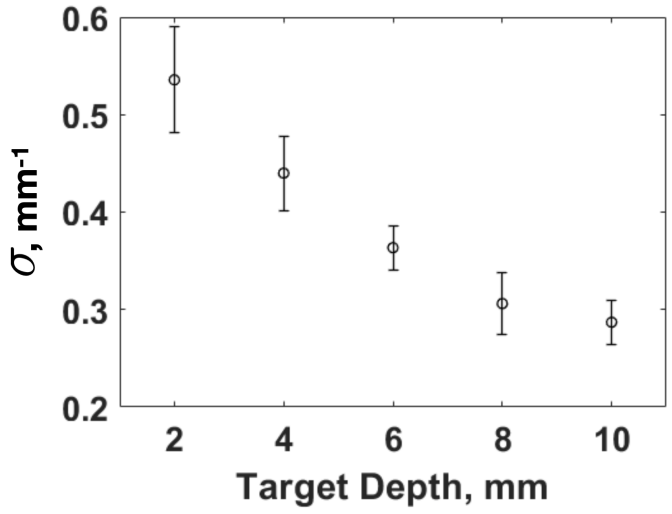

Figure 37: Optimized regularization parameter σ for single-depth reconstruction as a function of the target depth.

6.2.4 Stability of the estimates

The proposed two-step reconstruction method utilizes a Green's function formalism that is affected by the optical properties of the background. Therefore, errors in the background optical properties could lead to errors in the estimation of the depth and transverse margin of the fluorescent targets. We tested the stability of reconstructions by introducing a $\pm 10\%$ error into μ_a and μ_s'. The resulting absolute error of depth estimation was less than 0.8 mm, which does not significantly impact the overall depth sensitivity. Similarly, the change in transverse margins for the targets at the depths of 2, 4, and 6 mm was less than 2%. Thus, while it is desirable to use accurate background optical properties, the method of this paper is found to be stable with respect to relative errors in the optical properties with the magnitude of 10% or less. Note, in practice these background optical properties can be readily measured using the bright-field data sets that are simultaneously taken with the fluorescence data.

6.2.5 Data acquisition and reconstruction times

Since our technique does not attempt to reconstruct full 3D shapes, the time needed to estimate the depth and transverse margins ranged from one to two seconds (Intel(R) Core(TM) i5-8600K CPU 3.60GHz, 6 Cores). Clearly, the approximate approach is different from the traditional analytic inversion and nonlinear image reconstruction techniques, which require computation times ranging from minutes to hours depending on complexity. Acquisition time is the longest temporal factor in our experiments, typically, of the order of a few minutes.

6.2.6 Limitations

The proposed SFD-FDOT estimation methodology is promising though it has the aforementioned limitations. Notably, reconstruction of absolute fluorophore concentration was not pursued; absolute concentration is not a feature currently employed for image guidance or diagnosis. Per image guidance, the analysis assumed homogeneous background optical properties, semi-infinite geometry, and a thin slab geometry of the fluorescence inclusion. In practice, heterogeneous tissue optical properties in brain or lung tissue could generate errors in the estimation of depth and transverse margin. Even though this assumption is commonly used in diffuse optics analysis, more *in vivo* work needs to be done to fully characterize these limitations. Additionally, the instrumentation permits the determination of optical properties of tissue layers using multiple spatial frequencies in principle [161]. This information can be used to refine data analysis and provide guidance on the interpretation of reconstruction results in the future.

Per the semi-infinite geometry, this approximation is fairly good for most situa-

tions in the surgical theatre. In practice, this instrumentation can be readily modified to concurrently measure surface profiles and thereby deduce the magnitude/character of the assumption error; this will also provide concrete data which could be employed to modify the current approach to perturbatively include corrections due to surface curvature.

Per the thin slab approximation for the fluorescence inclusion, in practice, the high absorption coefficient of ICG will cause the top surface of the target to absorb most of the excitation light propagating downward through the target, and consequently the fluorescence emission will be dominated by the signal from the top surface. Thus, the thin slab approximation is useful, as long as the user appreciates that the target depth corresponds to the top surface of the fluorescent region. Note also, even if tumor tissue is not flat on the top surface, the proposed technique will provide a useful estimate of depth that is skewed toward the shallowest part of the tumor.

Another challenge is that our theory only concerns diffuse photons, not ballistic photons. For accurate estimation near surface, it is desirable to develop a comprehensive theory to account for the ballistic photon contribution. Subsequent experiments should characterize the cost versus benefit for practical implementation of the more complex model.

Finally, it is desirable to make measurements quickly in the operating room. In our current setup, the longest part of the procedure is data acquisition (up to eight minutes for the deepest occlusions). In the future, this can be improved by eliminating unnecessary (redundant) spatial modulation frequencies (at high-q) and increasing the excitation light intensity. Note, the current light intensity on the sample surface is smaller than the ANSI limit by the order of 3 (see Appendix A of Ref. 96).

6.3 Summary and Outlook

We modified the SFD-FDOT technique for rapid estimation of the fluorophore target depth and lateral margin. The new methodology was demonstrated to provide depth sensitivity in a variety of experimental situations. The width of the target was estimated with a reasonable negative margin, although this information became less reliable for multiple targets with large vertical separations. These advances build upon the prior work where the target size and depth were limited to point-like occlusions located less than 3 mm below the surface. Moreover, the prior image reconstructions were sensitive to the regularization parameter and the depth resolution was low. The simple and straightforward analytic estimates proposed in the present work are potentially attractive for neuro- and thoracic-surgeries because the technique can rapidly and accurately deliver information about the depth and transverse margins of a fluorescing target.

More broadly, the fluorophore target information obtained in this simple way can provide priors to constrain more complex fluorescence tomography. Applications, in this case, could extend beyond image guidance during tumor resection surgery. Looking forward, the technique can be improved with more rapid and complete data acquisition and type. Additionally, the use of improved theoretical models accounting for the presence of ballistic light can also lead to improvements.

Chapter 7

Summary

Optical imaging of photoluminescence from exogenous contrast agents provides unique opportunities to measure observables that are not easily accessed. The lifetimes of phosphorescent dyes enabled us to measure of oxygen concentration in the vascular and extravascular compartments of the brain, and thereby test traditional models for cerebral metabolism and neurovascular coupling. Moreover, fluorescence imaging is increasingly utilized for image-guided tumor resection surgery, which has largely relied on 2D images in reflection; our technical developments in fluorescence imaging theory and instrumentation, and corresponding experimental demonstrations, have provided advances which can improve upon current techniques for fast characterization of tumor depth and transverse margins.

More specifically, Cerebral Metabolic Rate of Oxygen consumption ($CMRO_2$) is a key physiological variable that characterizes brain oxygen metabolism in steady-state and during functional brain activation. We measured the spatiotemporal variation of $CMRO_2$ in steady-state and during functional activation using with two Oxyphors (one in the vasculature and one in the extravascular tissue) for the first time. To this end, we introduced a new optical technique for minimally-invasive real-time measurement of the oxygen gradients between intravascular and extravascular tissue compartments of the brain using phosphorescence lifetime oximetry. The method enabled computation and tracking of $CMRO_2$ during functional activation with high temporal resolution ($\sim$ 7 Hz), which, in principle, can be improved much more. In parallel, we measured cerebral blood flow (CBF) using laser speckle fluctuation imaging. No-

tably, in contrast to other approaches, our assessment of $CMRO_2$ does not require measurements of CBF or hemoglobin oxygen saturation thus making it possible to compare CBF and $CMRO_2$ as two independent variables.

Simultaneous measurement of p_iO_2 and p_eO_2, from which $CMRO_2$ is deduced, enabled us to explore traditional compartmental models of oxygen dynamics and metabolism in a more rigorous way. In particular, we were able to analyze $CMRO_2$ response using the full dynamic equations (with time-derivatives included) for the first time. Thus, we could compare the predictions of the *full-dynamic* and the *truncated-dynamic* or steady-state models using the same input data. The temporal differences observed at early times took first steps towards more rigorous confrontation of the common assumptions made by the community. The truncated-dynamic $CMRO_2$ closely followed conventional expectation with the dynamics of CBF rising nearly simultaneously but slightly ahead of $CMRO_2$. However, in case of the full-dynamic $CMRO_2$, $CMRO_2$ rapidly rises ahead CBF, p_iO_2 and p_eO_2, triggering CBF response, and then plateaus (briefly) and rises again (following CBF with a slight time-lag). Importantly, these results depend critically on the molecular oxygen mass transfer coefficient, PS_c for transport from inside to outside the capillaries. Our work suggests that the community needs to measure this parameter better. Taken together, the independent records of intravascular and extravascular partial pressures of oxygen (p_iO_2 and p_eO_2), CBF and $CMRO_2$ provided new information about the physiological events that accompany neuronal activation.

In a different vein, our work with Spatial Frequency Domain Fluorescence Diffuse Optical Tomography (SFD-FDOT), which was motivated by fluorescence image-guided surgery for tumor resection, advanced the SFD field and showed how current image-guided surgery techniques based on fluorescence can be improved per depth-specificity and determination of lateral margins. Specifically, we demonstrated rapid

reconstruction algorithms and associated instrumentation using the SFD-FDOT technique, but with compromises that save time and reduce computational complexity. The algorithms utilized the variation of fluorescence intensity with respect to spatial-modulation frequency to compute target depth. Then, using the aforementioned depth information, the lateral margins of fluorescent targets are determined *via* analytical inversion of the data. Both steps are computationally inexpensive and fast. We characterized system performance in experiments with fluorescent contrast targets embedded in tissue-simulating phantoms. Single targets (not point-like) were imaged at varying depths as large as 1 cm, and multiple (two) targets at similar and different depths were also imaged. The experiments suggest that the rapid SFD-FDOT approach could be useful in resection surgery and as a first step for more rigorous SFD-DOT. The experiments also permitted evaluation of current limitations.

Looking forward, we can make clear progress in both arenas by addressing the limitations discussed in Chapter 4 & 6. For simultaneous oxygen measurements, further elucidation and accounting of systematic errors due to the different optical depth penetration (for light excitation of the two Oxyphors) will generate more robust and reliable information about oxygen gradients between intra-/extravascular compartments. Improvements in time-resolution by as much as 50x should also be readily possible with better electronics. With these enhancements, further experiments could shed light on oxygen metabolism study in a variety of situations, *e.g.*, hypoxia, hyperoxia, hypercapnia, etc. Per the SFD-FDOT work, we next need to apply it in clinical settings, *i.e.*, neuro- and thoracic-surgery. This step is important to confirm performance *in vivo* and to understand practical issues that could improve instrumentation. Additionally, development of a theory to account for ballistic photons will improve depth sensitivity and multiple target experiment results.

Appendix

This Appendix has been largely adapted from a pending publication: Chong, S. H., Ong, Y. H., El Khatib, M., Allu, S. R., Parthasarathy, A. B., Greenberg, J. H., Yodh, A. G., & Vinogradov, S. A. (2022). *Real-Time Tracking of Brain Oxygen Gradients and Blood Flow during Functional Activation* [Manuscript submitted for publication]. Department of Physics & Astronomy, University of Pennsylvania.

A.1 General Information

All solvents and reagents were purchased from standard commercial sources and used as received. Polyethyleneglycol-amine monomethyl ether (MeO-PEG-NH_2), Av. MW 1000, was obtained from Laysan Bio. CBzNH-AG[1]OH and PtTPP-OH were synthesized as described previously [80, 44]. Size-exclusion chromatography (SEC) was performed using Bio-Beads S-X1 ($40-80$ μm bead size, Biorad) using THF as a mobile phase. Column chromatography was performed using Selecto^{TM} silica gel (Fisher Scientific). Analytical thin-layer chromatography (TLC) was carried out using silica gel matrix with a fluorescent indicator (layer thickness 200 μm) on aluminum support (SiliCycle). ^{1}H and ^{13}C NMR spectra were recorded on Bruker Neo400 (400.17 MHz for ^{1}H, 100.6 MHz for ^{13}C), UNI600 (600.1 MHz for ^{1}H, 150.9 MHz for ^{13}C) and UNI500 (500.4 MHz for ^{1}H, 125.8 MHz for ^{13}C) spectrometers. Deuterated solvents ($CDCl_3$, CD_2Cl_2, DMSO-d_6) were purchased from Cambridge Isotope Laboratories, Inc. The NMR data were analyzed using MestReNova software (Mestrelab Research). Mass spectra were recorded on a MALDI-TOF Bruker Daltonics Microflex LRF instrument using α-cyano-4-hydroxycinnamicacid (CCA) as a matrix (positive-ion mode). Samples were prepared by mixing a solution of the analyte in THF or

MeOH (10 μL, $\sim$ 1 mM) with a solution of the matrix (100 μL, 10 mg/ml, 0.053 M) in CH_2Cl_2/2-propanol (9:1). The sample, approximately 1 μL, was deposited on the probe tip, dried and analyzed.

Artificial cerebrospinal fluid (aCSF) was supplied by the Cerebrovascular Group in the Department of Anesthesiology and Critical Care at the University of Pennsylvania. The ingredients for preparation of 1 L of aCSF are listed below: diH2O (1 L), KCl (0.220 g), $MgCl_2$ (0.132 g), $CaCl_2$ (0.221 g), urea (0.402 g), dextrose (0.665 g), NaCl (7.710 g), $NaHCO_3$ (0.207 g / 100 mL; added on the day of use).

A.2 Synthesis of Oxyphor PtR4

CBzNH-AG^1(GLuO^{t}Bu)$_2$. To a solution of *N*-(benzyloxycarbonyl)-3,5-dicarboxyphenyl glycineamide, CBzNH-AG^{1}OH (0.744 g, 2 mmol), in DMF (20 ml), a solution of CDMT (0.878 g, 5.0 mmol) in DMF (4 ml) was added at 0^{o}C, followed by immediate addition of *N*-methylmorpholine (1.1 mL, 10 mmol). The reaction mixture was stirred at 0^{o}C for 1 h, then a solution of glutamic acid di-*tert*-butyl ester hydrochloride (1.302 g, 4.4 mmol) in DMF (20 ml) was added, and the reaction mixture was stirred at room temperature for 48 hours. The solvent was removed in vacuum, the resulting oil was dissolved in CH_2Cl_2 (300 ml), washed with HCl aq. (1N, 100 ml), then with $NaHCO_3$ aq. (10%, 2×100 ml) and dried over Na_2SO_4. The product was purified by column chromatography (silica gel, CH_2Cl_2/MeOH, 25 : 1) to give the title compound as a yellowish solid. Yield 1.22 g (78%). 1H NMR (DMSO-d_6), δ (ppm): 1.40 (s, 18H), 1.43 (s, 18H), $1.89-2.10$ (m, 4H), 2.35 (t, $J = 7.6$ Hz, 4H), 3.85 (d, $J = 6.0$ Hz, 2H), $4.33-4.39$ (m, 2H), 5.07 (s, 2H), $7.23-7.39$ (m, 5H), 7.61 (t, $J = 6.4$ Hz, 1H), 8.00 (s, 1H), 8.19 (s, 2H), 8.75(d, $J = 7.2$ Hz, 2H), 10.28 (s, 1H); ^{13}C NMR (DMSO-d_6), δ (ppm): 26.4, 28.1, 28.2, 31.8, 53.1, 66.0, 80.2, 81.1, 121.7, 128.20, 128.25, 128.8,

135.5, 137.5, 139.3, 157.1, 166.9, 168.8, 171.4, 171.9; MALDI-TOF (m/z): calcd. for $C_{44}H_{62}N_4O_{13}$: 854.4, found: 893.5 $[M+K]^+$.

Scheme S1. Synthesis of the Gen2 dendron $\mathbf{NH_2\text{-}AG^1(GluO^tBu)_2}$.

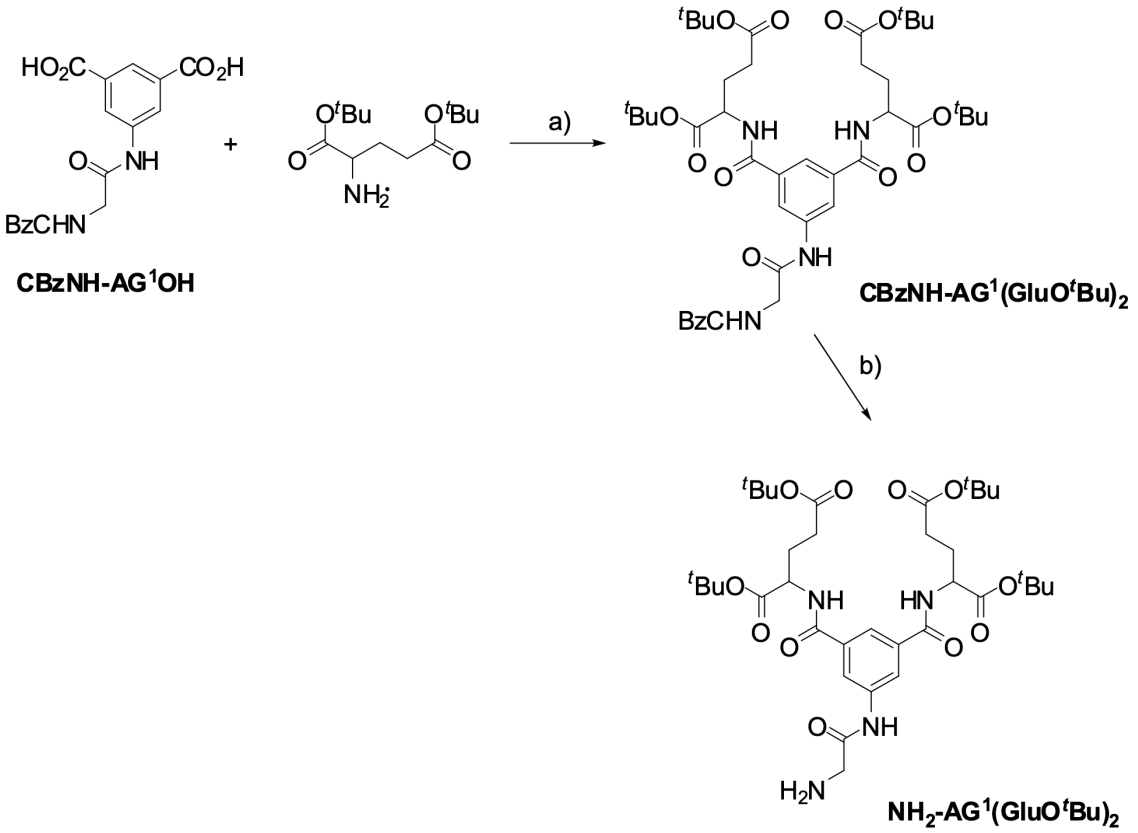

Reagents and conditions: (a) CDMT, *N*-methylmorpholine, DMF, r.t., 48 h (78%); (b) 10 wt. % palladium on carbon, THF, r.t., $14-15$ h (85%).

$\mathbf{NH_2\text{-}AG^1(GluO^tBu)_2}$. CBzNH-$AG^1(GluO^tBu)_2$ (1.2 g, 1.40 mmol) was dissolved in THF:MeOH mixture (100 mL, 1:1), and the solution was deoxygenated by Ar bubbling during $10-15$ min. Pd/C (10 wt%, 100 mg) was added to the solution, and the resulting mixture was flushed with hydrogen gas (H_2) and left under stirring

in H_2 atmosphere (1 atm) for $14 - 15$ h. The resulting mixture was passed through a Celite 545 column and the product was washed off the column with THF:MeOH mixture (200 mL, 1 : 1). Concentrating the washings afforded the title compound as a light-yellow solid. Yield: 0.86 g (85%). ^{1}H NMR (DMSO-d_6), δ (ppm): 1.38 (s, 18H), 1.41 (s, 18H), 1.88-1.96 (m, 2H), 1.99-2.07 (m, 2H), 2.33 (t, $J = 5.6$ Hz, 4H), 3.29 (s, 2H), $4.31 - 4.35$ (m, 2H), 7.99 (s, 1H), 8.23 (s, 2H), 8.72 (d, $J = 6.0$ Hz, 2H); ^{13}C NMR (DMSO-d_6), δ (ppm): 26.4, 28.1, 28.2, 31.8, 45.9, 53.1, 80.3, 81.2, 121.5, 121.6, 135.4, 139.2, 166.9, 171.4, 172.0, 172.8; MALDI-TOF (m/z): calcd. for $C_{36}H_{56}N_4O_{11}$: 720.4, found: 759.5 $[M+K]^+$.

Scheme S2. Synthesis of Oxyphor **PtR4**.

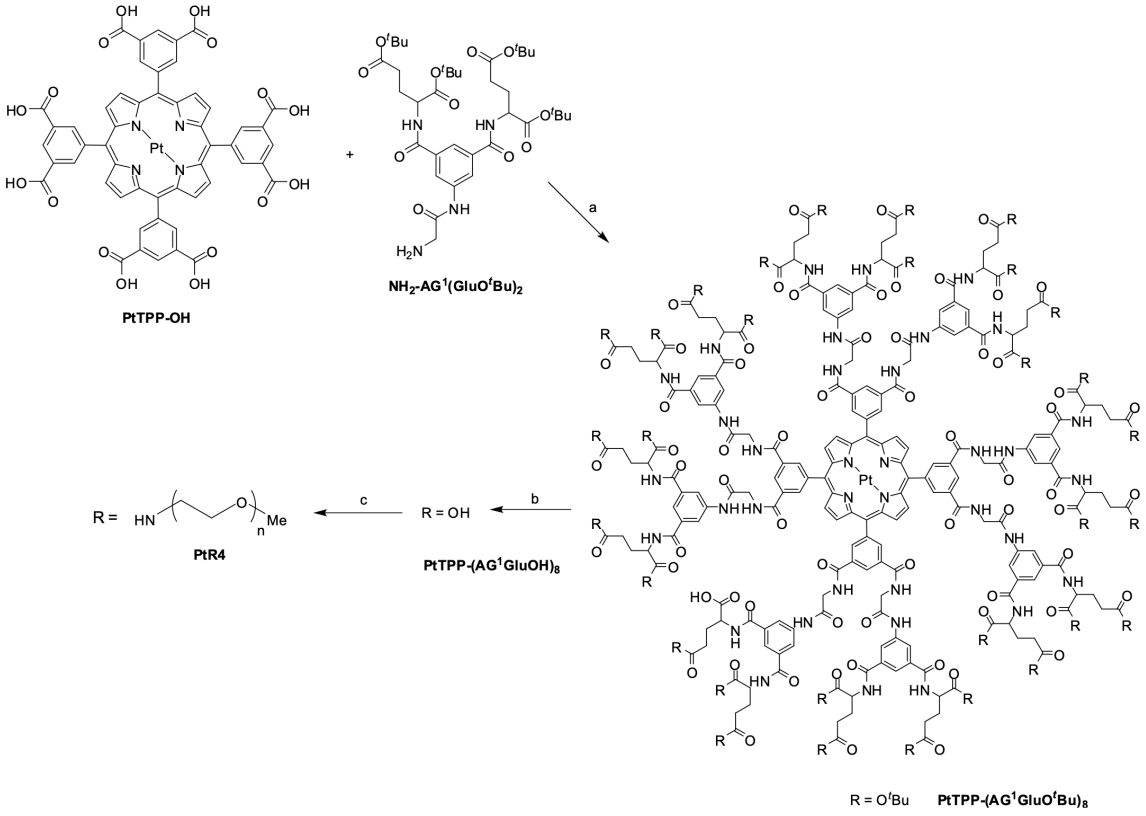

Reagents and conditions: (a) HBTU, DIPEA, DMF, r.t., 96 h (70%); (b) TFA, DCM,

r.t., 2 h (90%); (c) NH_2-PEG (Av. MW$\sim$ 1000), HBTU, DIPEA, DMF, r.t., $10-12$ days (63%).

PtTPP-(AG^{1}GluO^{t}Bu)$_8$. To a solution of PtTPP-OH (0.040 g, 0.034 mmol) in DMF (5 ml), HBTU (0.210 g, 0.554 mmol) was added, and the reaction mixture was stirred for 10 min at room temperature. N,N-diisopropylethylamine (0.19 mL, 0.554 mmol) was added to the mixture, immediately followed by addition of NH_2-AG^1(GluO^{t}Bu)$_2$ (0.4 g, 0.544 mmol). The resulting mixture was stirred at r.t. for 96 h. The reaction mixture was poured into aqueous HCl (5%, 30 ml). The resulting red precipitate was collected by centrifugation, washed with water (2×10 ml) and dried in vacuum. After purification by SEC (S-X1, THF), the title porphyrin-dendrimer was isolated as a red solid. Yield: 0.162 g (70%). ^{1}H NMR (DMSO-d_6), δ (ppm): $1.34, 1.35$ and 1.38 (s, 288H), $1.87-2.05$ (m, 32H), $2.30-2.33$ (m, 32H), 4.18 (br s, 16H), $4.31-4.35$ (m, 16H), 6.62 (s, 4H), 6.86 (s, 8H), 7.99 (s, 8H), 8.21 (s, 16H), 8.71 (d, $J = 6.0$ Hz, 16H), $8.88-8.92$ (m, 16H), 9.01 (s, 4H), 9.34 (s, 8H), 10.4 (s, 8H).

PtTPP-(AG^{1}GluOH)$_8$. To a solution of PtTPP-(AG^{1}GluO^{t}Bu)$_8$ (0.115 g, 0.017 mmol) in dichloromethane (10 ml), trifluoroacetic acid (5 mL) was added dropwise, and the mixture was stirred at r.t. for 2 h. The solvents were removed in a vacuum, after which DCM (10 mL) was added and evaporated again. This procedure was repeated twice to remove the remaining traces of TFA, after which the resulting precipitate was dried. The product was used in the following step without further purification. Yield: 0.076 g (90%).

Oxyphor PtR4. To a solution of PtTPP-(AG^{1}GluOH)$_8$ (0.075 g, 0.015 mmol) in DMF (10 ml), HBTU (0.364 g, 0.96 mmol) was added, and the reaction mixture was stirred for 10 min at room temperature. DIPEA (0.67 mL, 3.84 mmol) was added to

the mixture, followed by the addition of solid mPEG-Amine (MW 1000, 0.96 g, 0.96 mmol). The reaction mixture was stirred at room temperature for 7 days. Additional portions of HBTU (0.182 g, 0.48 mmol) and mPEG-Amine (MW 1000, 0.48 g, 0.48 mmol) were added to the mixture, and stirring continued for additional 5 days. The reaction mixture was poured into diethyl ether (100 mL) and sonicated. The obtained mixture was centrifuged, the supernatant was discarded, and the remaining dark red viscous material was dissolved in THF (10 mL) and subjected to SEC (Bioard S-X1, THF). The red-orange fraction was collected, the solvent was removed in a vacuum and the product was dried. PtR4 was isolated as a dark red solid. Yield: 0.345 g (63%).

A.3 Photophysical Properties of Oxyphor PtR4

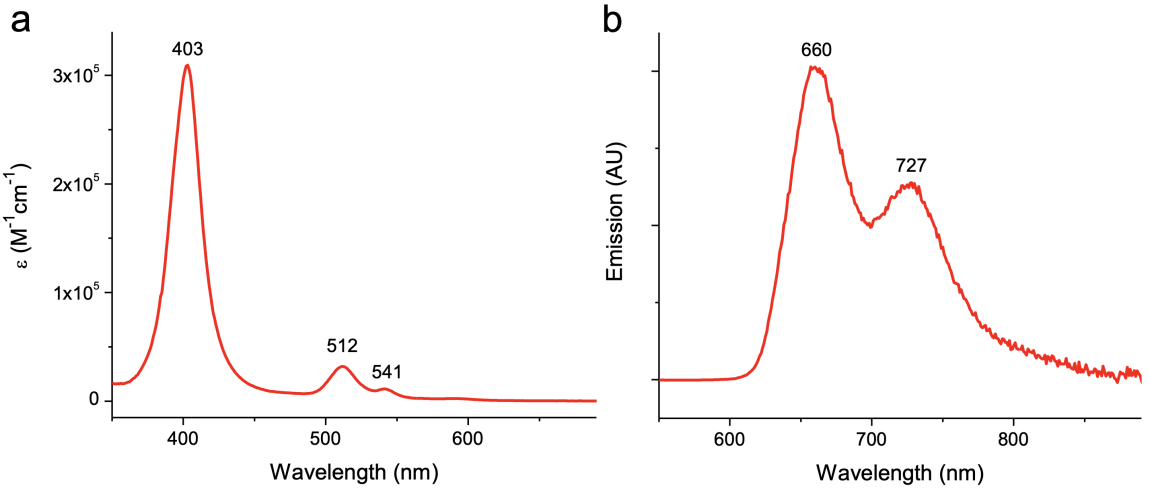

Figure 38: Absorption (a) and phosphorescence (b) spectra of Oxyphor PtR4 in 50 mM phosphate buffer solution (pH 7.1, λ_{ex} = 512 nm).

The absorption spectrum of PtR4 recorded in 50 mM phosphate buffer solution (pH 7.2) shows no traces of aggregation (Fig. 38). The photophysical properties of Oxyphor PtR4 are summarized in Table A1. The phosphorescence emission maximum is 727 nm. The phosphorescence quantum yield was measured in an aqueous

solution (phosphate buffer, pH 7.2, 23^{o}C) relative to the fluorescence of rhodamine 6G (Rh6G) in EtOH ($\phi_{fl} = 0.94$) and found to be 0.053.

Table 8: Photophysical constants of Oxyphor PtR4

Probe	Absorption, nm ($\varepsilon \times 10^{-4}$, $M^{-1}cm^{-1}$)^c	Emission^a λ_{max} nm	ϕ / τ_0 (μs)^b
PtR4	403 (30.9) 512 (3.2)	660, 727	0.053 / 44

^{a}The emission spectra were recorded in 50 mM phosphate buffer solution (pH 7.2, 23^{o}C), deoxygenated by Ar. ^{b}The phosphorescence quantum yield (ϕ) was determined relative to the fluorescence of Rh6G (ϕ_{fl}=0.94) in EtOH; the phosphorescence lifetime at zero oxygen (τ_0) was measured using a solution deoxygenated by Ar. ^{c}The extinction coefficient was determined assuming the molecular weight of 36,410 Da.

A.4 Oxygen Quenching Properties of Oxyphor PtR4

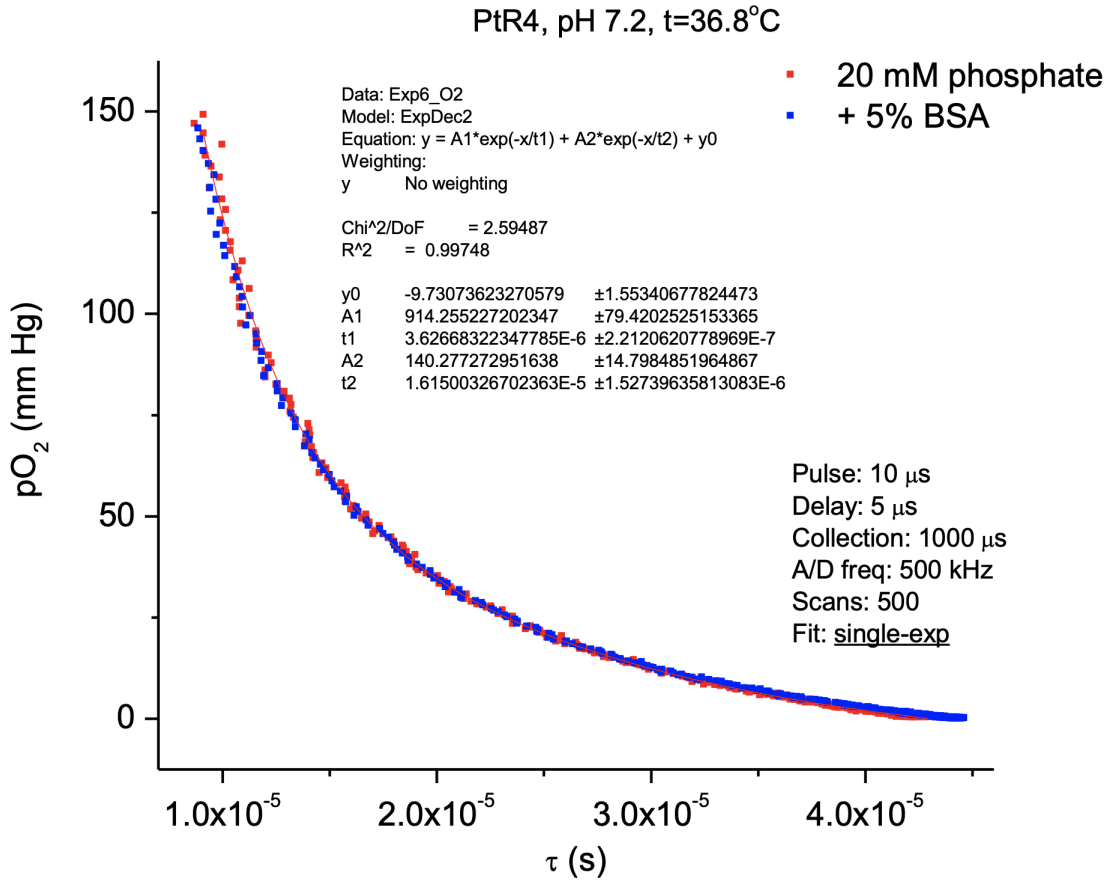

Figure 39: Phosphorescence quenching plot of Oxyphor PtR4.

The oxygen quenching plots of Oxyphor PtR4 were measured in buffered aqueous solutions (20 mM phosphate, pH 7.2) in the absence and presence of bovine serum albumin (BSA, 5%) and found to be nearly identical (Fig. 39). The data were fitted to an empirical bi-exponential form (shown in Fig. 39), and its coefficients were used to convert the phosphorescence lifetime measured *in vivo* to pO_2. The phosphorescence lifetime of Oxyphor PtR4 changes from ~ 8 μs at air saturation to ~ 43 μs at zero-oxygen at (36.8^{o}C).

A.5 Optical Filter Configuration of Two-channel Phosphorometer

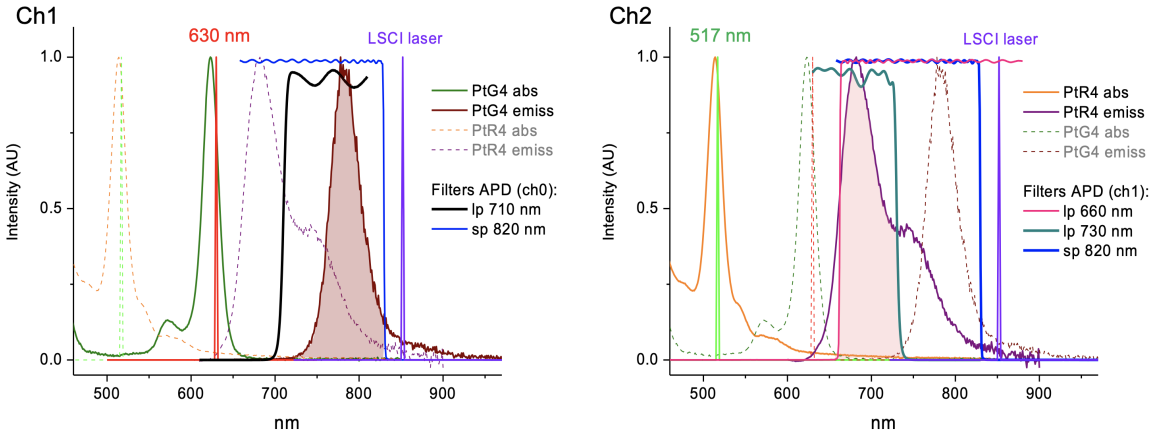

Figure 40: Optical absorption and emission spectra of the probes and associated laser lines and optical filters in Channels 1 and 2 of the phosphorometer. The spectral ranges seen by the detectors (APDs) are shown by shaded areas. **lp** is the abbreviation for *long-pass filter*, and **sp** is for *short-pass filter*.

Bibliography

[1] Abascal, J. F., Chamorro-Servent, J., Aguirre, J., Arridge, S., Correia, T., Ripoll, J., Vaquero, J. J., & Desco, M. (2011). Fluorescence diffuse optical tomography using the split Bregman method. *Med Phys*, **38**(11), 6275-6284. doi:10.1118/1.3656063

[2] Abbasizadeh, N., & Spencer, J. A. (2021). Two-Photon Phosphorescence Lifetime Microscopy. *Adv Exp Med Biol*, **3233**, 63-82. doi:10.1007/978-981-15-7627-0_4

[3] Akorn, Inc. (2006) IC-GREEN™, Indocyanine Green for Injection, USP. Buffalo Grove, IL: Author

[4] Ances, B. M., Wilson, D. F., Greenberg, J. H., & Detre, J. A. (2001). Dynamic changes in cerebral blood flow, O2 tension and calculated cerebral metabolic rate of O2 during functional activation using oxygen phosphorescence quenching. *J. Cereb. Blood Flow Metab.*, **21**(5), 511-516. doi:10.1097/00004647-200105000-00005

[5] Aronson, R. (1995). Boundary conditions for diffusion of light. *J Opt Soc Am A Opt Image Sci Vis*, **12**(11), 2532-2539. doi:10.1364/josaa.12.002532

[6] Azari, F., Kennedy, G., Bernstein, E., Hadjipanayis, C., Vahrmeijer, A., Smith, B., . . . Singhal, S. (2021). Intraoperative molecular imaging clinical trials: a review of 2020 conference proceedings. *J Biomed Opt*, **26**(5). doi:10.1117/1.JBO.26.5.050901

[7] Ban, H. Y., Schweiger, M., Kavuri, V. C., Cochran, J. M., Xie, L., Busch, D. R., . . . Yodh, A. G. (2016). Heterodyne frequency-domain multispectral diffuse optical tomography of breast cancer in the parallel-plane transmission geometry. *Med Phys*, **43**(7), 4383. doi:10.1118/1.4953830

[8] Bandyopadhyay, R., Gittings, A. S., Suh, S. S., Dixon, P. K., & Durian, D. J. (2005). Speckle-visibility spectroscopy: A tool to study time-varying dynamics. *Review of Scientific Instruments*, **76**(9), 093110. doi:10.1063/1.2037987

[9] Bezemer, R., Klijn, E., Khalilzada, M., Lima, A., Heger, M., van Bommel, J.,& Ince, C. (2010). Validation of near-infrared laser speckle imaging for assessing microvascular (re) perfusion. *Microvascular research*, **79**(2), 139-143.

[10] Boas, D. A., & Dunn, A. K. (2010). Laser speckle contrast imaging in biomedical optics. *J Biomed Opt*, **15**(1), 011109. doi:10.1117/1.3285504

[11] Boas, D. A., O'Leary, M. A., Chance, B., & Yodh, A. G. (1994). Scattering of diffuse photon density waves by spherical inhomogeneities within turbid media: analytic solution and applications. *Proc Natl Acad Sci U S A*, **91**(11), 4887-4891. doi:10.1073/pnas.91.11.4887

[12] Boero, J. A., Ascher, J., Arregui, A., Rovainen, C., & Woolsey, T. A. (1999). Increased brain capillaries in chronic hypoxia. *J Appl Physiol* (1985), **86**(4), 1211-1219. doi:10.1152/jappl.1999.86.4.1211

[13] Buxton, R. B. (2010). Interpreting oxygenation-based neuroimaging signals: the importance and the challenge of understanding brain oxygen metabolism. *Front. Neuroenergetics*, **2**, 8. doi:10.3389/fnene.2010.00008

[14] Buxton, R. B., & Frank, L. R. (1997). A model for the coupling between cerebral blood flow and oxygen metabolism during neural stimulation. *J. Cereb. Blood Flow Metab.*, **17**(1), 64-72. doi:10.1097/00004647-199701000-00009

[15] Cao, X., Rao Allu, S., Jiang, S., Jia, M., Gunn, J. R., Yao, C., . . . Pogue, B. W. (2020). Tissue pO_2 distributions in xenograft tumors dynamically imaged by Cherenkov-excited phosphorescence during fractionated radiation therapy. *Nat. Commun.*(**1**), 573.

[16] Catapano, G., Sgulo, F. G., Seneca, V., Lepore, G., Columbano, L., & di Nuzzo, G. (2017). Fluorescein-Guided Surgery for High-Grade Glioma Resection: An Intraoperative "Contrast-Enhancer". *World Neurosurg*, **104**, 239-247. doi:10.1016/j.wneu.2017.05.022

[17] Chance, B., & Williams, G. R. (1956). The respiratory chain and oxidative phosphorylation. *Adv Enzymol Relat Subj Biochem*, **17**, 65-134. doi:10.1002/9780470122624.ch2

[18] Christodoulou, C., Spencer, J. A., Yeh, S. C. A., Turcotte, R., Kokkaliaris, K. D., Panero, R., . . . Camargo, F. D. (2020). Live-animal imaging of native haematopoietic stem and progenitor cells. *Nature*, **578**(7794), 278-283. doi:10.1038/s41586-020-1971-z

[19] Clark, D. K., Erdmann, W., Halsey, J. H., & Strong, E. (1977). Oxygen diffusion, conductivity and solubility coefficients in the microarea of the brain. (Measurements with noble metal microelectrodes). *Adv Exp Med Biol*, **94**, 697-704. doi:10.1007/978-1-4684-8890-6_96

[20] Cochran, J. M., Busch, D. R., Leproux, A., Zhang, Z., O'Sullivan, T. D., Cerussi, A. E., . . . Yodh, A. G. (2018). Tissue oxygen saturation predicts

response to breast cancer neoadjuvant chemotherapy within 10 days of treatment. *J Biomed Opt*, **24**(2), 1-11. doi:10.1117/1.JBO.24.2.021202

[21] Cochran, J. M., Leproux, A., Busch, D. R., O'Sullivan, T. D., Yang, W., Mehta, R. S., . . . Yodh, A. G. (2021). Breast cancer differential diagnosis using diffuse optical spectroscopic imaging and regression with z-score normalized data. *J Biomed Opt*, **26**(2). doi:10.1117/1.JBO.26.2.026004

[22] Cooper GM. The Cell: *A Molecular Approach.* 2nd edition. Sunderland (MA): Sinauer Associates; 2000. The Mechanism of Oxidative Phosphorylation. Available from: https://www.ncbi.nlm.nih.gov/books/NBK9885/

[23] Corlu, A., Choe, R., Durduran, T., Rosen, M. A., Schweiger, M., Arridge, S. R., . . . Yodh, A. G. (2007). Three-dimensional in vivo fluorescence diffuse optical tomography of breast cancer in humans. *Opt Express*, **15**(11), 6696-6716. doi:10.1364/oe.15.006696

[24] Correia, T., Ducros, N., D'Andrea, C., Schweiger, M., & Arridge, S. (2013). Quantitative fluorescence diffuse optical tomography in the presence of heterogeneities. *Opt Lett*, **38**(11), 1903-1905. doi:10.1364/OL.38.001903

[25] Culver, J. P., Durduran, T., Furuya, D., Cheung, C., Greenberg, J. H., & Yodh, A. G. (2003). Diffuse optical tomography of cerebral blood flow, oxygenation, and metabolism in rat during focal ischemia. *J Cereb Blood Flow Metab*, **23**(8), 911-924. doi:10.1097/01.WCB.0000076703.71231.BB

[26] Daly, M. J., Wilson, B. C., Irish, J. C., & Jaffray, D. A. (2019). Navigated non-contact fluorescence tomography. *Phys Med Biol*, **64**(13), 135021. doi:10.1088/1361-6560/ab1f33

[27] Davis, S. C., Dehghani, H., Wang, J., Jiang, S., Pogue, B. W., & Paulsen, K. D. (2007). Image-guided diffuse optical fluorescence tomography implemented with Laplacian-type regularization. *Opt Express*, **15**(7), 4066-4082. doi:10.1364/oe.15.004066

[28] De Silva, T. M., & Faraci, F. M. (2017). Chapter 31 - Hypertension. In L. R. Caplan, J. Biller, M. C. Leary, E. H. Lo, A. J. Thomas, M. Yenari, & J. H. Zhang (Eds.), *Primer on Cerebrovascular Diseases* (Second Edition) (pp. 153-157). San Diego: Academic Press.

[29] Debie, P., & Hernot, S. (2019). Emerging Fluorescent Molecular Tracers to Guide Intra-Operative Surgical Decision-Making. *Front Pharmacol*, **10**, 510. doi:10.3389/fphar.2019.00510

[30] Devor, A., Sakadzic, S., Saisan, P. A., Yaseen, M. A., Roussakis, E., Srinivasan, V. J., . . . Boas, D. A. (2011). "Overshoot" of O2 is required to maintain baseline tissue oxygenation at locations distal to blood vessels. *J. Neurosci.*, **31**(38), 13676-13681. doi:10.1523/JNEUROSCI.1968-11.2011

[31] Devor, A., Sakadzic, S., Srinivasan, V. J., Yaseen, M. A., Nizar, K., Saisan, P. A., . . . Boas, D. A. (2012). Frontiers in optical imaging of cerebral blood flow and metabolism. *J Cereb Blood Flow Metab*, **32**(7), 1259-1276. doi:10.1038/jcbfm.2011.195

[32] DiResta, G. R., Lee, J. B., & Arbit, E. (1991). Measurement of brain tissue specific gravity using pycnometry. *J Neurosci Methods*, **39**(3), 245-251. doi:10.1016/0165-0270(91)90103-7

[33] Ducros, N., D'Andrea, C., Valentini, G., Rudge, T., Arridge, S., & Bassi, A. (2010). Full-wavelet approach for fluorescence diffuse optical tomography with structured illumination. *Opt Lett*, **35**(21), 3676-3678. doi:10.1364/OL.35.003676

[34] Dunn, A. K., Bolay, H., Moskowitz, M. A.,& Boas, D. A. (2001). Dynamic imaging of cerebral blood flow using laser speckle. *Journal of Cerebral Blood Flow& Metabolism*, **21**(3), 195-201.

[35] Dunn, A. K., Devor, A., Dale, A. M., & Boas, D. A. (2005). Spatial extent of oxygen metabolism and hemodynamic changes during functional activation of the rat somatosensory cortex. *Neuroimage*, **27**(2), 279-290. doi:10.1016/j.neuroimage.2005.04.024

[36] Durduran, T., Choe, R., Baker, W. B., & Yodh, A. G. (2010). Diffuse Optics for Tissue Monitoring and Tomography. *Rep Prog Phys*, **73**(7). doi:10.1088/0034-4885/73/7/076701

[37] Durduran, T., Choe, R., Culver, J. P., Zubkov, L., Holboke, M. J., Giammarco, J., . . . Yodh, A. G. (2002). Bulk optical properties of healthy female breast tissue. *Phys Med Biol*, **47**(16), 2847-2861. doi:10.1088/0031-9155/47/16/302

[38] Durduran, T., & Yodh, A. G. (2014). Diffuse correlation spectroscopy for non-invasive, micro-vascular cerebral blood flow measurement. *Neuroimage*, **85** Pt 1, 51-63. doi:10.1016/j.neuroimage.2013.06.017

[39] Durduran, T., Yu, G., Burnett, M. G., Detre, J. A., Greenberg, J. H., Wang, J., . . . Yodh, A. G. (2004). Diffuse optical measurement of blood flow, blood oxygenation, and metabolism in a human brain during sensorimotor cortex activation. *Opt. Lett.*, **29**(15), 1766-1768. doi:10.1364/ol.29.001766

[40] Dzurinko, V. L., Gurwood, A. S., & Price, J. R. (2004). Intravenous and indocyanine green angiography. *Optometry*, **75**(12), 743-755. doi:10.1016/s1529-1839(04)70234-1

[41] Eklof, B., Lassen, N. A., Nilsson, L., Norberg, K., & Siesjo, B. K. (1973). Blood flow and metabolic rate for oxygen in the cerebral cortex of the rat. *Acta. Physiol. Scand.*, **88**(4), 587-589. doi:10.1111/j.1748-1716.1973.tb05489.x

[42] Elliott, J. T., Dsouza, A. V., Davis, S. C., Olson, J. D., Paulsen, K. D., Roberts, D. W., & Pogue, B. W. (2015). Review of fluorescence guided surgery visualization and overlay techniques. *Biomed Opt Express*, **6**(10), 3765-3782. doi:10.1364/BOE.6.003765

[43] Esipova, T. V., Barrett, M. J. P., Erlebach, E., Masunov, A. E., Weber, B., & Vinogradov, S. A. (2019). Oxyphor 2P: A High-Performance Probe for Deep-Tissue Longitudinal Oxygen Imaging. *Cell Metab*, **29**(3), 736-744 e737. doi:10.1016/j.cmet.2018.12.022

[44] Esipova, T. V., Karagodov, A., Miller, J., Wilson, D. F., Busch, T. M., & Vinogradov, S. A. (2011). Two new "protected" oxyphors for biological oximetry: properties and application in tumor imaging. *Anal Chem*, **83**(22), 8756-8765. doi:10.1021/ac2022234

[45] Fan, A. P., An, H., Moradi, F., Rosenberg, J., Ishii, Y., Nariai, T., . . . Zaharchuk, G. (2020). Quantification of brain oxygen extraction and metabolism with 15O-gas PET: A technical review in the era of PET/MRI. *Neuroimage*, **220**, 117136. doi:10.1016/j.neuroimage.2020.117136

[46] Fang, Q., & Boas, D. A. (2009). Monte Carlo simulation of photon migration in 3D turbid media accelerated by graphics processing units. *Opt Express*, **17**(22), 20178-20190. doi:10.1364/OE.17.020178

[47] Ferrari, M., & Quaresima, V. (2012). A brief review on the history of human functional near-infrared spectroscopy (fNIRS) development and fields of application. *Neuroimage*, **63**(2), 921-935. doi:10.1016/j.neuroimage.2012.03.049

[48] Finikova, O. S., Lebedev, A. Y., Aprelev, A., Troxler, T., Gao, F., Garnacho, C., . . . Vinogradov, S. A. (2008). Oxygen microscopy by two-photon-excited phosphorescence. *ChemPhysChem*, **9**(12), 1673-1679. doi:10.1002/cphc.200800296

[49] Flexman, M. L., Kim, H. K., Gunther, J. E., Lim, E. A., Alvarez, M. C., Desperito, E., . . . Hielscher, A. H. (2013). Optical biomarkers for breast cancer derived from dynamic diffuse optical tomography. *J Biomed Opt*, **18**(9), 096012. doi:10.1117/1.JBO.18.9.096012

[50] Fortin, P. Y., Genevois, C., Koenig, A., Heinrich, E., Texier, I., & Couillaud, F. (2012). Detection of brain tumors using fluorescence diffuse optical tomography and nanoparticles as contrast agents. *J Biomed Opt*, **17**(12), 126004. doi:10.1117/1.JBO.17.12.126004

[51] Gagnon, L., Sakadzic, S., Lesage, F., Musacchia, J. J., Lefebvre, J., Fang, Q., . . . Boas, D. A. (2015). Quantifying the microvascular origin of BOLD-fMRI from first principles with two-photon microscopy and an oxygen-sensitive nanoprobe. *J Neurosci*, **35**(8), 3663-3675. doi:10.1523/JNEUROSCI.3555-14.2015

[52] Ganfield, R. A., Nair, P., & Whalen, W. J. (1970). Mass transfer, storage, and utilization of O2 in cat cerebral cortex. *Am J Physiol*, **219**(3), 814-821. doi:10.1152/ajplegacy.1970.219.3.814

[53] Gao, F., Zhao, H., Zhang, L., Tanikawa, Y., Marjono, A., & Yamada, Y. (2008). A self-normalized, full time-resolved method for fluorescence diffuse optical tomography. *Opt Express*, **16**(17), 13104-13121. doi:10.1364/oe.16.013104

[54] Girouard, H., & Iadecola, C. (2006). Neurovascular coupling in the normal brain and in hypertension, stroke, and Alzheimer disease. *J. Appl. Physiol.*, **100**(1), 328-335. doi:10.1152/japplphysiol.00966.2005

[55] Gjedde, A., Johannsen, P., Cold, G. E., & Ostergaard, L. (2005). Cerebral metabolic response to low blood flow: possible role of cytochrome oxidase inhibition. *J Cereb Blood Flow Metab*, **25**(9), 1183-1196. doi:10.1038/sj.jcbfm.9600113

[56] Goodman, J. W. (2007). *Speckle phenomena in optics: theory and applications*: Roberts and Company Publishers.

[57] Gross, P. M., Sposito, N. M., Pettersen, S. E., & Fenstermacher, J. D. (1986). Differences in function and structure of the capillary endothelium in gray matter, white matter and a circumventricular organ of rat brain. *Blood Vessels*, **23**(6), 261-270. doi:10.1159/000158652

[58] Guidolin, D., Marcoli, M., Tortorella, C., Maura, G., & Agnati, L. F. (2019). Receptor-Receptor Interactions as a Widespread Phenomenon: Novel Targets for Drug Development? *Front Endocrinol (Lausanne)*, **10**, 53. doi:10.3389/fendo.2019.00053

[59] Hayashi, T., Watabe, H., Kudomi, N., Kim, K. M., Enmi, J., Hayashida, K., & Iida, H. (2003). A theoretical model of oxygen delivery and metabolism for physiologic interpretation of quantitative cerebral blood flow and metabolic rate of oxygen. *J Cereb Blood Flow Metab*, **23**(11), 1314-1323. doi:10.1097/01.WCB.0000090506.76664.00

[60] Hendrikx, D., Smits, A., Lavanga, M., De Wel, O., Thewissen, L., Jansen, K., ... & Naulaers, G. (2019). Measurement of neurovascular coupling in neonates. *Frontiers in physiology*, **10**—, 65.

[61] Hoge, R. D., Franceschini, M. A., Covolan, R. J., Huppert, T., Mandeville, J. B., & Boas, D. A. (2005). Simultaneous recording of task-induced changes in blood oxygenation, volume, and flow using diffuse optical imaging and arterial spin-labeling MRI. *Neuroimage*, **25**(3), 701-707. doi:10.1016/j.neuroimage.2004.12.032

[62] Holt, D., Parthasarathy, A. B., Okusanya, O., Keating, J., Venegas, O., Deshpande, C., . . . Singhal, S. (2015). Intraoperative near-infrared fluorescence imaging and spectroscopy identifies residual tumor cells in wounds. *J Biomed Opt*, **20**(7), 76002. doi:10.1117/1.JBO.20.7.076002

[63] Homer, L. D., Shelton, J. B., & Williams, T. J. (1983). Diffusion of oxygen in slices of rat brain. *Am J Physiol*, **244**(1), R15-22. doi:10.1152/ajpregu.1983.244.1.R15

[64] Hyder, F., Shulman, R. G., & Rothman, D. L. (1998). A model for the regulation of cerebral oxygen delivery. *J Appl Physiol* (1985), **85**(2), 554-564. doi:10.1152/jappl.1998.85.2.554

[65] Iadecola, C. (2017). The neurovascular unit coming of age: a iourney through neurovascular coupling in health and disease. *Neuron*, **96**(1), 17-42. doi:10.1016/j.neuron.2017.07.030

[66] Ibaraki, M., Miura, S., Shimosegawa, E., Sugawara, S., Mizuta, T., Ishikawa, A., & Amano, M. (2008). Quantification of cerebral blood flow and oxygen metabolism with 3-dimensional PET and 15O: validation by comparison with 2-dimensional PET. *J Nucl Med*, **49**(1), 50-59. doi:10.2967/jnumed.107.044008

[67] Jespersen, S. N., & Østergaard, L. (2012). The roles of cerebral blood flow, capillary transit time heterogeneity, and oxygen tension in brain oxygenation and metabolism. *Journal of cerebral blood flow & metabolism*, **32**(2), 264-277.

[68] Kassissia, I. G., Goresky, C. A., Rose, C. P., Schwab, A. J., Simard, A., Huet, P. M., & Bach, G. G. (1995). Tracer oxygen distribution is barrier-limited in the cerebral microcirculation. *Circ Res*, **77**(6), 1201-1211. doi:10.1161/01.res.77.6.1201

[69] Kazmi, S. S., Faraji, E., Davis, M. A., Huang, Y. Y., Zhang, X. J.,& Dunn, A. K. (2015). Flux or speed? Examining speckle contrast imaging of vascular flows. *Biomedical optics express*, **6**(7), 2588-2608.

[70] Kim, J. H., & Ress, D. (2016). Arterial impulse model for the BOLD response to brief neural activation. *Neuroimage*, **124**(Pt A), 394-408. doi:10.1016/j.neuroimage.2015.08.068

[71] Kim, T., Hendrich, K. S., Masamoto, K., & Kim, S. G. (2007). Arterial versus total blood volume changes during neural activity-induced cerebral blood flow change: implication for BOLD fMRI. *J Cereb Blood Flow Metab*, **27**(6), 1235-1247. doi:10.1038/sj.jcbfm.9600429

[72] Kobayashi, H., & Choyke, P. L. (2011). Target-cancer-cell-specific activatable fluorescence imaging probes: rational design and in vivo applications. *Acc Chem Res*, **44**(2), 83-90. doi:10.1021/ar1000633

[73] Kobayashi, M., Mori, T., Kiyono, Y., Tiwari, V. N., Maruyama, R., Kawai, K., & Okazawa, H. (2012). Cerebral oxygen metabolism of rats using injectable (15)O-oxygen with a steady-state method. *J Cereb Blood Flow Metab*, **32**(1), 33-40. doi:10.1038/jcbfm.2011.125

[74] Konecky, S. D., Owen, C. M., Rice, T., Valdes, P. A., Kolste, K., Wilson, B. C., . . . Tromberg, B. J. (2012). Spatial frequency domain tomography of protoporphyrin IX fluorescence in preclinical glioma models. *J Biomed Opt*, **17**(5), 056008. doi:10.1117/1.JBO.17.5.056008

[75] Krogh, A. (1919). The supply of oxygen to the tissues and the regulation of the capillary circulation. *J. Physiol.*, **52**(6), 457-474. doi:10.1113/jphysiol.1919.sp001844

[76] Kudomi, N., Hayashi, T., Teramoto, N., Watabe, H., Kawachi, N., Ohta, Y., . . . Iida, H. (2005). Rapid quantitative measurement of CMRO(2) and CBF by dual administration of (15)O-labeled oxygen and water during a single PET scan-a validation study and error analysis in anesthetized monkeys. *J Cereb Blood Flow Metab*, **25**(9), 1209-1224. doi:10.1038/sj.jcbfm.9600118

[77] LaManna, J. C. (2007). Hypoxia in the central nervous system. *Essays Biochem*, **43**, 139-151. doi:10.1042/BSE0430139

[78] Lapointe, E., Pichette, J., & Berube-Lauziere, Y. (2012). A multi-view time-domain non-contact diffuse optical tomography scanner with dual wavelength detection for intrinsic and fluorescence small animal imaging. *Rev Sci Instrum*, **83**(6), 063703. doi:10.1063/1.4726016

[79] Laursen, H., & Diemer, N. H. (1977). Capillary size and density in the cerebral cortex of rats with a porto-caval anastomosis. *Acta Neuropathol*, **40**(2), 117-122. doi:10.1007/BF00688699

[80] Lebedev, A. Y., Cheprakov, A. V., Sakadzic, S., Boas, D. A., Wilson, D. F., & Vinogradov, S. A. (2009). Dendritic phosphorescent probes for oxygen imaging in biological systems. *ACS Appl. Mater. Interfaces*, **1**(6), 1292-1304. Retrieved from ¡Go to ISI¿://000267513100024 https://www.ncbi.nlm.nih.gov/pmc/articles/PMC2805241/pdf/nihms163292.pdf

[81] Leblond, F., Ovanesyan, Z., Davis, S. C., Valdes, P. A., Kim, A., Hartov, A., . . . Roberts, D. W. (2011). Analytic expression of fluorescence ratio detection correlates with depth in multi-spectral sub-surface imaging. *Phys Med Biol*, **56**(21), 6823-6837. doi:10.1088/0031-9155/56/21/005

[82] Lecoq, J., Parpaleix, A., Roussakis, E., Ducros, M., Goulam Houssen, Y., Vinogradov, S. A., & Charpak, S. (2011). Simultaneous two-photon imaging of oxygen and blood flow in deep cerebral vessels. *Nat. Med.*, **17**(7), 893-898. doi:10.1038/nm.2394

[83] Lee, J. Y., Thawani, J. P., Pierce, J., Zeh, R., Martinez-Lage, M., Chanin, M., . . . Singhal, S. (2016). Intraoperative Near-Infrared Optical Imaging Can Localize Gadolinium-Enhancing Gliomas During Surgery. *Neurosurgery*, **79**(6), 856-871. doi:10.1227/NEU.0000000000001450

[84] Lee, J. Y. K., Pierce, J. T., Zeh, R., Cho, S. S., Salinas, R., Nie, S., & Singhal, S. (2017). Intraoperative Near-Infrared Optical Contrast Can Localize Brain Metastases. *World Neurosurg*, **106**, 120-130. doi:10.1016/j.wneu.2017.06.128

[85] Leithner, C., & Royl, G. (2014). The oxygen paradox of neurovascular coupling. *J. Cereb. Blood Flow Metab.*, **34**(1), 19-29. doi:10.1038/jcbfm.2013.181

[86] Leithner, C., Royl, G., Offenhauser, N., Fuchtemeier, M., Kohl-Bareis, M., Villringer, A., . . . Lindauer, U. (2010). Pharmacological uncoupling of activation induced increases in CBF and CMRO2. *J Cereb Blood Flow Metab*, **30**(2), 311-322. doi:10.1038/jcbfm.2009.211

[87] Lemieux, P. A., & Durian, D. J. (1999). Investigating non-Gaussian scattering processes by using nth-order intensity correlation functions. *Journal of the Optical Society of America A*, **16**(7), 1651-1664. doi:10.1364/JOSAA.16.001651

[88] Leontiev, O., Dubowitz, D. J., & Buxton, R. B. (2007). CBF/CMRO2 coupling measured with calibrated BOLD fMRI: sources of bias. *Neuroimage*, **36**(4), 1110-1122. doi:10.1016/j.neuroimage.2006.12.034

[89] Li, B., Lin, J., Huang, P., & Chen, X. (2022). Near-infrared probes for luminescence lifetime imaging. *Nanotheranostics*, **6**(1), 91-102. doi:10.7150/ntno.63124

[90] Li, X., Pattanayak, D. N., Durduran, T., Culver, J. P., Chance, B., & Yodh, A. G. (2000). Near-field diffraction tomography with diffuse photon density waves. *Phys Rev E Stat Phys Plasmas Fluids Relat Interdiscip Topics*, **61**(4 Pt B), 4295-4309. doi:10.1103/physreve.61.4295

[91] Lin, S. Z., Sposito, N., Pettersen, S., Rybacki, L., McKenna, E., Pettigrew, K., & Fenstermacher, J. (1990). Cerebral capillary bed structure of normotensive and chronically hypertensive rats. *Microvasc Res*, **40**(3), 341-357. doi:10.1016/0026-2862(90)90032-m

[92] Lo, L.-W., Vinogradov, S. A., Koch, C. J., & Wilson, D. F. (1997). A New, Water Soluble, Phosphor for Oxygen Measurements in Vivo. In D. K. Harrison & D. T. Delpy (Eds.), *Oxygen Transport to Tissue XIX* (pp. 651-656). Boston, MA: Springer US.

[93] Luker, G. D., & Luker, K. E. (2008). Optical imaging: current applications and future directions. *J Nucl Med*, **49**(1), 1-4. doi:10.2967/jnumed.107.045799

[94] Lyons, D. G., Parpaleix, A., Roche, M., & Charpak, S. (2016). Mapping oxygen concentration in the awake mouse brain. *eLife*, 5. doi:e12024 10.7554/eLife.12024

[95] Magistretti, P. J., & Allaman, I. (2015). A cellular perspective on brain energy metabolism and functional imaging. *Neuron*, **86**(4), 883-901. doi:10.1016/j.neuron.2015.03.035

[96] Maini, A. K., & Maini. (2013). *Lasers and Optoelectronics : Fundamentals, Devices and Applications.* New York, UNITED KINGDOM: John Wiley & Sons, Incorporated.

[97] Markel, V. A., & Schotland, J. C. (2001). Inverse problem in optical diffusion tomography. I. Fourier-Laplace inversion formulas. *J Opt Soc Am A Opt Image Sci Vis*, **18**(6), 1336-1347. doi:10.1364/josaa.18.001336

[98] Markel, V. A., & Schotland, J. C. (2002). Inverse problem in optical diffusion tomography. II. Role of boundary conditions. *J Opt Soc Am A Opt Image Sci Vis*, **19**(3), 558-566. doi:10.1364/josaa.19.000558

[99] Masamoto, K., Vazquez, A., Wang, P., & Kim, S. G. (2008). Trial-by-trial relationship between neural activity, oxygen consumption, and blood flow responses. *Neuroimage*, **40**(2), 442-450. doi:10.1016/j.neuroimage.2007.12.011

[100] Materi, J., Mampre, D., Ehresman, J., Rincon-Torroella, J., & Chaichana, K. L. (2020). Predictors of recurrence and high growth rate of residual meningiomas after subtotal resection. *J Neurosurg*, 1-7. doi:10.3171/2019.10.JNS192466

[101] Mik, E. G., Johannes, T., & Ince, C. (2008). Monitoring of renal venous PO2 and kidney oxygen consumption in rats by a near-infrared phosphorescence lifetime technique. *Am J Physiol Renal Physiol*, **294**(3), F676-681. doi:10.1152/ajprenal.00569.2007

[102] Mintun, M. A., Lundstrom, B. N., Snyder, A. Z., Vlassenko, A. G., Shulman, G. L., & Raichle, M. E. (2001). Blood flow and oxygen delivery to human brain during functional activity: Theoretical modeling and experimental data. *Proc. Natl. Acad. Sci. USA*, **98**(12), 6859-6864. doi:10.1073/pnas.111164398

[103] Mintun, M. A., Raichle, M. E., Martin, W. R. W., & Herscovitch, P. (1984). Brain oxygen utilization measured with15O radiotracersand positron emission tomography. *J. Nucl. Med.*, **25**(2), 177-187. Retrieved from ¡Go to ISI¿://WOS:A1984SC28900006 https://jnm.snmjournals.org/content/jnumed/25/2/177.full.pdf

[104] Mondal, S. B., Gao, S., Zhu, N., Habimana-Griffin, L., Akers, W. J., Liang, R., . . . Achilefu, S. (2017). Optical See-Through Cancer Vision Goggles Enable Direct Patient Visualization and Real-Time Fluorescence-Guided Oncologic Surgery. *Ann Surg Oncol*, **24**(7), 1897-1903. doi:10.1245/s10434-017-5804-8

[105] Neira, J. A., Ung, T. H., Sims, J. S., Malone, H. R., Chow, D. S., Samanamud, J. L., . . . Bruce, J. N. (2017). Aggressive resection at the infiltrative margins of glioblastoma facilitated by intraoperative fluorescein guidance. *J Neurosurg*, **127**(1), 111-122. doi:10.3171/2016.7.JNS16232

[106] Newton, A. D., Predina, J. D., Nie, S., Low, P. S., & Singhal, S. (2018). Intraoperative fluorescence imaging in thoracic surgery. *J Surg Oncol*, **118**(2), 344-355. doi:10.1002/jso.25149

[107] Okusanya, O. T., Hess, N. R., Luketich, J. D., & Sarkaria, I. S. (2018). Infrared intraoperative fluorescence imaging using indocyanine green in thoracic surgery. *Eur J Cardiothorac Surg*, **53**(3), 512-518. doi:10.1093/ejcts/ezx352

[108] Onda, N., Kimura, M., Yoshida, T., & Shibutani, M. (2016). Preferential tumor cellular uptake and retention of indocyanine green for in vivo tumor imaging. *Int J Cancer*, **139**(3), 673-682. doi:10.1002/ijc.30102

[109] Parthasarathy, A. B., Tom, W. J., Gopal, A., Zhang, X.,& Dunn, A. K. (2008). Robust flow measurement with multi-exposure speckle imaging. *Optics express*, **16**(3), 1975-1989.

[110] Patel, D. D.,& Lipinski, D. M. (2020). Validating a low-cost laser speckle contrast imaging system as a quantitative tool for assessing retinal vascular function. *Scientific reports*, **10**(1), 1-11.

[111] Pellicer, A., & Bravo Mdel, C. (2011). Near-infrared spectroscopy: a methodology-focused review. *Semin Fetal Neonatal Med*, **16**(1), 42-49. doi:10.1016/j.siny.2010.05.003

[112] Piilgaard, H., & Lauritzen, M. (2009). Persistent increase in oxygen consumption and impaired neurovascular coupling after spreading depression in rat neocortex. *J Cereb Blood Flow Metab*, **29**(9), 1517-1527. doi:10.1038/jcbfm.2009.73

[113] Pogue, B. W., & Rosenthal, E. L. (2021). Review of successful pathways for regulatory approvals in open-field fluorescence-guided surgery. *J Biomed Opt*, **26**(3). doi:10.1117/1.JBO.26.3.030901

[114] Popel, A. S. (1989). Theory of oxygen transport to tissue. *Crit Rev Biomed Eng*, **17**(3), 257-321. Retrieved from https://www.ncbi.nlm.nih.gov/pubmed/2673661 https://www.ncbi.nlm.nih.gov/pmc/articles/PMC5445261/pdf/nihms857462.pdf

[115] Quaresima, V., & Ferrari, M. (2016). Functional Near-Infrared Spectroscopy (fNIRS) for Assessing Cerebral Cortex Function During Human Behavior in Natural/Social Situations: A Concise Review. *Organizational Research Methods*, **22**(1), 46-68. doi:10.1177/1094428116658959

[116] Ramirez-San-Juan, J. C., Mendez-Aguilar, E., Salazar-Hermenegildo, N., Fuentes-Garcia, A., Ramos-Garcia, R.,& Choi, B. (2013). Effects of speckle/pixel size ratio on temporal and spatial speckle-contrast analysis of dynamic scattering systems: Implications for measurements of blood-flow dynamics. *Biomedical optics express*, **4**(10), 1883-1889.

[117] Rodgers, Z. B., Detre, J. A., & Wehrli, F. W. (2016). MRI-based methods for quantification of the cerebral metabolic rate of oxygen. *J. Cereb. Blood Flow Metab.*, **36**(7), 1165-1185. doi:10.1177/0271678x16643090

[118] Sakadzic, S., Roussakis, E., Yaseen, M. A., Mandeville, E. T., Srinivasan, V. J., Arai, K., . . . Boas, D. A. (2010). Two-photon high-resolution measurement of partial pressure of oxygen in cerebral vasculature and tissue. *Nat. Methods*, **7**(9), 755-759. doi:10.1038/nmeth.1490

[119] Sakadzic, S., Yaseen, M. A., Jaswal, R., Roussakis, E., Dale, A. M., Buxton, R. B., . . . Devor, A. (2016). Two-photon microscopy measurement of cerebral metabolic rate of oxygen using periarteriolar oxygen concentration gradients. *Neurophotonics*, **3**(4), 045005. doi:10.1117/1.NPh.3.4.045005

[120] Sakadzic, S., Yuan, S., Dilekoz, E., Ruvinskaya, S., Vinogradov, S. A., Ayata, C., & Boas, D. A. (2009). Simultaneous imaging of cerebral partial pressure of oxygen and blood flow during functional activation and cortical spreading depression. *Appl Opt*, **48**(10), D169-177. doi:10.1364/ao.48.00d169

[121] Santuy, A., Turegano-Lopez, M., Rodriguez, J. R., Alonso-Nanclares, L., DeFelipe, J., & Merchan-Perez, A. (2018). A Quantitative Study on the Distribution of Mitochondria in the Neuropil of the Juvenile Rat Somatosensory Cortex. *Cereb Cortex*, **28**(10), 3673-3684. doi:10.1093/cercor/bhy159

[122] Schlageter, K. E., Molnar, P., Lapin, G. D., & Groothuis, D. R. (1999). Microvessel organization and structure in experimental brain tumors: microvessel populations with distinctive structural and functional properties. *Microvasc Res*, **58**(3), 312-328. doi:10.1006/mvre.1999.2188

[123] Secomb, T. W., Bullock, K. V., Boas, D. A., & Sakadzic, S. (2020). The mass transfer coefficient for oxygen transport from blood to tissue in cerebral cortex. *J. Cereb. Blood Flow Metab.*, **40**(8), 1634-1646. doi:10.1177/0271678X19870068

[124] Sencan, I., Esipova, T. V., Yaseen, M. A., Fu, B., Boas, D. A., Vinogradov, S. A., . . . Sakadzic, S. (2018). Two-photon phosphorescence lifetime microscopy of retinal capillary plexus oxygenation in mice. *J Biomed Opt*, **23**(12), 1-9. doi:10.1117/1.JBO.23.12.126501

[125] Sinha, A. K., Klein, J., Schultze, P., Weiss, J., & Weiss, H. R. (1991). Cerebral regional capillary perfusion and blood flow after carbon monoxide exposure. *J Appl Physiol* (1985), **71**(4), 1196-1200. doi:10.1152/jappl.1991.71.4.1196

[126] Slakter, J. S., Yannuzzi, L. A., Guyer, D. R., Sorenson, J. A., & Orlock, D. A. (1995). Indocyanine-green angiography. *Curr Opin Ophthalmol*, **6**(3), 25-32. doi:10.1097/00055735-199506000-00005

[127] Smith, J. T., Aguenounon, E., Gioux, S., & Intes, X. (2020). Macroscopic fluorescence lifetime topography enhanced via spatial frequency domain imaging. *Opt Lett*, **45**(15), 4232-4235. doi:10.1364/OL.397605

[128] Solomon, M., White, B. R., Nothdruft, R. E., Akers, W., Sudlow, G., Eggebrecht, A. T., . . . Culver, J. P. (2011). Video-rate fluorescence diffuse optical

tomography for in vivo sentinel lymph node imaging. *Biomed Opt Express*, **2**(12), 3267-3277. doi:10.1364/BOE.2.003267

[129] Soustiel, J. F., Glenn, T. C., Shik, V., Boscardin, J., Mahamid, E., & Zaaroor, M. (2005). Monitoring of cerebral blood flow and metabolism in traumatic brain injury. *J. Neurotrauma*, **22**(9), 955-965. doi:10.1089/neu.2005.22.955

[130] Stadlbauer, A., Zimmermann, M., Kitzwogerer, M., Oberndorfer, S., Rossler, K., Dorfler, A., . . . Heinz, G. (2017). MR Imaging-derived oxygen metabolism and neovascularization characterization for grading and IDH gene mutation detection of gliomas. *Radiology*, **283**(3), 799-809. doi:10.1148/radiol.2016161422

[131] Stern, O., & Volmer, M. (1919). Uber die abklingzeit der fluoreszenz, *Phys. Z*, **20**, 183-188.

[132] Suilender, C. T., Mark, A. E., Clark, T. A., Esipova, T. V., Vinogradov, S. A., Jones, T. A., & Dunn, A. K. (2018). Imaging of cortical oxygen tension and blood flow following targeted photothrombotic stroke. *Neurophotonics*, **5**(3). doi:035003 10.1117/1.NPh.5.3.035003

[133] Svenmarker, P., Xu, C. T., Liu, H., Wu, X., & Andersson-Engels, S. (2014). Multispectral guided fluorescence diffuse optical tomography using upconverting nanoparticles. *Applied Physics Letters*, **104**(7), 073703. doi:10.1063/1.4863960

[134] Temma, T., Kuge, Y., Sano, K., Kamihashi, J., Obokata, N., Kawashima, H., . . . Saji, H. (2008). PET O-15 cerebral blood flow and metabolism after acute stroke in spontaneously hypertensive rats. *Brain Res*, **1212**, 18-24. doi:10.1016/j.brainres.2008.03.033

[135] Thews, G. (1960). [A method for determination of oxygen diffusion coefficients, oxygen conductivity and oxygen solubility coefficients in brain tissue]. *Pflugers Arch Gesamte Physiol Menschen Tiere*, **271**, 227-244. Retrieved from https://www.ncbi.nlm.nih.gov/pubmed/13837730

[136] Thomsen, K., Piilgaard, H., Gjedde, A., Bonvento, G., & Lauritzen, M. (2009). Principal cell spiking, postsynaptic excitation, and oxygen consumption in the rat cerebellar cortex. *J Neurophysiol*, **102**(3), 1503-1512. doi:10.1152/jn.00289.2009

[137] Torres, V. C., Li, C., Zhou, W., Brankov, J. G., & Tichauer, K. M. (2021). Characterization of an angular domain fluorescence optical projection tomography system for mesoscopic lymph node imaging. *Appl Opt*, **60**(1), 135-146. doi:10.1364/AO.411577

[138] Tricoli, U., Macdonald, C. M., Da Silva, A., & Markel, V. A. (2018). Optimized diffusion approximation. *J Opt Soc Am A Opt Image Sci Vis*, **35**(2), 356-369. doi:10.1364/JOSAA.35.000356

[139] Tromberg, B. J., Pogue, B. W., Paulsen, K. D., Yodh, A. G., Boas, D. A., & Cerussi, A. E. (2008). Assessing the future of diffuse optical imaging technologies for breast cancer management. *Med Phys*, **35**(6), 2443-2451. doi:10.1118/1.2919078

[140] Tsai, A. G., Friesenecker, B., Mazzoni, M. C., Kerger, H., Buerk, D. G., Johnson, P. C., & Intaglietta, M. (1998). Microvascular and tissue oxygen gradients in the rat mesentery. *Proc Natl Acad Sci USA*, **95**(12), 6590-6595. doi:10.1073/pnas.95.12.6590

[141] Vafaee, M. S., & Gjedde, A. (2000). Model of blood-brain transfer of oxygen explains nonlinear flow-metabolism coupling during stimulation of visual cortex. *J Cereb Blood Flow Metab*, **20**(4), 747-754. doi:10.1097/00004647-200004000-00012

[142] Valabregue, R., Aubert, A., Burger, J., Bittoun, J., & Costalat, R. (2003). Relation between cerebral blood flow and metabolism explained by a model of oxygen exchange. *J. Cereb. Blood Flow Metab.*, **23**(5), 536-545. doi:10.1097/01.WCB.0000055178.31872.38

[143] Valeur, B., & Berberan-Santos, M. N. (2011). A Brief History of Fluorescence and Phosphorescence before the Emergence of Quantum Theory. *Journal of Chemical Education*, **88**(6), 731-738. doi:10.1021/ed100182h

[144] van Beurden, F., van Willigen, D. M., Vojnovic, B., van Oosterom, M. N., Brouwer, O. R., der Poel, H. G. V., . . . Buckle, T. (2020). Multi-Wavelength Fluorescence in Image-Guided Surgery, Clinical Feasibility and Future Perspectives. *Mol Imaging*, **19**, 1536012120962333. doi:10.1177/1536012120962333

[145] Vanderkooi, J. M., Maniara, G., Green, T. J., & Wilson, D. F. (1987). An optical method for measurement of dioxygen concentration based on quenching of phosphorescence. *J. Biol. Chem.*, **262**, 5476-5482.

[146] Vazquez, A. L., Fukuda, M., Tasker, M. L., Masamoto, K., & Kim, S. G. (2010). Changes in cerebral arterial, tissue and venous oxygenation with evoked neural stimulation: implications for hemoglobin-based functional neuroimaging. *J. Cereb. Blood Flow Metab.*, **30**(2), 428-439. doi:10.1038/jcbfm.2009.213

[147] Verweij, B. H., Amelink, G. J., & Muizelaar, J. P. (2007). Current concepts of cerebral oxygen transport and energy metabolism after severe traumatic brain injury. *Prog Brain Res*, **161**, 111-124. doi:10.1016/S0079-6123(06)61008-X

[148] Vovenko, E. (1999). Distribution of oxygen tension on the surface of arterioles, capillaries and venules of brain cortex and in tissue in normoxia: an experimental study on rats. *Pflugers Arch*, **437**(4), 617-623. doi:10.1007/s004240050825

[149] Wang, L., & Wu, H. (2009). *Radiative Transfer Equation and Diffusion Theory. Biomedical Optics*, 83-118. doi:https://doi.org/10.1002/9780470177013.ch5

[150] Watabe, T., Shimosegawa, E., Watabe, H., Kanai, Y., Hanaoka, K., Ueguchi, T., . . . Hatazawa, J. (2013). Quantitative evaluation of cerebral blood flow and oxygen metabolism in normal anesthetized rats: 15O-labeled gas inhalation PET with MRI Fusion. *J Nucl Med*, **54**(2), 283-290. doi:10.2967/jnumed.112.109751

[151] Wei, L., Roberts, D. W., Sanai, N., & Liu, J. T. C. (2019). Visualization technologies for 5-ALA-based fluorescence-guided surgeries. *J Neurooncol*, **141**(3), 495-505. doi:10.1007/s11060-018-03077-9

[152] Weiss, H. R., Buchweitz, E., Murtha, T. J., & Auletta, M. (1982). Quantitative regional determination of morphometric indices of the total and perfused capillary network in the rat brain. *Circ Res*, **51**(4), 494-503. doi:10.1161/01.res.51.4.494

[153] Weyl, H. (1919). Ausbreitung elektromagnetischer Wellen über einem ebenen Leiter. *Annalen der Physik*, **365**(21), 481-500. doi:https://doi.org/10.1002/andp.19193652104

[154] Wilkinson, J. H., Hopewell, J. W., & Reinhold, H. S. (1981). A quantitative study of age-related changes in the vascular architecture of the rat cerebral cortex. *Neuropathol Appl Neurobiol*, **7**(6), 451-462. doi:10.1111/j.1365-2990.1981.tb00245.x

[155] Willford, D. C., Gray, A. T., Hempleman, S. C., Davis, R. W., & Hill, E. P. (1990). Temperature and the oxygen-hemoglobin dissociation curve of the harbor seal, Phoca vitulina. *Respir Physiol*, **79**(2), 137-144. doi:10.1016/0034-5687(90)90013-o

[156] Wilson, D. F. (1992). Oxygen dependent quenching of phosphorescence: a perspective. *Adv Exp Med Biol*, **317**, 195-201. doi:10.1007/978-1-4615-3428-0_20

[157] Wilson, D. F., Erecinska, M., Drown, C., & Silver, I. A. (1979). Oxygen dependence of cellular energy metabolism. *Arch. Biochem. Biophys.*, **195**(2), 485-493. doi:10.1016/0003-9861(79)90375-8

[158] Wilson, D. F., Harrison, D. K., & Vinogradov, S. A. (2012). Oxygen, pH, and mitochondrial oxidative phosphorylation. *J Appl Physiol* (1985), **113**(12), 1838-1845. doi:10.1152/japplphysiol.01160.2012

[159] Wilson, D. F., Lee, W. M., Makonnen, S., Finikova, O., Apreleva, S., & Vinogradov, S. A. (2006). Oxygen pressures in the interstitial space and their relationship to those in the blood plasma in resting skeletal muscle. *J Appl Physiol* (1985), **101**(6), 1648-1656. doi:10.1152/japplphysiol.00394.2006

[160] Wilson, D. F., & Matschinsky, F. M. (2020). Cerebrovascular Blood Flow Design and Regulation; Vulnerability in Aging Brain. *Front Physiol*, **11**, 584891. doi:10.3389/fphys.2020.584891

[161] Wirth, D. J., Sibai, M., Wilson, B. C., Roberts, D. W., & Paulsen, K. (2020). First experience with spatial frequency domain imaging and red-light excitation of protoporphyrin IX fluorescence during tumor resection. *Biomed Opt Express*, **11**(8), 4306-4315. doi:10.1364/BOE.397507

[162] Yaseen, M. A., Srinivasan, V. J., Sakadzic, S., Radhakrishnan, H., Gorczynska, I., Wu, W., . . . Boas, D. A. (2011). Microvascular oxygen tension and flow measurements in rodent cerebral cortex during baseline conditions and functional activation. *J Cereb Blood Flow Metab*, **31**(4), 1051-1063. doi:10.1038/jcbfm.2010.227

[163] Yucel, M. A., Selb, J. J., Huppert, T. J., Franceschini, M. A., & Boas, D. A. (2017). Functional near infrared spectroscopy: enabling routine functional brain imaging. *Curr. Opin. Biomed. Eng.*, **4**, 78-86. doi:10.1016/j.cobme.2017.09.011

[164] Zhang, Y., Yin, Y., Li, H., & Gao, J. H. (2020). Measurement of $CMRO_2$ and its relationship with CBF in hypoxia with an extended calibrated BOLD method. *J Cereb Blood Flow Metab*, **40**(10), 2066-2080. doi:10.1177/0271678X19885124